# Control of Nanoscale Thermal Transport for Thermoelectric Energy Conversion and Thermal Rectification

Souvik Pal

Dissertation submitted to the faculty of the Virginia Polytechnic Institute and State University

in partial fulfillment of the requirements for the degree of

Doctor of Philosophy

in

Engineering Mechanics

Ishwar K. Puri, Chair

Muhammad R. Hajj, Co-chair

Marwan Al-Haik

Raffaella De Vita

Mark Stremler

Mayuresh Patil

December 2, 2013

Blacksburg, Virginia

Keywords: Nanoscale heat transfer, molecular dynamics, thermoelectric energy, thermal rectification, phononics

# Control of Nanoscale Thermal Transport for Thermoelectric Energy Conversion and Thermal Rectification

Souvik Pal

ABSTRACT

Materials at the nanoscale show properties uniquely different from the bulk scale which when controlled can be utilized for variety of thermal management applications. Different applications require reduction, increase or directional control of thermal conductivity. This thesis focuses on investigating thermal transport in two such application areas, viz., 1) thermoelectric energy conversion and 2) thermal rectification. Using molecular dynamics simulations, several methods for reducing of thermal conductivity in polyaniline and polyacetylene are investigated. The reduction in thermal conductivity leads to improvement in thermoelectric figure of merit. Thermal diodes allow heat transfer in one direction and prevents in the opposite direction. These materials have potential application in phononics, i.e., for performing logic calculations with phonons. Rectification obtained with existing material systems is either too small or too difficult to implement. In this thesis, a more useful scheme is presented that provides higher rectification using a single wall carbon nanotube (SWCNT) that is covalently functionalized near one end with polyacetylene (PA). Although several thermal diodes are discussed in literature, more complex phononic devices like thermal logic gates and thermal transistors have been sparingly investigated. This thesis presents a first design of a thermal AND gate using asymmetric graphene nanoribbon (GNR) and characterizes its performance.

*Dedicated to my parents and my wife Priyanka*

# Acknowledgements

This PhD would never have been possible without my advisor Prof. Ishwar K. Puri. He was a constant source of inspiration through his unparalleled scientific vision. He always encouraged independent thinking and innovative approaches in solving scientific problems. One of the biggest skills I learnt from him is the art of communicating science to the society. The current academic literature is infested with esoteric jargon. As a result, the common man fails to perceive the impact of a scientific work on the society. Through his critical review and feedback, my scientific communication skills improved immensely. He was also an excellent research mentor. During many tough times in the past three years, whenever I lost the forest for the trees, he restored it. The vibrant and cheerful nature of his personality deeply influences my thinking and philosophy of life. I deeply respect him for the way he regards the value of family. Whenever I wanted to visit my parents in India, he smilingly agreed. I thank Professor from the core of my heart for all the help and support.

I sincerely thank my collaborator and ex-labmate Ganesh who introduced me to the field of nanoscale thermal transport. I learnt the fundamentals of molecular dynamics from him. His ideas and suggestions helped me gain initial momentum when I began as a PhD student and was

struggling to find a research direction. He also mentored me in preparing scientific manuscripts. His observant scrutiny of the manuscripts made them achieve highest academic quality.

The Multiphysics Research Group (MuRG) holds a very special place in my heart. This is not just a room in a building where I used to go to work, or not just a group of people I used to work with, or not a collection of facilities or instruments. MuRG is more than that. It has given me an identity, a scientific orientation, a philosophy towards performing fundamental research of highest standard. I deeply thank everyone in MuRG from current and previous years for making this so special. I would like to express my thanks to Dr. Ranjan Ganguly and Dr. Swarnendu Sen, both Murg alumni, for introducing me to Professor. After I started working, Dr. Ganguly provided lots of inputs in brainstorming sessions when I was trying to identify my dissertation problem. Special thanks to my labmates Monrudee, Suvojit, Ravi, Aschvin and Austin for making my stay in MuRG such an enjoyable experience. They are all really friendly and helpful. On numerous occasions they provided extremely valuable comments on my research through informal friendly discussions, which also served as a stress release mechanism for me.

I thank my committee members Dr. Hajj, Dr. Stremler, Dr. Al-Haik, Dr. De Vita and Dr. Patil for serving on my committee and for their valuable comments and feedbacks about my research. I also thank all the ESM staff, especially Anne-Marie, Linda and Lisa for always providing help and support in whatever way they could. I am fortunate to have a group of friends, especially everyone in the “Friday Nighters Association” who made my stay in Blacksburg some of the most memorable and enjoyable times of my life.

My parents have been extremely supporting. Their love, affection and constant words of encouragement kept me going. There were times when I felt extremely frustrated and depressed

in this journey. They provided motivation in those tough times. Even though they are miles away, they are and always will be in my heart. Whatever I am today, it is because of them.

Finally, I thank Priyanka, my wife and soul mate, for her endless love and support. She stood by my side in all situations of my life, good or bad. Her amazingly simple solutions to all my complex problems made life a lot easier.

Souvik Pal

Blacksburg

12/2/2013

# Attribution

Professor Ishwar K. Puri is my thesis advisor. He mentored me throughout my PhD. He provided new ideas, research directions and key technical inputs at all the stages. He also provided critical feedback while preparing manuscripts. He is a co-author in all my scientific publications during this PhD.

Dr. Ganesh Balasubramanian introduced me to molecular dynamics simulations and the field of nanoscale thermal transport. He helped me with research ideas in the beginning phases of my PhD. He also provided critical reviews in manuscript preparation. He is a co-author in two of my published journal papers.

# Contents

# List of Figures

# List of Tables

Chapter 1

# Introduction

### 1.1. Fourier's law of heat conduction

Heat transfer in solids is a widely researched topic dating back to 18th century. In 1807, Jean Baptiste Joseph Fourier first formulated the transient heat conduction problem using partial differential equations in his masterpiece, 'Théorie de la propagation de la chaleur dans les solides' [1]. In English that translates to "Theory of heat propagation in solids". Fourier's law of heat conduction is written as

$$J = -\kappa \nabla T . \tag{1.1}$$

Here, $J$ denotes the heat flux, $\kappa$ the thermal conductivity and $\nabla T$ the temperature gradient. This was an immense contribution. Fourier's formulation provides a very general framework that describes any transient process involving molecular diffusion. It has been used to derive several subsequent models, e.g., diffusion of a chemical species and flow of fluids through porous media. Narasimhan provides an excellent review of the historical aspect, depth and interdisciplinary nature of Fourier's heat conduction equation [2]. Even after two centuries, Fourier's law provides the foundation for modeling heat transfer in solids. However, it does not answer a very fundamental question: What is it that actually carries the heat? Is it the same for all solids?

### 1.2. Heat carriers for different material types

The physics of heat transfer has undergone considerable evolution through the last two centuries. In the early 19th century, it was believed that an entity called '*calorie*' carries heat from a hotter body to a colder one [3]. Classical thermodynamics was developed mainly based on this understanding. Since the involved theories are entirely phenomenological, it was possible to ignore the physics of heat carriers. In 1914, Debye proposed that heat transmission occurs through propagation of vibrational energy. This was the first correlation of heat transfer with the kinematics of fundamental particles. Over the last century, rigorous experimentation has demonstrated that heat is transmitted by the stochastic motion of fundamental particles such as electrons, atoms and molecules.

For metals, electrons are the major heat carriers. This simplifies studying heat transfer and enables formulation of the Weidman-Franz-Lorenz Law relating electrical and thermal conductivities [4]. For non-metals, however, identifying the heat carrier is non-trivial due to the possibility of multiple mechanisms of heat transfer. Other than electrons, atomic vibrations or 'phonons' form a major heat transfer mechanism. In a solid, atoms are tightly packed. The increase in temperature in a region enhances atomic vibrations therein. This induces vibrations in neighboring atoms. The vibrational energy propagates in this manner from a high temperature region to a low temperature region. In several materials, e.g., polymers and lightly doped semiconductors, electronic contribution to heat transfer is negligible and understanding phononic transport becomes crucial.

### 1.3. Phonon transport

Phonons have both a wave and a particle nature. When viewed as a wave, each phonon is a wave of vibrational energy that transports through the solid. Each phonon wave has a definite frequency and a wavelength. Superposition or interaction of multiple phonons creates a wave packet that moves as a result of phonon transport. These wave packets are equivalently represented as particles and provide a particle nature to phonon. Therefore, the dynamics of a collection of phonon waves can be equivalently described by a collection of particles in a box which collides with each other.

The interaction of atoms in a solid can be described by a potential $\phi$, such that the forces on atoms are given as

$$F = -\nabla\phi. \tag{1.2}$$

The process of a phonon wave getting deflected from its path due to interaction with another phonon, material impurities or boundaries is called scattering. In a simplified model with no impurity, each atom is assumed to be connected to their neighbors by linear springs. In such a case, interaction potential $\phi$ is harmonic and different phonons do not interact among themselves [3]. Consequently, there is no scattering mechanism present and phonons travel uninterrupted from the high temperature region to the low temperature region. Since there is no resistance to the flow of heat carriers, the thermal conductivity in this case becomes infinite. The anharmonicity in the interaction potential causes the phonons to interact and thus scatter. Therefore, even in a pure material, anharmonic atomic interaction leads to finite thermal conductivity. The presence of impurity and boundaries causes additional scattering and further lowers the thermal conductivity.

### *1.3.1. Phonon transport at the nanoscale*

In a bulk material (macro scale) at room temperature, phonon-phonon scattering dominates compared to all other scattering mechanisms. As the material size shrinks, below a threshold size, the phonon mean free path becomes comparable to material dimension [3, 5]. Consequently, boundary phonon scattering begins to dominate. Also, since the surface area to volume ratio is inversely proportional to material dimension, phonon transport across material interfaces begins strongly influencing the transport within the material [6, 7]. Since the physics of phonon scattering and transport mechanisms for nanoscale materials is characteristically different from bulk scale. This is manifested in thermal properties that are remarkably different from bulk scale [8-10]. For instance, transverse thermal conductivity of silicon thin films (thickness ~10-100 nm) is significantly less than that of bulk silicon [11-13]. The reduction is caused by increase in phonon transmission resistance due to strong phonon boundary scattering. In bulk materials, thermal conductivity is independent of the material size. In contrast, at the nanoscale, it becomes size dependent. '*Anomalous heat transfer*' refers to a class of problems in low dimensional nanoscale systems, where the longitudinal thermal conductivity $\kappa$ of one-dimensional and quasi one-dimensional atomic chains, e.g. silicon nanowires, polyethylene chains, diverges with the length and number of atoms in the chain, i.e. $\kappa \sim L^{\beta}$ [14-19]. Here, $\beta$ is a positive exponent and $L$ is the chain length. Carbon nanotubes (CNT) are quasi one-dimensional nanostructures known for remarkable high thermal conductivity values [20-23]. Such novel thermal properties can be utilized for a wide range of thermal management problems listed in Table 1.1, such as increasing the figure of merit in thermoelectric energy conversion by reducing the thermal conductivity of polyacetylene. The applications can be classified into three major categories, 1) applications with high thermal conductivity requirement 2) applications with

low thermal conductivity requirement 3) applications with the requirement of directional control of thermal conductivity, i.e. thermal rectification, as explained in section 1.4.

**Table 1.1: Categories of thermal management applications**

| Category | Application | Materials or Nanostructures involved |
|---|---|---|
| **High thermal conductivity requirement** ➡ | Enhancing heat transfer in nanoscale MOSFET, CPU and other nano-electronic circuits. | Graphene [24-26]<br>CNT [27-30] |
| | Enhancing heat transfer from a solid surface to the adjacent liquid during pool boiling. | CNT[31, 32] |
| **Low thermal conductivity requirement** ⇨ | Increasing the figure of merit for thermoelectric energy conversion | Superlattice [33, 34]<br>Silicon Nanowire [8],<br>Electrically conducting polymers (polyaniline, Polyacetylene)[35, 36] |
| **Requirement of directional control of thermal conductivity** ➡⇦ | Performing logic calculations with phonons. It requires thermal rectification of heat flux, i.e. to allow heat transfer only in one direction and prevent in the opposite direction. | Mass graded CNT [37] ,<br>Polymer –silicon Superlattice [38] |

## 1.4. Calculation of phonon thermal conductivity

Calculation of $\kappa_p$ is usually performed using the Boltzmann Transport Equation (BTE) [39, 40] or molecular dynamics (MD) simulations [7, 35]. In the BTE approach, the physics of phonon scattering and transport is explicitly modeled. This requires prior understanding and often some idealizations of the underlying thermal transport processes. In contrast, MD simulations assume nothing about the transport processes in a material. The only input it requires is a valid interatomic potential and boundary conditions. Therefore it is more fundamental and can describe complicated phonon transport mechanisms.

### *1.4.1. MD simulation*

MD [41, 42] is a computer based deterministic simulation technique which considers each atom in a material system as a sphere and solves Newton's laws of motion for each of them under the influence of a mutual interaction potential with other atoms. The interatomic potential is the input to MD and usually obtained from either quantum mechanical calculations or from experiments. The position and velocity of each atom is tracked at every instant of time. The system proceeds forward in time by integrating the equation of motion under the constraints of an imposed statistical ensemble (canonical, grand canonical, etc.). Because of its fundamental nature, MD is routinely used to study and evaluate properties of systems at small length and time scales [42, 43]. The two most commonly used MD methods for a $\kappa_p$ calculation in a dielectric solid are the equilibrium MD (EMD) also known as the Green-Kubo method [44, 45] and non-equilibrium MD (NEMD) [45, 46].

### *1.4.2. The Green-Kubo method*

The Green-Kubo method calculates the thermal conductivity at the equilibrium state of the system. Even when the system is in thermal equilibrium, there are heat fluxes in the material due to statistical fluctuations in temperature. By using the fluctuation-dissipation theorem, the heat flux autocorrelation function can be related to the thermal conductivity tensor as

$$\kappa_p = \frac{1}{k_B V T^2} \int_0^{\tau} \langle J(t) J(0) \rangle dt \tag{1.3}$$

Here, $k_B$ denotes Boltzmann constant, $V$ the system volume, $T$ the temperature and $J$ the heat flux. The time constant $\tau$ is the minimum time required for the heat flux autocorrelation function to decay to zero. Since the full thermal conductivity tensor can be obtained, this method is more appropriate for anisotropic systems. The main disadvantages of this method is that it takes a long

time for the heat flux autocorrelation function to decay to zero and the predictions depend on the size of the system [45].

### *1.4.3. The NEMD method*

The NEMD is a more direct method in the sense that it mimics typical experiments to evaluate the thermal conductivity. The typical simulation system for NEMD is shown in Fig. 1.1. Two thin regions equidistant from left and right boundary are setup as source and sink. Periodic boundary condition is imposed on the left and right boundaries. This eliminates the size dependence of thermal conductivity. To set up heat transfer, at each timestep $\Delta t$, the velocities

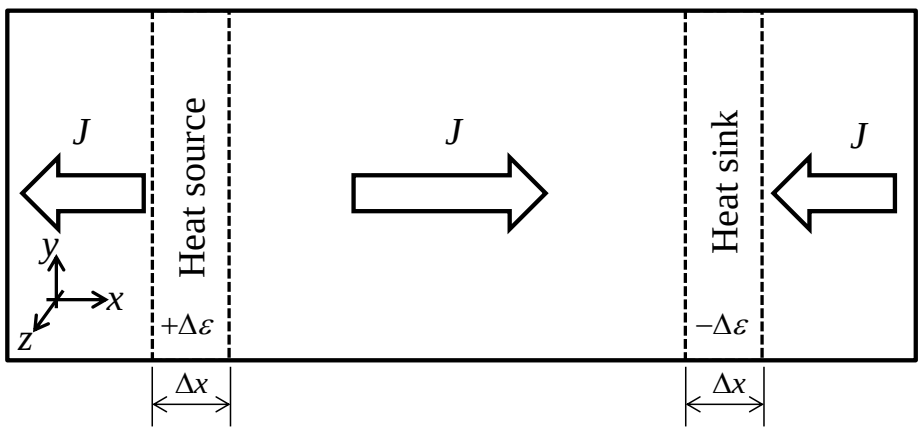


**Figure 1.1:** The simulation cell for calculating thermal conductivity along *x* direction using NEMD method. The periodic boundary condition is applied to the right and the left boundary. The heat sink and the source are equidistant from the right and left boundary respectively.

of the atoms in the source are scaled up, so that a net positive kinetic energy $\Delta\varepsilon$ is added to the system and those in the sink are scaled down so that $\Delta\varepsilon$ amount of energy is removed from the system thus keeping the total energy constant. This eventually sets up a heat flux $J$ in the system. When the steady state conditions are achieved, the heat flux can be calculated as $J = \Delta\varepsilon / (2A\Delta t)$, where $A$ is the cross sectional area in the *y*-*z* plane. The temperature gradient $\frac{\partial T}{\partial x}$ in the system

is directly calculated from the linear portion of the steady state temperature profile. The thermal conductivity is then calculated using Fourier's law in Eq. (1.1). However, for Fourier's law to be applicable, two conditions must be satisfied. First, the duration of a simulation must be at least three orders of magnitude greater than phonon relaxation time. The typical relaxation time for phonon transport is $10^{-12}$ s. Hence, a simulation time of $\sim 10^{-9}$ s, i.e. nanoseconds, are necessary and are commonly found in the current literature. Secondly, the heat flux $J$ should be less than a certain threshold for the linearity of Eq. (1.1) to hold true. $J$ depends on the ratio $\Delta\varepsilon / A$. The maximum allowed value of $\Delta\varepsilon / A$ for applicability of Fourier's law is reported to be $1\times10^{-4}$ eV/nm$^2$ [45]. Although this value is not universal, higher values of $\Delta\varepsilon / A$ will produce non-linear system response and temperature profile and therefore not recommended.

### *1.4.4. The RNEMD method*

The reverse NEMD or RNEMD [46] is a slight variant of NEMD. In this method, instead of rescaling the velocities, heat transfer is setup by exchanging velocities in the source and sink. The simulation cell is shown in Fig. 1.2.

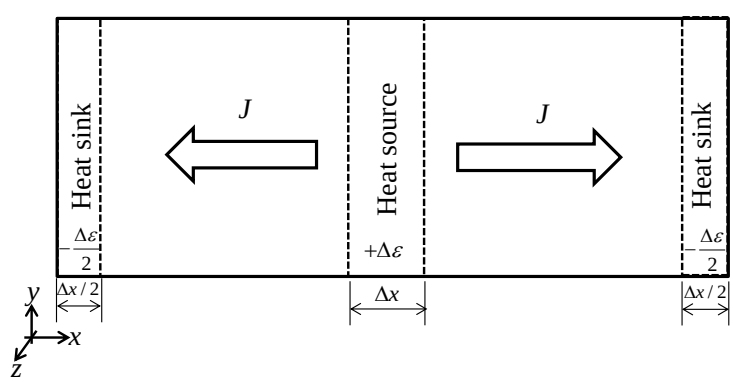


**Figure 1.2:** The simulation cell for RNEMD or Müller-Plathe technique. The heat source is placed in the middle and the two heat sinks are placed at the either ends subjected to

periodic boundary condition. The width of each of the sinks is half the width of the source. The temperature profile resulting from this system is symmetric about the source in the middle.

The atom with the highest temperature in one of the sink and the atom with lowest temperature in the source are paired and their velocities are swapped which essentially swaps their kinetic energies. When continued, this process sets up a heat transfer in the system and at steady state a temperature profile is obtained from which $\frac{\partial T}{\partial x}$ is evaluated. By keeping track of the energy transfer due to the swapping at each step, the total energy transfer in a given time and $J$ can be calculated. Finally, using Fourier's law, $\kappa_p$ can be calculated. Since this method conserves both momentum and energy, we adopt this method. Further details about RNEMD and MD in general can be found in the following chapters.

### 1.5. A brief outline

The present thesis contains the studies of phonon transport phenomena in dielectric materials having important applications in thermoelectric energy conversion and thermal rectification. Thermoelectric materials produce a voltage when subjected to a temperature difference. For sustainability of the voltage production, the temperature difference between the hot and the cold ends need to be kept constant. This requires a material with very low thermal conductivity. Certain classes of polymers like polyaniline (PANI) and polyacetylene (PA) can conduct electricity [47]. The index of performance of these polymers in thermoelectric energy conversion is the thermoelectric figure of merit $ZT = S^2\sigma T/\kappa$, where $S$ is the Seebeck coefficient, $T$ is the absolute temperature, $\sigma$ is the electrical conductivity and $\kappa$ is the thermal conductivity. Since $ZT$ is inversely proportional to $\kappa$, lower is the thermal conductivity, higher

is the $ZT$. Hence, different strategies for reducing $\kappa$ are explored in chapters 2 and 3. In chapter 2, the dependence of mechanical strain on thermal conductivity in pure PANI, pure PA and mixtures of PANI and PA is studied using RNEMD [35]. It is found that by compressing the material, the polymer chains can be more misaligned with respect to the heat transfer direction. This increases phonon scattering thereby reducing the thermal conductivity. The chapter also addresses the relatively unexplored problem of dependence $\kappa_p$ of amorphous polymeric mixtures on the mixing ratio. The contents of this chapter has been published in Journal of chemical Physics article "Modifying thermal transport in electrically conducting polymers: Effects of stretching and combining polymer chains" [35] and has been included here with permissions from American Institute of Physics.

In chapter 3, the effect of transverse boundary phonon scattering on longitudinal phonon transport in strategically designed ordered PANI-PA nanocomposites is investigated using RNEMD [48]. It is found that in polymers like PANI and PA where the bonded interactions are highly anharmonic, vibrations and phonon transport in longitudinal direction is coupled with that in transverse direction. If the transverse interfacial area between PANI and PA is increased, the longitudinal thermal conductivity reduces. The contents of this chapter has been published in Applied Physics Letters article "Reducing thermal transport in electrically conducting polymers: Effects of ordered mixing of polymer chains" [48] and has been included here with permissions from American Institute of Physics.

Thermal rectification and phononics has gained recent attention because of its potential future applications in developing thermal logic gates and thermal computer. Phononics refers to the idea that phonons, like electrons, can be used to perform logic calculations. Certain materials and nanostructures have been recently reported to behave as good conductor in one direction and

a good thermal insulator in the opposite direction [37, 38]. They are called thermal diodes drawing inspiration from electronics, where diodes allow electric current to flow through them in only one direction. Using these thermal diodes, more complicated structures like logic gates has also been proposed [49]. However, most of these claims are far from comprehensive and performance of existing nanostructures and materials are far from satisfactory for any real world application. Hence tremendous research is being carried out in this area. Chapter 4 demonstrates a particular nanocomposite using CNT and PANI to create a thermal diode. The diode demonstrates highest thermal rectification effect compared to that found in existing studies with CNT based thermal diodes. The thermal rectification effect is characterized by computing heat currents in the forward and reverse biased configuration of the diode. The underlying principles are identified by analyzing the phonon spectrum mismatch among different sections in the diode and optimum operating temperature ranges are determined.

Graphene nanoribbons (GNR) show very high thermal rectification effect [50]. The design and characterization of the first thermal AND gate using two identical GNR thermal diodes is presented in Chapter 5. The device has two inputs and a biasing terminal. The behavior of the device is characterized and compared to that of an electrical AND gate using truth tables. The dependence of gate mechanism on thermal rectification in the two diodes is investigated through phonon spectrum overlap/mismatch analysis. The AND gate is found to be more effective at nanoscale and at temperatures much below room temperature. The switching time of the AND gate is also determined.

In chapter 6, some of the future research directions are outlined.

Chapter 2

# Modifying thermal transport in electrically conducting polymers: effects of stretching and combining polymer chains

*If their thermal conductivity can be lowered, polyacetylene (PA) and polyaniline (PANI) offer examples of electrically conducting (EC) polymers that can have potential use as thermoelectrics. Thermal transport in such polymers is primarily influenced by bonded interactions and chain orientations relative to the direction of heat transfer. We employ molecular dynamics simulations to investigate two mechanisms to control the phonon thermal transport in PANI and PA, namely, (1) mechanical strain, and (2) polymer combinations. The molecular configurations of PA and PANI have a significant influence on their thermal transport characteristics. The axial thermal conductivity increases when a polymer is axially stretched but decreases under transverse tension. Since the strain dependence of the thermal conductivity is related to the phonon scattering among neighboring polymer chains, this behavior is examined through Herman's orientation factor that quantifies the degree of chain alignment in a given direction. The conductivity is enhanced as adjacent chains become more aligned along the*

*direction of heat conduction but diminishes when they are orthogonally oriented to it. Physically combining these polymers reduces the thermal conductivity, which reaches a minimum value for a 2:3 PANI/PA chain ratio.*

## 2.1. Motivation and background

Delocalized electrons associated with the $sp^2$ hybridized carbon atoms contained within the backbone of conjugated EC polymers like PA and PANI have a high mobility. These electrons serve as the primary charge carriers for electrical conduction [51], which makes them suitable for thermoelectric applications [52, 53]. The electron delocalization and hence the electrical conductivity $\sigma$ can be further enhanced by doping them with various materials. Since the charge transport of delocalized electrons in an EC polymer has a different mechanism than the free electron drift in metals, their electrical conductivity is only weakly correlated with their thermal conductivity $\kappa$. Hence, while the doping of EC polymers increases $\sigma$, it does not significantly influence $\kappa$ [52, 54].

Since the electron contribution to heat conduction is typically insignificant in EC polymers, we only consider the more relevant contribution of phonon transport. Individual polymer chains can have a relatively high phonon thermal conductivity $\kappa_p$ as compared to their bulk amorphous volumes [55]. In contrast with individual chains, the highly twisted and irregular bulk macromolecular chain arrangements serve to enhance phonon scattering and shorten the phonon mean free paths, thus reducing $\kappa_p$ [56]. While the literature discusses means to increase $\kappa_p$ for polymers [55, 56], few strategies have been offered for ways to lower it [57]. Lowering $\kappa_p$ is essential if EC polymers are to find widespread use in thermoelectrics [58], thermal barrier coatings [59], and phase change memory technology [60].

Unlike crystals, polymer chains experience both bonded and nonlinear anharmonic nonbonded interactions [57]. Hence, the mechanism that reduces the lattice thermal conductivity of strained crystals [61-63] fails to explain the corresponding influence of stretching on thermal transport in polymers. We employ atomistic simulations to understand how phonon thermal transport in the EC polymers (PANI and PA) can be modified when (1) they are subject to axial and transverse strains, or (2) their polymer chains are physically mixed.

## 2.2. Computational Methodology

### *2.2.1. Nonequilibrium molecular dynamics simulations (NEMD)*

Molecular dynamics (MD) simulations have been used to investigate the chain configuration of bulk polymers under applied strain[64-67]. We employ nonequilibrium molecular dynamics (NEMD) to determine the thermal conductivity of strained PANI and PA using the LAMMPS code [68]. Three systems are considered, namely, (1) pure amorphous PANI in Emeraldine Base (EB) form [69], (2) pure amorphous PA in trans-isomeric form, and (3) combinations of PANI and PA containing different numbers of chains of each polymer.

**Table 2.1:** The dimensions of the simulated systems and the number of atoms present in them are listed. The percentage of PANI corresponds to the number of PANI chains relative to the total number of polymer chains in the simulation domain. The system dimensions reported are values obtained upon equilibration of the polymers.

| Material | System Dimensions | | | No. of atoms |
|---|---|---|---|---|
| % of PANI | x(Å) | y(Å) | z(Å) | |
| 100 (Pure PANI) | 35.42 | 35.42 | 35.42 | 3840 |
| 87.5 | 35.63 | 35.63 | 35.63 | 3860 |
| 75 | 35.67 | 35.67 | 35.67 | 3880 |
| 62.5 | 35.95 | 35.95 | 35.95 | 3900 |

| | | | | |
|---|---|---|---|---|
| 50 (1:1 Mixture) | 35.90 | 35.90 | 35.90 | 3920 |
| 37.5 | 36.19 | 36.19 | 36.19 | 3940 |
| 25 | 36.12 | 36.12 | 36.12 | 3960 |
| 12.5 | 36.37 | 36.37 | 36.37 | 3980 |
| 0 (Pure PA) | 36.11 | 36.11 | 36.11 | 4000 |

The number of atoms and the dimensions of the equilibrated systems used to simulate unstrained PANI and PA, and the different PANI/PA mixture compositions that are considered are provided in Table 2.1. Periodic boundary conditions are imposed along all three coordinate directions. Both the amorphous PANI and PA systems contain 80 chains while their 1:1 mixture contains 40 chains of each polymer. Each PANI and PA chain contains 24 carbon atoms. The chain structures are generated with Xenoview [70] for an initial density $\rho$ at $T$ = 300 K and $P$ = 1 atm. (where $\rho_{PANI}$ = 1.3 g cm$^{-3}$ and $\rho_{PA}$ = 1.16 g cm$^{-3}$) [69, 71]. The parameters for the PCFF (Polymer Consistent Force Field) that describe the bonded and nonbonded interactions are obtained from the literature [69, 70], details about which are provided in the Appendix A. The VMD package [72] is used to visualize the response of the polymers to applied strains.

The energy of each system is first minimized using the conjugate gradient technique [68]. The minimized structure is then initialized at 300K. This is followed by a two-step process where the system is: (1) first heated over 0.1 nanoseconds (ns) to a temperature much higher than the glass transition temperature ($T_g$), i.e. from $T$ = 300 K to $T$ = 1000 K (for PANI, $T_g$ = 493 K, for PA, $T_g$ = 473 K), and (2) then cooled back to 300 K over 0.1 ns under a canonical (NVT) ensemble using a Langevin thermostat with a coupling time of 0.1 picoseconds (ps). This annealing and tempering relaxes the molecules and removes any bond symmetry that could have been an artifact produced through polymer construction.

Next, the system is equilibrated under isothermal-isobaric conditions (NPT with $T$ = 300 K and $P$ = 1 atm.) followed by NVT and NVE ensembles, each for 0.2 ns respectively. The equilibrated systems are strained from an initial zero engineering strain rate $e$ in five increments of $2\times10^{10}$ $s^{-1}$ to $10\times10^{10}$ $s^{-1}$. These strains are applied along both the axial ($x$) and transverse ($y$) directions through separate simulations. All strained structures are allowed to equilibrate for 0.3 ns under the NVT ensemble before thermal conductivity calculations are performed.

### *2.2.2. Phonon thermal conductivity*

The axial thermal conductivity, $\kappa_p$ is determined by employing a standard NEMD technique [73]. A source (of dimensions 0.7084 ($x$) × 35.42 ($y$) × 35.42 ($z$) Å) placed at the center of the system heats two sinks that are located at both $x$-wise boundaries (with dimensions equal to half the $x$-wise thickness of the heat source), as shown in Fig. 2.1.

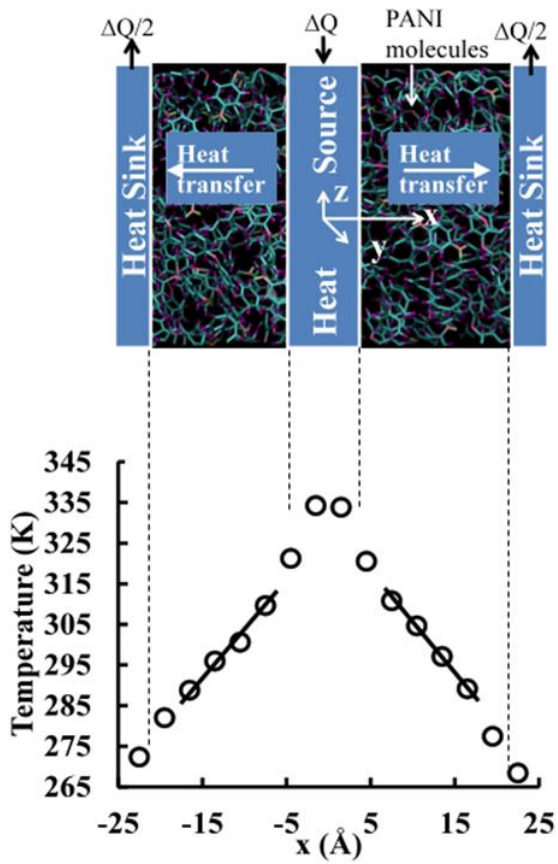


**Figure 2.1:** The top panel shows the *x*-*z* cross sectional view of pure amorphous PANI. The heat flux *Q* from the source is transferred axially through the material to the sinks at its two *x*-wise boundaries. The bottom panel shows the simulated temperature profile for a representative case, linear portions of which are used to calculate the temperature gradient. The position of the temperature peak in the system corresponds to the heat source in the top panel, and the lower temperatures at both boundaries correspond to the two heat sinks.

The figure also shows how the temperature gradient across the material is calculated over linear sections of the steady state temperature distribution. This temperature gradient is sampled over the final 1 ns of the 5 ns NEMD simulation. A temporal average is employed to determine its steady state value and the net heat flux transferred between the heat source and its sinks.

Thereafter, the thermal conductivity is calculated based on Fourier's heat conduction law [74]. More extensive details about the simulation methodology are available in the Appendix B.

## 2.3. Results and discussion

### *2.3.1. The effect of strain on thermal conductivity*

Figure 2.2(a) presents $\kappa_p$ at different uniaxial strains for PANI, PA and a 1:1 PANI/PA mixture. Its value increases with increasing strain but the rate of increase in $\kappa_p$ successively decreases. The thermal conductivities of unstrained PANI and PA that are thus obtained (0.1 and 0.08 $Wm^{-1}K^{-1}$ respectively) are compared with reported experimental measurements (0.11 and 0.38 $Wm^{-1}K^{-1}$ [75, 76]). While the two PANI values are in good agreement, the ones for PA, for which the cited measurement is for a 0.89 μm thin film [76], are not, where the simulated value is much lower.

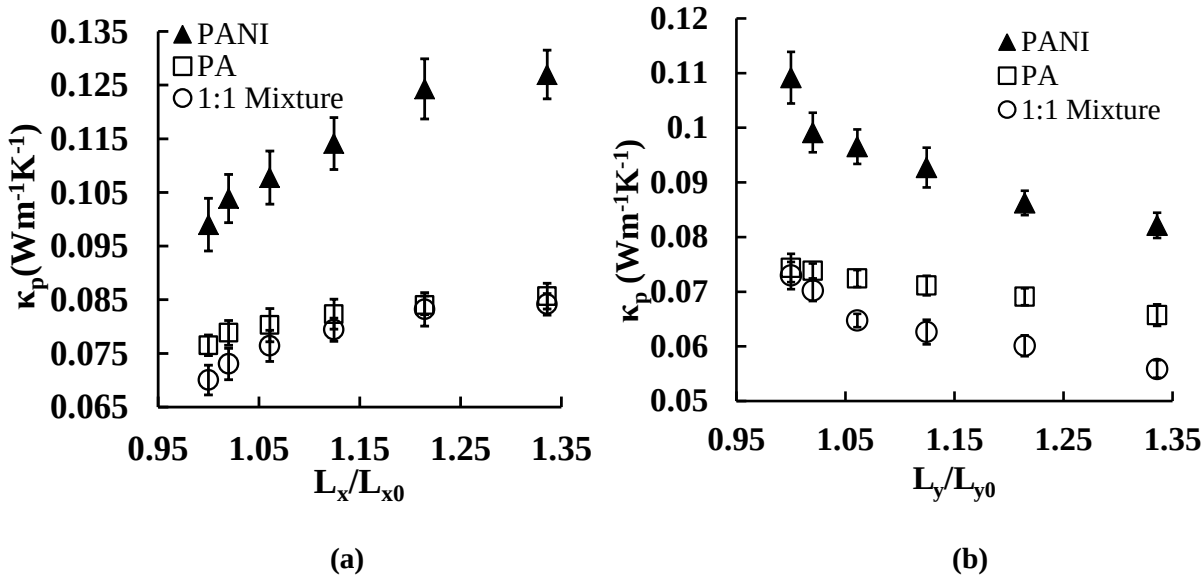


**Figure 2.2:** (a) Variation of the phonon thermal conductivity $\kappa_p$ along the axial ($x$-wise) direction with respect to the axial tensile strain for three different systems (PANI, PA, and a 1:1 mixture). $L_x$ denotes the axial dimension of the simulation domain and $L_{x0}$ the corresponding unstretched length. (b) Variation of $\kappa_p$ with respect to transverse ($y$-axis) tensile strain for the three systems. $L_y$ denotes the transverse dimension of the domain and $L_{y0}$ the corresponding unstretched length. For both (a) and (b), error bars represent the standard error in $\kappa_p$ calculated from ten spatially averaged temperature profiles at intervals of 0.1 ns over the last 1 ns of the simulation.

The thermal conductivity is often lower at the nanoscale, as for our simulations, than at the microscale, as for thin films, since the energy losses due to phonon scattering at the system boundaries are enhanced as the system dimensions are reduced [77, 78]. We also show later that the helical structure of PA lends itself to a lower $\kappa_p$ in contrast to the more planar PANI.

Large tensile strains in crystal lattices reduce *van der Waals* interactions and hence the phonon thermal conductivity [62]. However, phonon transport in polymers occurs through both (1) intrachain energy exchanges that involve relatively stiff covalent bonds in the polymer

backbone, and (2) interchain heat transfer through weak *van der Waals* interactions that involve softer force constants between the constituent atoms of two different chains [79]. Hence, unlike for crystal lattices, the major phonon contribution to heat transfer in polymers is through the bonded interactions. The increase in $\kappa_p$ shown in Fig. 2.2(a) occurs due to the growing structural ordering that is induced in the polymers as these are strained. The polymer chains that are highly twisted and randomly oriented in the initial unstretched amorphous bulk provide a structure that favors phonon-phonon scattering, thus lowering the thermal conductivity. In contrast, straining the material incrementally aligns the chains along the direction of stretch. Chain alignment lowers phonon scattering and improves energy transport through the polymer backbones, thereby increasing $\kappa_p$. Similarly, we find that when these polymer chains are compressed (not shown here), $\kappa_p$ decreases, which validates this hypothesis. However, since the number of polymer chains in the system is finite, there is an upper limit to the enhancement of $\kappa_p$. The increasing molecular alignment gradually tapers off at relatively large values of mechanical strain and phonon heat conduction is no longer improved through polymer stretching. Thus, Fig. 2.2(a) also shows that the rate of increase in $\kappa_p$ decreases at higher strain rates.

Figure 2.2(b) presents the influence of transverse strain (along the *y*-direction) on $\kappa_p$. This conductivity decreases as the transverse strain increases. Imposing $e$ = 33.6% reduces the thermal conductivities of PANI, PA and their 1:1 mixture by 24.7%, 11.6% and 23.44%, respectively, with respect to their corresponding unstrained values. A transverse strain induces additional anisotropy by orienting the polymer chains orthogonal to the direction of thermal transport, thus diminishing axial heat conduction. Here, instead of intrachain bonded interactions, interchain intermolecular collisions mainly influence the energy transfer along the *x*-direction. The larger the transverse strain, the lower is the value of $\kappa_p$. The rate of decrease in

$\kappa_p$ is again lowered at larger transverse strains, indicating saturation in the alignment of polymer chains in a similar manner to the results for axial stretching.

### *2.3.2. The effect of polymer combination on thermal conductivity*

Figure 2.2(a) shows that the thermal conductivity of a PANI-PA combination is lower than for either of the pure polymers. Combining these polymers produces a physical mismatch between the characteristic frequencies for the thermal vibrations and intermolecular collisions associated with their two different polymer backbones. One polymer can thus be thought to behave as an impurity within the other, which enhances phonon scattering just as the differences in the masses and force constants of impurity atoms within a bulk material diminish thermal transport [80]. The thermal conductivities of several unstrained polymer combinations are presented in Fig. 2.3, which shows that physical combinations of PANI and PA lower $\kappa_p$ below its value for either of the two pure polymers [81]. The conductivity is lowest for a combined heterogeneous polymer that contains a 2:3 PANI:PA chain ratio. We have previously shown for a binary mixture of crystalline solids that such a behavior is related to their molar mass fractions [81]. While the mass dependence of thermal conductivities for the amorphous polymer combinations do not conform to the analytical expression for crystalline materials due to differences in the major contributors to phonon thermal transport, both systems exhibit a minimum $\kappa_p$ for a specific composition of the binary mixture.

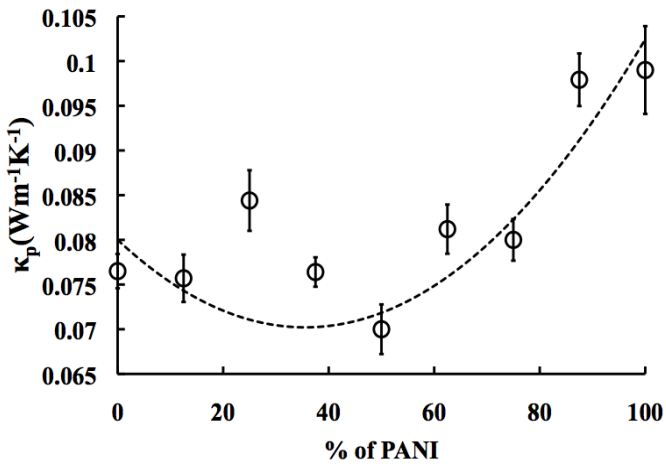


**Figure 2.3:** Variation of $\kappa_p$ for unstretched PANI-PA combinations with respect to the proportion of PANI chains in the mixture where 0% and 100% represent pure PA and pure PANI, respectively. Error bars are determined in a similar manner as for Fig. 2.2.

### *2.3.3. Herman's orientation factor and chain alignment*

Polymer chain alignment in the direction of heat transfer can be characterized through Herman's orientation factor $f_i$. For the $i^{th}$ polymer chain, it is represented as[82]

$$f_i = \frac{3}{2}\left(\frac{1}{B_i}\sum_{j=1}^{B_i}\cos^2\theta_j\right) - \frac{1}{2}, \text{ where } -\frac{1}{2} \le f_i \le 1 \tag{2.1}$$

In Eq. (2.1), $\theta_j$ denotes the angle between the $j^{th}$ bond in the backbone of $i^{th}$ polymer and the $x$-axis, and $B_i$ the total number of bonds in the backbone of the $i^{th}$ polymer chain. When (1) $f_i$ =1, the chains are fully aligned, i.e. all chains are oriented along the $x$-axis, (2) $f_i$ =0, the system is isotropic with no preferential alignment in any particular direction, and (3) $f_i$ =-0.5, all chains are aligned transversely and perpendicular to the $x$-axis. The overall orientation factor $f$ for the entire system is calculated by averaging $f_i$ for all polymer chains in the system.

Figure 2.4(a) shows that axial straining increases $f$ for PANI but that the overall alignment of PA is not significantly influenced by axial strain. The effect of increasing chain alignment on $\kappa_p$ for both polymers is presented in Fig. 2.4(b). In accord with Fig. 2.4(a), $\kappa_p$

increases with increasing PANI chain alignment but straining produces a smaller influence on the PA conductivity due to the lower degree of induced chain alignment. Taken together, Figs. 4(a) and 4(b) again validate the hypothesis that increasing axial strain improves the polymer chain alignment and thus $\kappa_p$.

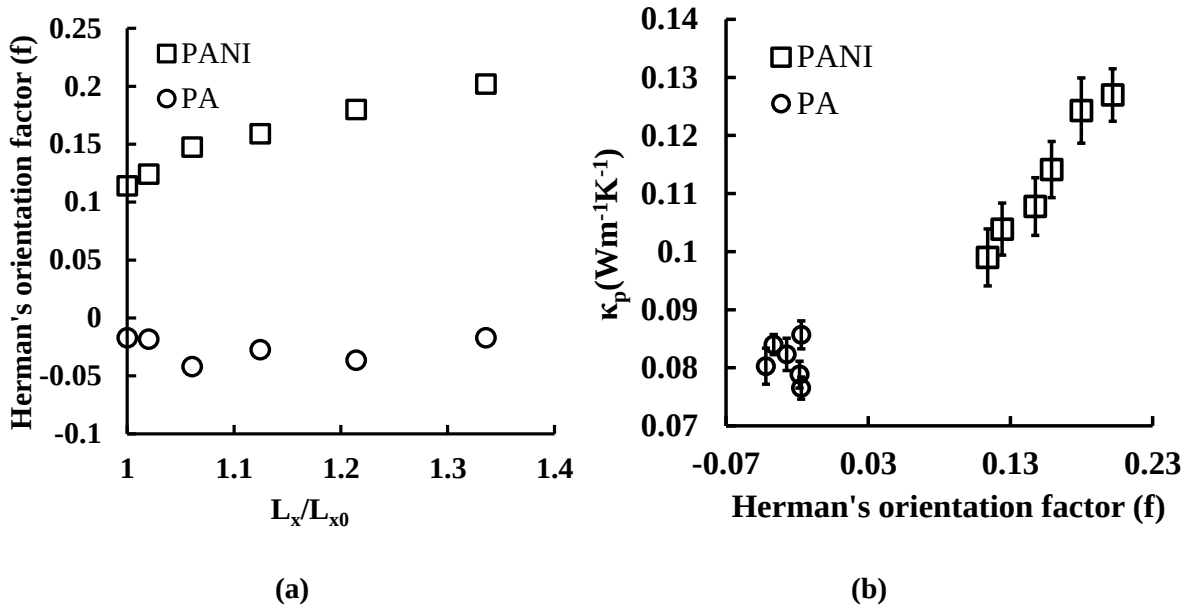


**Figure 2.4:** (a) Variation of Herman's orientation factor *f* calculated along the axial direction for each system along the axial direction with respect to the axial tensile strain for pure PANI and pure PA. The orientation factor ranges from -0.5 (implying an orientation perpendicular to the *x*-axis) to 1 (implying an orientation along the *x*-axis). (b) Variation of $\kappa_p$ with respect to *f* for different PANI and PA axial strains. For (b), error bars are determined in a similar manner as for Fig. 2.2.

Transverse strain decreases the axial polymer chain alignment as illustrated in Fig. 2.5(a). The figure shows that increasing transverse strain reduces the axial chain alignment for PANI but again PA is not as significantly influenced. Consequently, as expected, we observe from Fig. 2.5(b) that the reduction in the alignment of the PANI chains lowers $\kappa_p$ but the corresponding value for PA is not as significantly influenced.

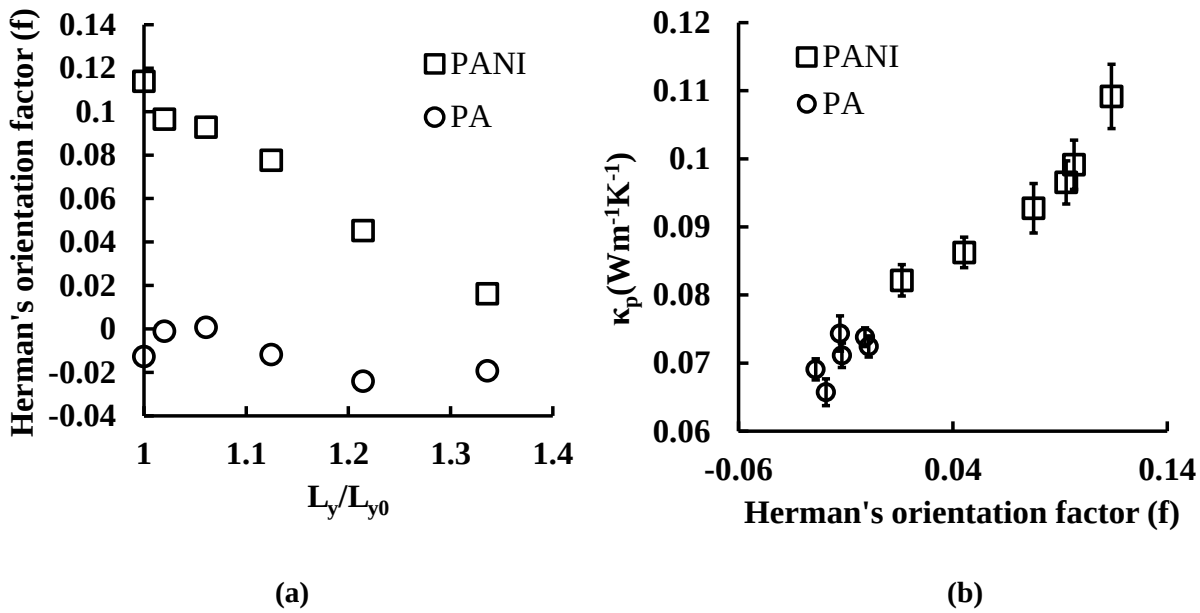


**Figure 2.5: (a)** Variation of $f$ with respect to the tensile strain in the transverse direction for PANI and PA. **(b)** Variation of $\kappa_p$ with respect to $f$ for different PANI and PA transverse strains. For (b), error bars are determined in a similar manner as for Fig. 2.2.

These results consistently demonstrate that the correlations between strain and chain alignment, and in effect the thermal conductivity, are significantly weaker for PA than for PANI. We explain this by emphasizing the differences in their molecular configurations. Figure 2.6 presents representative structures of unstrained individual PA and PANI chains obtained from the simulations. *Ab initio* calculations predict that helical configurations are more energetically stable than planar orientations for PA chains [83], which is also confirmed by our simulations that corroborate the preferred helical form.

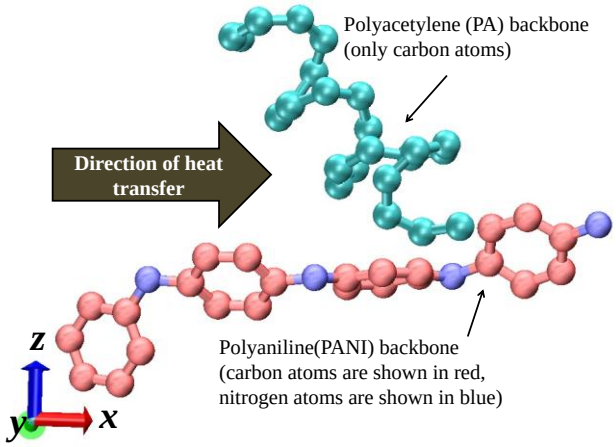


**Figure 2.6:** Representative structures of PA and PANI molecule backbones obtained from our simulations. The backbone of PA is helical while the PANI backbone is more planar.

The different contributions to the total intramolecular energy ($E_{molecule}$) for equilibrated and unstrained pure PA and PANI systems listed in Table 2.2 show a significantly higher $E_{molecule}$ for PA (18151.4 Kcal mole$^{-1}$) than for PANI (7923.5 Kcal mole$^{-1}$).

**Table 2.2:** The different contributions to the total intramolecular energy $E_{molecule}$ of equilibrated and unstrained pure PA and PANI molecules. The torsion energy $E_{torsion}$ is the main contributor to the large difference in the $E_{molecule}$ between PA and PANI.

| System | Bond energy ($E_{bond}$) (Kcal mole$^{-1}$) | Angle energy ($E_{angle}$) (Kcal mole$^{-1}$) | Torsion energy ($E_{torsion}$) (Kcal mole$^{-1}$) | Improper energy ($E_{improper}$) (Kcal mole$^{-1}$) | Total intramolecular energy ($E_{molecule}$) (Kcal mole$^{-1}$) |
|---|---|---|---|---|---|
| PA | 1732.57 | 2722.78 | 13332.71 | 363.34 | 18151.40 |
| PANI | 2065.56 | 2005.68 | 3642.64 | 209.64 | 7923.51 |

The differences in $E_{molecule}$ for PANI and PA mainly arise from their dissimilar torsional energies. That for PA is higher due to its helical configuration as compared to that for the more planar PANI. Consequently, the straining of PA does not cause appreciable chain stretching and

thus does not also improve its chain alignment. On the contrary, PANI reshapes into an elongated structure when stretched, promoting overall chain alignment. The nonplanar PA chain configuration also explains the lower intrinsic thermal conductivity of pure PA as compared to pure PANI.

### 2.4. Summary

Phonon thermal transport can be modified in EC polymers by applying mechanical strain or through binary polymer mixing. Applying an axial tensile strain increases chain alignment in a polymer which improves intrachain phonon transport. While nonbonded interactions are typically reduced by increasing tensile strain in crystals [62, 64], these have a smaller significance in EC polymers where phonon transport is instead more significantly affected by chain alignment. Improving axial chain alignment, e.g., by mechanical straining, increases the overall axial thermal conductivity. Transverse strain promotes the alignment of polymer chains orthogonal to the direction of axial heat transfer and thus reduces the axial thermal conductivity by localizing phonons in neighboring polymer chains. Since the differences in atomic masses and bond force constants are typically responsible for reducing the thermal transport in a binary system, impurities with masses and bond spring constants very different from the bulk material can induce a substantial reduction in the thermal conductivity. Hence, physically combining polymers and exploiting the mismatch between their different characteristic phonon and intermolecular collision frequencies can also be used to lower the overall thermal conductivity. The preferential helical configuration of PA chains results in their lower intrinsic thermal conductivity as compared to PANI which contains relatively more planar polymer backbones. This helicity also diminishes the influence of strain on thermal transport for PA in comparison to the more planar PANI molecules.

## 2.5. Acknowledgement

We thank Professor Aman Haque, Department of Mechanical and Nuclear Engineering, Pennsylvania State University, for introducing us to EC polymers. GB thanks Professor Eugene Joseph, Institute for Critical Technology and Applied Science, Virginia Tech, for explaining the fundamentals of polymer stretching. We thank the Virginia Tech Department of Engineering Science and Mechanics for use of its Linux Compute Cluster.

Chapter 3

# Reducing thermal transport in electrically conducting polymers: effects of ordered mixing of polymer chains

*Reducing the phonon thermal conductivity of electrically conducting (EC) polymers can facilitate their use as potential thermoelectric materials. Thus, the influence of the coupling between the longitudinal and transverse phonon modes on overall thermal conductivity is explored for binary mixtures of polyaniline (PANI) and polyacetylene (PA) chains by considering various geometric polymer mixture configurations. The molecular simulations reveal that an increase in the interfacial area available for transverse interactions between dissimilar chains enhances atomic interactions that are orthogonal to the heat transfer direction. As transverse collisions between PA and PANI chains are enhanced, the motion of longitudinal phonons is disrupted, impeding thermal transport. This enhances phonon scattering and reduces longitudinal thermal transport. While there is a nonlinear decrease in the phonon thermal conductivity with increasing interfacial contact area, there is a corresponding linear growth in the nonbonded interaction energies between the different polymers.*

### 3.1. Motivation and background

EC polymers such as PA and PANI conduct electric current by moving delocalized electrons[51] associated with the $sp^2$ hybridized carbon atoms of the polymer chain backbone. This feature, coupled with their low thermal conductivity $\kappa$, makes them suitable for potential thermoelectric applications [52, 53]. The performance of a thermoelectric material is evaluated through its figure of merit *ZT* that is inversely proportional to $\kappa$. Strategies to manipulate $\kappa$ facilitate the on demand tuning of *ZT*. Since electronic motion in EC polymers is different from the free electron drift observed in metals, energy and charge transport through PANI and PA are only weakly correlated [52, 54]. Atomic vibrations (phonons) and interatomic collisions are the major thermal energy carriers in these polymers. Hence, by reducing the phonon contribution to the thermal conductivity $\kappa_p$, $\kappa$ can be lowered considerably, which in turn enhances *ZT*.

While various strategies have been investigated to increase $\kappa_p$ [55, 84, 85], only a few studies have considered possibilities for its reduction [57, 86]. Unlike crystalline materials, polymer chains exhibit nonlinear anharmonic bonded interactions [57] so that phonon transport through them is strongly dependent on the orientations of their backbone relative to the direction of heat transfer [56, 86]. Polymer chains that are more aligned along this direction offer a smaller resistance to phonon transport. Destroying such an ordered orientation by imposing mechanical strain or mixing dissimilar polymers increases phonon scattering and atomic collisions, and limits the phonon mean free paths, all of which reduce $\kappa_p$ [86].

Longitudinal phonon transport is coupled with transport in the transverse direction [87]. In this letter, we investigate the effect of this coupling in EC polymers and explore its applicability for reducing $\kappa_p$. We contend that enhancing transverse phonon scattering across an interface that is placed parallel to the longitudinal direction of heat transfer should impede transport in this

direction, lowering $\kappa_p$. Various binary PANI-PA polymer mixtures in various geometric configurations are selected to validate this hypothesis using atomistic simulations. Although it is understood how interfacial thermal resistance reduces $\kappa_p$ in superlattice nanostructures [88], discussions of the influence of transverse phonon scattering on $\kappa_p$ are absent from the literature.

### 3.2. Methodology

Nonequilibrium molecular dynamics (NEMD) simulations are employed to determine the thermal conductivity of the PANI-PA configurations using LAMMPS [68]. The term *interfacial area S* denotes the contact area between PANI and PA molecules. Four differently ordered PANI-PA binary polymer combinations are created. These have dissimilar $S$ but the same 1:1 mixture ratio for the numbers of PANI-PA polymer chains. Combinations containing a random distribution of PANI and PA chains as well as those with pure polymers (or 1:0 and 0:1 mixture ratios) are also prepared. Each configuration has a cuboidal geometry of $\Delta X$ nm$\times$ $\Delta Y$ nm$\times$ $\Delta Z$ nm consisting of 64 chains of each of PANI and PA. The geometrical details of these structures, including the values of $\Delta X$ , $\Delta Y$ and $\Delta Z$ for each configuration, are available in the Appendix C. The volume $V = \Delta X \Delta Y \Delta Z$ for all configurations at a specific temperature is comparable (with variation of $\sim$1 % from the mean value). Each polymer chain containing 24 carbon atoms is constructed as a linearly stretched entity that is aligned along the longitudinal direction of heat transfer $x$. The structures are generated with Xenoview [70]. The parameters for the PCFF (Polymer Consistent Force Field) that describe the bonded and nonbonded interactions for these EC polymers are obtained from the literature [69, 70]. Details of the forcefield functions are described elsewhere [86, 89]. For all simulations, periodic boundary conditions are imposed along all three coordinate directions. The VMD package [72] is used to visualize the simulated structures.

### *3.2.1. Energy minimization and equilibration*

First, energy minimization is performed for each configuration using the conjugate gradient technique [68]. The minimized structure is then initialized at the simulation temperature (150, 200, 250, 300, 350 and 400 K for the different cases). This is followed by a two-step process where the configuration is: (1) first heated for 0.1 nanoseconds (ns) to a temperature much higher than the polymer glass transition temperature $T_g$, i.e. from $T$ = 300 K to $T$ = 700 K (for PANI, $T_g$ = 493 K, for PA, $T_g$ = 473 K), and (2) then cooled back to 300 K over 0.1 ns under a canonical (NVT) ensemble using a Langevin thermostat with a coupling time of 0.1 picoseconds (ps). This annealing and tempering relaxes the molecules and removes bond symmetries that could have been artifacts of polymer construction. Next, the configuration is equilibrated under an isothermal-isobaric ensemble (NPT) with $T$ = 300 K and $P$ = 1 atm. where the pressure is controlled by Nosé-Hoover barostat with a coupling time of 1 ps, followed by simulations under the NVT and NVE ensembles, each for 0.2 ns respectively. Upon equilibration, the configuration relaxes to its appropriate mixture density. All simulations use a timestep of 0.001 ps.

### *3.2.2. Determination of $\kappa_p$*

The longitudinal $\kappa_p$ is obtained by implementing the reverse NEMD technique [73]. Along the $x$-wise direction, the exchange of kinetic energies between the coldest atoms in a 0.8950 ($x$) Å × 43.16 ($y$) Å × 36.99 ($z$) Å region, which serves as a heat source in the middle of the domain, with the hottest atoms at the two corresponding $x$-wise boundary regions (that serve as heat sinks with half the thickness of the heat source) provides the heat flux. Figure 3.1 schematically illustrates the direction of heat transfer and shows the steady state temperature distribution along $x$ direction of the polymer configuration 1.

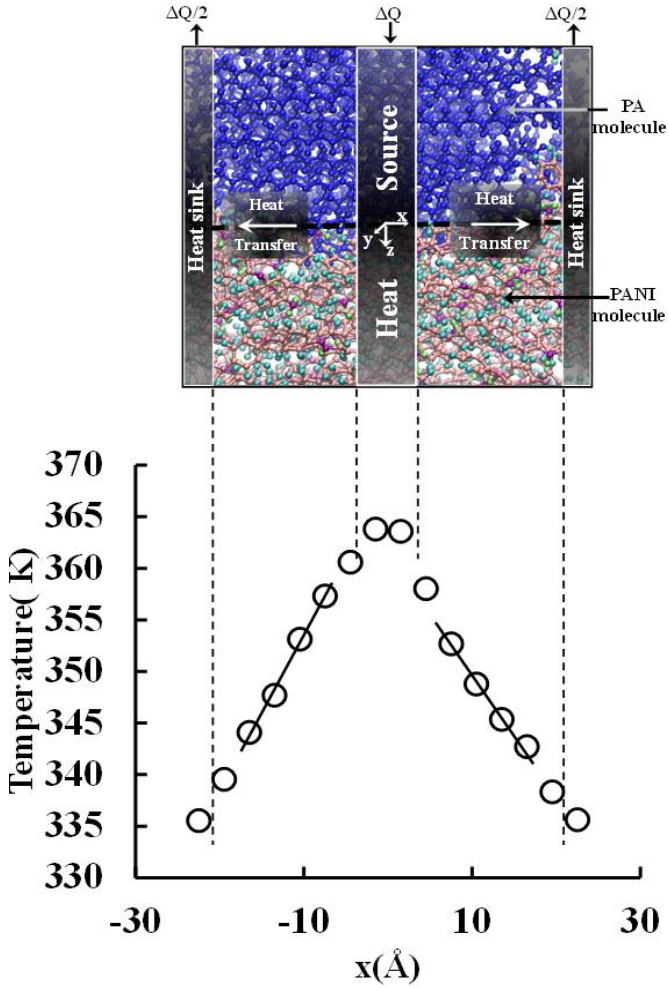


**Figure 3.1:** The top panel illustrates the *x*-*z* cross sectional view of configuration 1 described in the Appendix C. The heat flux *Q* from the source is transferred along the *x* direction through the polymer mixture to the sinks at its two *x*-wise boundaries. The bottom panel presents the simulated temperature profile averaged over 10 samples recorded at regular intervals during the last 1 ns of reverse NEMD simulation. The linear portions of the temperature profiles are used to calculate the average temperature gradient. The locations of the peak temperature(s) correspond to the heat source in the top panel, while the lower temperatures at both boundaries correspond to the two heat sinks.

After the heat transfer reaches steady state, the temperature distribution is sampled over data recorded every 100 ps during the last 1 ns of the 5 ns long NEMD simulations. Temperature

gradients are calculated from the linear portions of the temperature distribution for all the recorded data and a steady state value is obtained from a temporal average over these gradients. The net steady state heat flux transferred from the heat source to the sinks is also determined from a temporal average. Finally, $\kappa_p$ is calculated using Fourier's heat conduction law [74].

### 3.3. Results and discussion

We use $\kappa_{pn}$ to denote the value of $\kappa_p$ normalized with respect to $\kappa_p^{PANI}$ at the corresponding temperature. At room temperature (300 K), $\kappa_p^{PANI}$ is 0.135 $Wm^{-1}K^{-1}$, a value that is obtained by simulating only PANI chains contained in the reference cuboid. Likewise, we calculate $\kappa_p^{PA}$ = 0.088 $Wm^{-1}K^{-1}$ at $T$ = 300 K. For each binary mixture, $S$ (and surface area to volume ratio $S/V$) is obtained by examining the cross section (in $y$-$z$ plane) of the domain taken at the lower boundary of $x$-axis and multiplying the length of the interface by the domain length along $x$-wise direction. As described in the Appendix C, we use an image analysis scheme to identify visually ill-defined contact regions. For a given chain ratio, the random distribution provides the largest $S$.

#### *3.3.1. Effect of $\kappa_{pn}$ on interfacial area*

Figure 3.2 shows the variation of $\kappa_{pn}$ with respect to PANI-PA interfacial area at $T$ =300 K for identical (1:1) chain ratios. As $S/V$ increases $\kappa_{pn}$ decreases. While a typical mixture rule predicts a single value of $\kappa_p$ [86, 90], it is instead evident from Fig. 3.2 that the thermal transport and the conductivity also depend upon the polymer mixture configurations and the magnitudes of their interfacial contact areas. Different configurations alter the magnitude of the transverse interactions between the PANI and PA chains. Increasing the interfacial contact area between these two chains increases phonon scattering through enhanced atomic collisions. This reduces

$\kappa_p$ for the ordered polymer mixture from that of the pure material $\kappa_p^{PANI}$ so that $\kappa_{pn} < 1$. Thus, stronger interfacial interactions lead to smaller $\kappa_{pn}$, which reveal that the higher energy losses due to transverse phonon interactions (or scattering) impede longitudinal thermal transport.

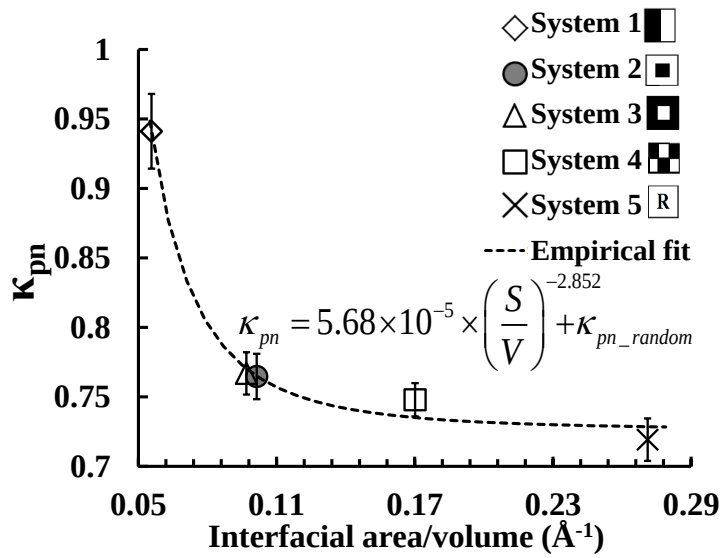


**Figure 3.2:** The variation of the normalized thermal conductivity $\kappa_{pn}$ ($\kappa_p/\kappa_p^{PANI}$) with the interfacial contact area per unit volume ($S/V$) between PANI -PA chains at $T$ = 300 K. The different markers correspond to the binary PANI-PA configurations whose cross sectional configurations are schematically illustrated in the figure legend. Each such schematic reflects the cross sectional ($yz$ plane) view of the binary mixture, perpendicular to the direction ($x$) of heat transfer, where black represents PANI, white PA, and R a random distribution of PANI and PA. Error bars denote the standard error in $\kappa_p$ calculated from ten spatially averaged temperature profiles at intervals of 0.1 ns over the last 1 ns of the simulation and normalized with respect to $\kappa_p^{PANI}$. An empirical fit that asymptotically reaches a limiting value of $\kappa_{pn}$ shows that $\kappa_{pn} - \kappa_{pn,random} \propto \left(\frac{S}{V}\right)^{-2.852}$.

The higher transverse scattering decreases the phonon mean free paths, thereby lowering longitudinal $\kappa_p$. This validates our conjecture that there is a mode coupling between phonons along the transverse and longitudinal directions even for noncrystalline polymer configurations. Since *S/V* increases with diminishing length scale, the effects of these transverse interactions become more pronounced at the nanoscale.

Empirically we find,

$$\kappa_{pn} = 5.68\times10^{-5}\times\left(\frac{S}{V}\right)^{-2.852} + \kappa_{pn,random}\,. \tag{3.1}$$

This fit reaches an asymptotic value for $\kappa_{pn}$, implying that beyond a certain threshold interfacial area (provided by a random mixing of polymers), $\kappa_p$ cannot be lowered any further through polymer mixing. It follows from Eq. (1) that $\kappa_{pn} - \kappa_{pn,random} \propto \left(\frac{S}{V}\right)^{-2.852}$.

### *3.3.2. Effect of temperature*

For amorphous polymers, the dependence of $\kappa$ on temperature is different below and above the glass transition temperature [91]. Below $T_g$, the thermal conductivity increases with temperature due to the reduction in polymer chain entanglement that lowers energy scattering at chain bends. Close to $T_g$, or above it, chain mobility increases as the polymers undergo large movements, thereby creating voids that scatter phonons and lower $\kappa$. The thermal conductivities of PANI and PA also increase below $T_g$ with increasing temperature because of enhanced specific heat [92, 93].

Figure 3.3 presents the variation of $\kappa_{pn}$ and $\kappa_p^{PANI}$ for configurations 1 and 4, described in the Appendix C, at different temperatures. $\kappa_p^{PANI}$ increases with temperature up to 300 K and then slightly decreases close to $T_g$ (493 K), suggesting an increase in phonon scattering from

emerging defects in form of voids. In contrast, $\kappa_{pn}$ for configuration 1 decreases continually with increasing *T*, implying that interfacial interatomic interactions and collisions increase at higher temperatures. However, for the relatively more complex mixture configuration 4 that has larger *S*, $\kappa_p$ does not vary as significantly with temperature. Thus, we conjecture that the reduction in $\kappa_p$ due to transverse phonon scattering is characteristic of a simple ordered mixture configuration and relatively small *S*.

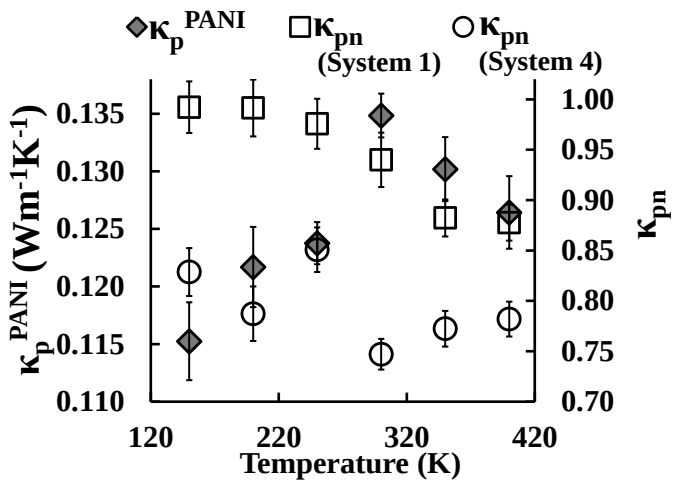


**Figure 3.3:** The evolution of $\kappa_{pn}$ for configurations 1 and 4 and $\kappa_p^{PANI}$ as a function of temperature. Here, $\kappa_p^{PANI}$ is the thermal conductivity of a configuration with only PANI chains. Error bars are determined as described in Fig. 3.2. For $\kappa_{pn}$, error bars at different temperatures are normalized with respect to $\kappa_p^{PANI}$ at the corresponding temperature, whereas for $\kappa_p^{PANI}$ they are in units of $Wm^{-1}K^{-1}$.

Figure 3.4 shows the temperature dependent variation of $\kappa_{pn}$ for the different binary mixture configurations as a function of *S/V*. For each configuration, both *S* and *V* increase by small amounts with temperature due to thermal expansion although the ratio *S/V* remains relatively unaltered (and lies within 2% for a particular configuration). For a specified temperature, $\kappa_{pn}$ typically decreases with increasing *S/V*. While for configuration 1, $\kappa_{pn}$ steadily

decreases with increasing temperature in accord with Fig. 3.3, more complex mixing configurations with larger *S* and enhanced transverse phonon interactions do not exhibit an as organized temperature dependence for $\kappa_{pn}$.

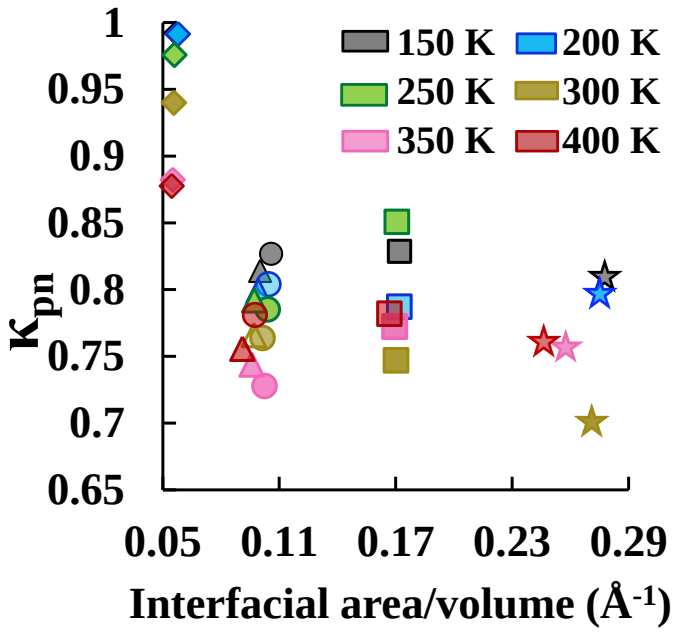


**Figure 3.4:** The variation of $\kappa_{pn}$ as a function of *S/V* between PANI-PA for different temperatures. The value at a specific temperature is obtained by normalizing $\kappa_p$ with respect to $\kappa_p^{PANI}$ at that temperature. Different colors represent the various temperatures while different markers denote the various mixture configurations similar to Fig. 3.2. The *S/V* values for a particular configuration, although comparable at different temperatures, are not equal because of small temperature dependent changes in *S* and *V*. Consequently, data points for the same configuration are not exactly vertically aligned.

### *3.3.3. Interaction energy between PANI and PA*

We evaluate the interaction energies between the two different polymers for each configuration. The interaction energies of PANI molecules with the PA chains consist of *van der Waals* and *Coulombic* energy components. Since the volumes of the different configurations are

comparable, Fig. 3.5 shows that the interaction energies increase with increasing *S*. The reduction in $\kappa_{pn}$ with increases in *S* occurs due to the growth in the locations across which different polymers are able to interact and subsequently scatter the energy transported by phonons and atomic collisions. While $\kappa_{pn}$ is nonlinearly correlated with *S/V* as shown in Fig. 3.2, the interaction energies demonstrate a linear relationship with *S/V*.

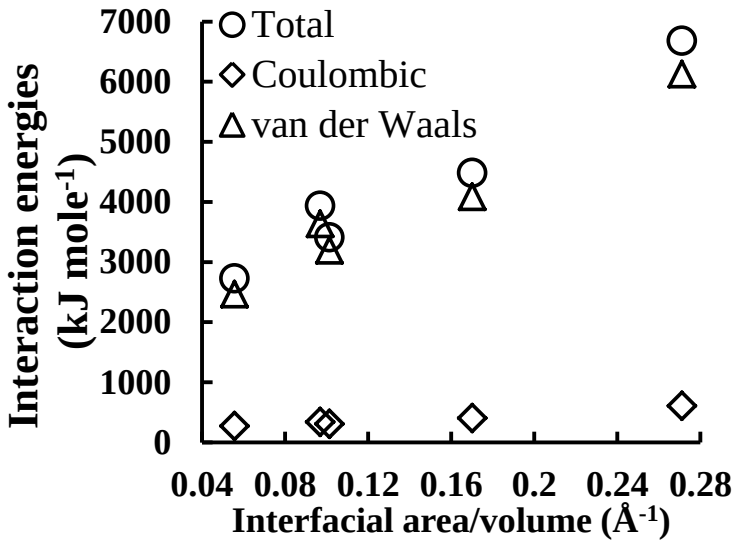


**Figure 3.5**: The variation in interaction energies as a function of *S/V*. The total interaction energy between PANI and PA molecules consists of pairwise interaction and Coulombic energies that are also separately presented here. For all the simulated cases, absolute magnitudes of the energies are presented.

Longitudinal thermal transport occurs due to delocalized phonons traveling along the *x*-direction as well the energy carried by atomic collisions along the same direction. Increasing *S* increases transverse interatomic and polymer interactions. These raise the potential energies associated with the *van der Waals* and Coulombic components, displacing phonons from their longitudinal trajectories, scattering their energies and reducing $\kappa_p$. Thus, the greater the

magnitude of the interaction energies between the PANI and PA chains, the stronger is the impedance to phonon motion along the heat transfer direction (and the lower $\kappa_p$ is).

### 3.4. Summary

In summary, the influence of transverse polymer interactions and interatomic collisions on the longitudinal heat transfer in binary mixtures of PANI and PA chains is investigated. Interfaces that lie parallel to the heat transfer direction reduce phonon thermal conductivity due to transverse phonon scattering. The intrinsic coupling of longitudinal and transverse vibrational modes in these polymers impedes longitudinal thermal transport. $\kappa_{pn}$ has a nonlinear relationship with *S/V*. For simple mixing configurations that generate interfaces with relatively smaller interfacial areas, the enhancement of transverse phonon scattering with increasing temperature further reduces $\kappa_p$ although such a temperature dependent trend does not hold for more complex configurations with larger interfacial areas. The underlying reason for the $\kappa_p$ dependence on *S/V* is illustrated by the linear increase in the intermolecular interaction energies between the two sets of polymer chains with increasing *S*. The enhancement in the interaction energies is due to the increase in transverse polymer interactions and atomic collisions that perturb the longitudinal phonon paths, thereby impeding heat transfer and lowering $\kappa_p$. Such a polymer mixing approach that lowers $\kappa_p$ and increases *ZT* could facilitate the employment of PANI and PA for potential soft-thermoelectric applications requiring high thermal resistance.

### 3.5. Acknowledgement

SP thanks the Virginia Tech Department of Engineering Science and Mechanics for the use of their Linux Computing Cluster (LCC).

Chapter 4

# Thermal rectification in a polymer-functionalized single wall carbon nanotube

*Thermal rectification occurs when heat current through a material is favored in one direction but not in the opposite direction. These materials, often called thermal diodes, have potential application in phononics, i.e., for performing logic calculations with phonons. Rectification obtained with existing material systems is either too small or too difficult to implement practically. Hence, we present a more useful scheme that provides higher rectification using a single wall carbon nanotube (SWCNT) that is covalently functionalized near one end with polyacetylene (PA) chains. This composite structure allows rectification R up to 204%, which is higher than the values reported for SWCNTs. Here,* $R = 100(J_+ - J_-)/J_-$*, where* $J_+$ *and* $J_-$ *are the heat currents for forward and reverse bias respectively. The interatomic interactions in the SWCNT-PA nanocomposite are nonlinear, i.e., anharmonic in nature, which is an established requirement for thermal rectification. Through atomistic simulations, we identify two additional conditions to accomplish thermal rectification at the nanoscale, viz., structural asymmetry and that the influence of this asymmetry on thermal transport is temperature dependent. The optimum temperature difference for achieving the highest thermal rectification with the structure is 40-80 K.*

## 4.1. Motivation and background

Our ability to regulate the flow of electricity is far superior to how we can control heat transfer. Directional control of electric current leads to functional units such as diodes and transistors, which are foundations for modern electronics. An electronic diode allows electric current to flow in a particular direction but behaves as an electrical insulator in the other. For heat transfer, we are however restricted to using materials that behave only as insulators or as conductors in all directions.

The thermal counterpart of an electric diode is a thermal diode or rectifier, which transfers heat preferentially in a particular direction. Rectification of heat current was first observed in 1936[94] when the thermal conductance across a copper oxide-copper interface was found to be directionally dependent. Motivated by the need for better heat removal and thermal management in small electronic devices, research on thermal rectification resumed significantly only about a decade ago.[95] This includes theoretical[96, 97] and experimental[98] investigations, and molecular simulations[38, 99-104] with single materials,[50, 100] and composite materials and interfaces[38, 101].

Thermal diodes could lead to thermal logic gates and eventually a thermal computer.[49, 105] The process of performing logic calculations using phonon transport through thermal logic gates is called phononics for which the possibilities of thermal memory[106] and a thermal transistor[105, 107] have been proposed. Thermal rectification could improve the efficiency of solar water heaters by reducing heat leakage[108] during the night or over winter when the temperature of the collector falls below the water temperature.

Although the rectification of heat current has been established in a one-dimensional non-linear lattice e.g., a Fermi-Pasta-Ulam (FPU),[109] or a Frenkel-Kontorova (FK) lattice,[109,

110] these idealized systems do not represent any existing nanomaterials. When their diameter is reduced so that they are quasi one-dimensional, SWCNTs exhibit one-dimensional thermal behavior e.g. length dependent thermal conductivity.[111] In addition, the interatomic interactions in an SWCNT close to room temperature are anharmonic.[112] The quasi-one-dimensional structure coupled with anharmonic interatomic interactions make SWCNTs an ideal choice to investigate thermal rectification.[37, 113, 114]

Thermal rectification requires local modification of the intrinsic structure of a material,[81] e.g., by varying the masses of carbon atoms[114] or the diameter[113] along the length of an SWCNT. This is extremely challenging in practice and, besides, the rectification obtained is also minor. We propose a more practical and easier to implement thermal rectification scheme where an SWCNT is functionalized with PA near one end while its other end remains pristine. As for an SWCNT, the various bonded interactions in PA are also anharmonic.[57] Thus, an SWCNT-PA nanocomposite satisfies the anharmonicity requirement for thermal rectification. The functionalization of SWCNTs with polymers has been extensively investigated[115, 116] using well-established experimental methods,[117] which makes implementation more practical. Here, we identify the principles that lead to thermal rectification in such a composite structure by employing nonequilibrium molecular dynamics simulations. We also characterize rectification as a function of the temperature difference across the device to determine optimal operating conditions.

## 4.2. Methodology

### 4.2.1. *Nonequilibrium molecular dynamics simulations*

Molecular dynamics simulations can characterize thermal transport in SWCNT-polymer nanocomposites.[116, 117] We employ nonequilibrium simulations to explore thermal

rectification using LAMMPS.[68] Our base case initial structure is presented in the left panel of Fig. 4.1.

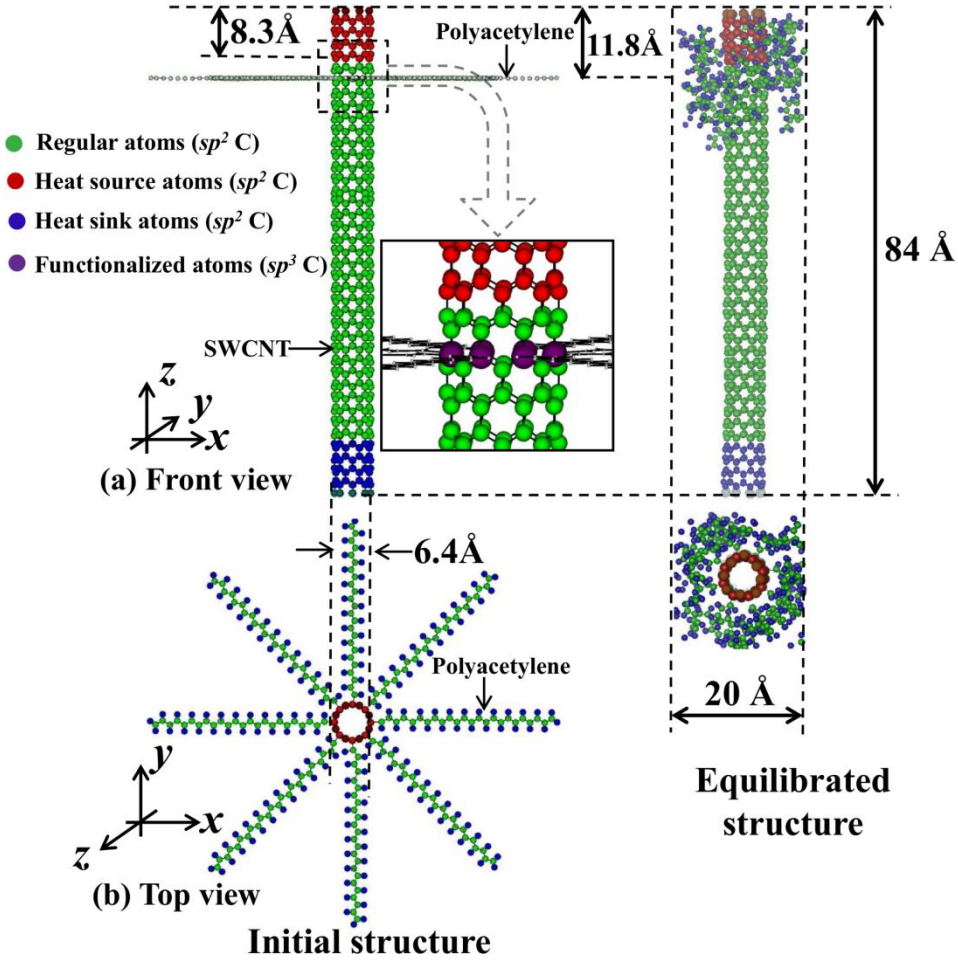


**Figure 4.1:** The base case structure to investigate thermal rectification. The front view is presented in (a) and the top view in (b). The left panel shows the initially prepared structure in Xenoview[70], while the right shows the corresponding structure after equilibration. The PA chains are bonded to SWCNT (zigzag, 8, 0) atoms that are represented in purple in the inset of (a). The carbon atoms of the pristine SWCNT and the PA molecules are in an $sp^2$ hybridized state, respectively indicated in green and blue. The heat source and the sink are of the same dimension and represented by red and blue, respectively.

PA chains are attached to a ring of carbon atoms, indicated by purple in the inset of Fig. 4.1 (a), in a zigzag (8, 0) SWCNT. Each PA chain consists of 24 carbon atoms. The end atoms of the SWCNT are bonded to hydrogen atoms.[118] The SWCNT atoms covalently bonded to PA are in an $sp^3$ hybridized state.[119] Throughout this study, we use the color red to represent hotter and blue to represent colder temperatures. All structures are generated in Xenoview.[70] Periodic boundary conditions are applied along *x* and *y* direction while it is non-periodic in the *z* direction. The equilibrated structure is shown in the right panel of Fig. 4.1. There, the polymers remain attached to the SWCNT and form a layer around it in the vicinity of the functionalization. The anharmonic bonded and nonbonded interatomic interactions in SWCNT-polymer composites are described using the PCFF forcefield[35] that is reported to accurately describe phonon transport in a pristine[120] as well as a chemically functionalized CNT.[121]

The system energy is first minimized using the conjugate gradient technique.[68] The minimized structure is then initialized at 300 K. Next, the system is equilibrated under isothermal-isobaric conditions (NPT ensemble with $T$ = 300 K and $P$ = 1 atm.) for 0.4 nanoseconds (ns) with the pressure being controlled by Nosé-Hoover barostat. The simulations continue (1) under a microcanonical ensemble (NVE) for 0.4 ns with the temperature held constant at 300 K using a Langevin thermostat, (2) under a canonical (NVT) ensemble for 0.4 ns when the temperature is again 300 K using a Nosé-Hoover thermostat, and finally (3) as the system is equilibrated under an NVE ensemble for 0.2 ns. All simulations use a 1 femtosecond (fs) timestep.

### *4.2.2. Thermal transport and rectification ratio*

After equilibration, the atoms forming the heat source are heated to a temperature $T_h$ while the sink atoms simultaneously cooled to $T_l$ under an NVE ensemble. For the base case, $T_h$

=350 K and $T_l$=250 K. Both temperatures are held constant by rescaling the atomic velocities in the source and sink at each timestep.[122] This sets up a heat current $J$, which is calculated from the energy addition and subtraction at the source and the sink, respectively, at each timestep. The energy added to the heat source equals that subtracted from the sink, keeping the system energy constant. To characterize thermal rectification, simulations with the equilibrated structure are conducted for two configurations, viz., forward and reverse bias as shown in Fig. 4.2(a) and (b), respectively.

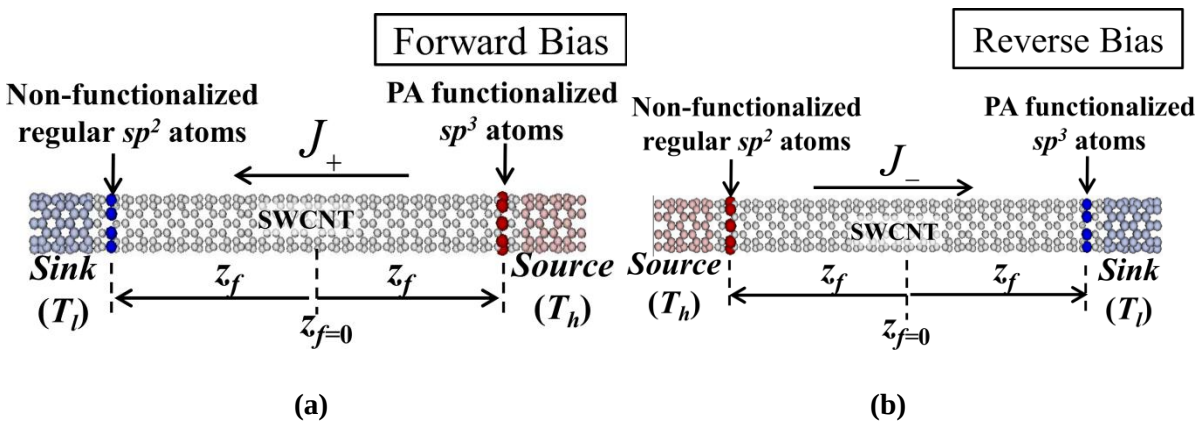


**Figure 4.2:** (a) The forward bias configuration. In forward bias, the heat source is placed at the functionalized end and the heat sink at the pristine end. The temperatures of the heat source and sink are maintained at $T_h$ and $T_l$, respectively. The heat current flowing from the source to sink due to the temperature difference $\Delta T = T_h - T_l$ is denoted by $J_+$. The ring of functionalized $sp^3$ atoms shown in red is placed at a distance $z_f$ from the longitudinal center of the nanotube. Another set of atoms, represented by blue, is selected near the cold end at the same displacement $z_f$ from the center. These two sets of atoms are used to calculate the phonon spectrum presented in Fig. 4.4(a). (b) The reverse bias configuration. In reverse bias, the heat source and sink are at opposite ends as compared to the schematic in (a). The source and sink temperatures are the same as for forward bias leading to an identical $\Delta T$. The heat current is denoted by $J_-$. The red atoms

for forward bias are now represented by blue and the forward bias atoms that were colored blue are now red. They are used to calculate the phonon spectrum in Fig. 4.4(b).

For forward bias, the heat source is placed at the functionalized end whereas for reverse bias that end is instead now a sink. The direction of heat current and phonon propagation is opposite for the two cases, i.e., $J_+$ for forward bias and $J_-$ for reverse bias. The rectification is characterized by the rectification parameter,[99]

$$R = 100(J_+ - J_-)/J_- . \tag{4.1}$$

The temperature difference $\Delta T = (T_h - T_l)$ is held constant for both forward and reverse bias. When the heat transfer simulation is run for 9 ns, a steady state is achieved after 7 ns. The steady state value of $J$ is obtained from a temporal average over ten samples recorded at regular intervals during the last 2 ns.

### 4.3. Results and discussion

The steady state temperature distributions along the SWCNT length for the base case under both forward and reverse bias are presented in Fig. 4.3. The two temperature profiles are dissimilar, implying that heat transfer for the two cases is different. Hence, the system exhibits thermal rectification (here $R$ = 173%). For both cases, the temperature changes rapidly at the location of functionalization. This stark alteration of the local temperature gradient is explained through the significant local change in the thermal conductivity. Covalent functionalization of a SWCNT leads to a local thermal conductivity decrease because it produces greater phonon scattering and leads to a smaller phonon mean free path,[123] as we will show below.

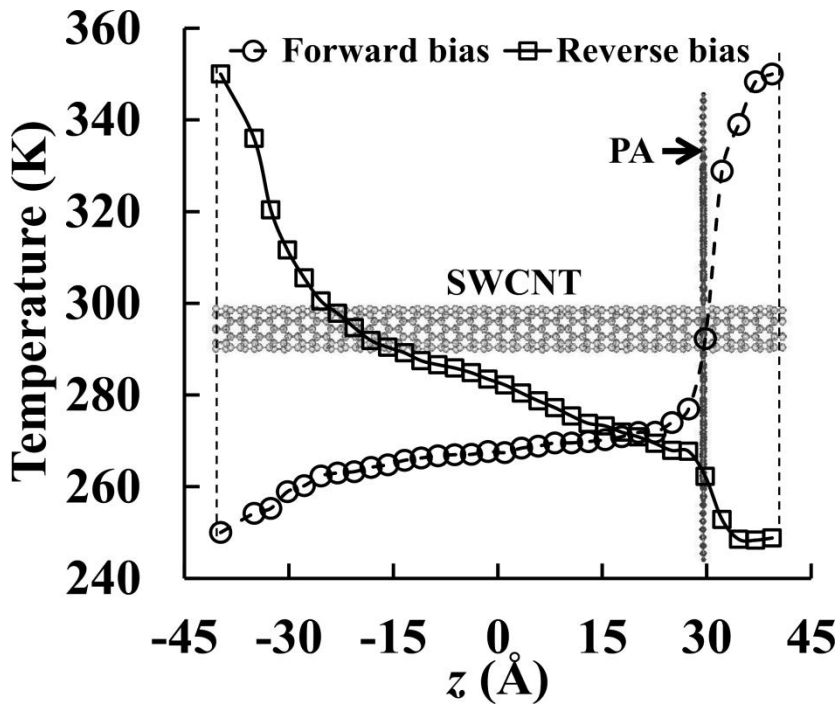


**Figure 4.3:** The steady state temperature profiles along the length of the PA functionalized SWCNT obtained after 9 ns of heat transfer simulations for forward and reverse bias. The temperatures are obtained by averaging over ten such profiles at intervals of 0.2 ns over the last 2 ns of the simulation. We omit error bars for clarity, since the temperature fluctuations are within 0.1 % of the average value, indicating a steady state.

The reasons for the enhanced scattering are as follows. First, the carbon atoms to which the PA chains are covalently bonded are in an $sp^3$ hybridized state while the remaining C-atoms are in an $sp^2$ hybridized state. Therefore, the $sp^3$ C-atoms behave just as defects would in a pristine nanotube, causing phonons to scatter away from them. Second, the longitudinal phonon transport in an SWCNT is coupled with transport in the transverse direction.[124] Consequently, the transverse phonon scattering at the PA-SWCNT interface interacts with phonons traveling in the longitudinal direction, also scattering these and causing a further reduction in the thermal conductivity. Interfacial phonon scattering is temperature dependent since the Kapitza resistance

due to phonon scattering at the interface of two materials is a function of temperature.[125, 126] In forward bias, the functionalized C-atoms and the PA molecules are both at a higher temperature as compared to their respective conditions during reverse bias. Thus, the transverse scattering of phonons between the PA molecules and the functionalized SWCNT atoms, and how this scattering is coupled with longitudinal phonon transport, is different for the two cases. These effects lead to thermal rectification. Since $J_+ > J_-$, $R$ is positive, i.e., the SWCNT favors heat transfer from its functionalized to its pristine end.

### *4.3.1. The origin of thermal rectification: the phonon power spectrum*

To further understand the directional difference in heat currents, we calculate the phonon power spectrum at the two ends of the SWCNT. A spectral overlap over different portions of a material diminishes scattering and facilitates more efficient phonon energy exchange between these segments. A mismatch in the spectra enhances phonon scattering on the other hand, which lowers the thermal conductivity.[127] The steady state spectra at the two ends of the SWCNT in forward and reverse bias are shown in Fig. 4.4(a) and (b), respectively. A spectrum is calculated through the Fourier transform of the velocity autocorrelation function obtained from the corresponding MD trajectories.[38, 128] In forward bias, two spectra are obtained, one for the ring of functionalized $sp^3$ atoms near the hot end of the nanotube and another for the ring of regular $sp^2$ carbon atoms near its pristine cold end. Both atom sets lie equidistant from the center of the SWCNT, as shown in Fig. 4.2(a). In reverse bias, the spectra for the two ends are based on the same sets of atoms although, for this case, the $sp^3$ and $sp^2$ atoms instead lie at the cold and hot ends, respectively.

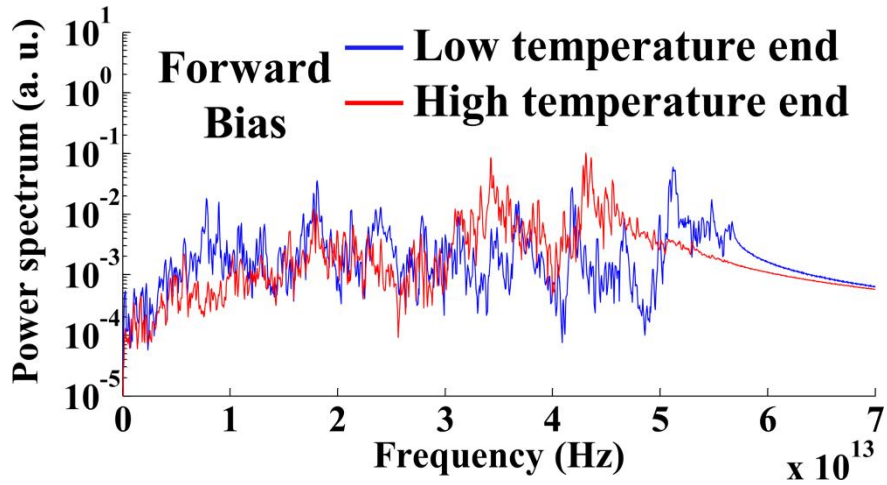


(a)

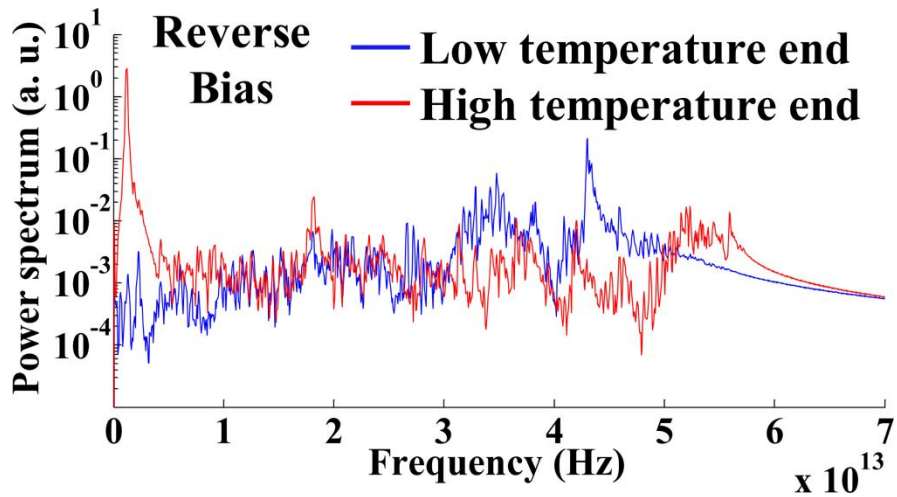


(b)

**Figure 4.4:** The steady state phonon power spectra for the base case for **(a)** forward bias and **(b)** reverse bias. The red and blue spectra in (a) correspond to the red and blue atoms in Fig. 4.2(a) and likewise for (b) corresponding to Fig. 4.2(b). Since the velocity autocorrelation is normalized, the power spectrum obtained is a dimensionless quantity. The ordinate has a logarithmic scale.

The spectra for the cold ends in both forward and reverse bias are similar while those at the hot ends differ significantly for the two bias cases. For instance, as shown in Fig. 4.4(b),

during reverse bias, the hot end spectrum contains a distinct low frequency peak, which is missing from the corresponding hot end spectrum for forward bias that is shown in Fig. 4.4(a). Hence, the spectral overlap between the two ends of the SWCNT is different in forward and reverse bias. There is a greater spectral mismatch during reverse bias, which reduces the heat exchange between the hot and cold ends due to increased phonon-phonon scattering. Consequently, $J_- < J_+$.

Since the spectral mismatch between the ends of a pristine SWCNT is uninfluenced by switching the locations of the heat source and the sink, there is no thermal rectification. Functionalization imposes additional constraints on the motion of the C-atoms, modifying the phonon spectrum by filtering out certain phonon frequencies. In effect, functionalization manifests itself as a band-pass filter. The range of allowable frequencies for this filter is temperature dependent. The low frequency peak in the hot end spectrum is filtered in forward bias when the functionalization, or filter, is placed near the heat source. When placed near the heat sink in reverse bias, the filter does not significantly alter the cold end spectrum. This band pass filtering is a fundamental cause of thermal rectification.

### *4.3.2. The role of structural asymmetry*

Structural asymmetry with respect to the heat source and sink is also a necessary condition for nanoscale thermal rectification.[113] The asymmetry shown in Fig. 4.2 depends upon $z_f$. Structural symmetry increases as $z_f$ is reduced with the material being fully symmetric when $z_f = 0$. Then, the functionalization is equidistant from the source and the sink. The variation of $R$ with respect to $z_f$ is presented in Fig. 4.5. As expected, the reduction in $R$ with decreasing $z_f$ reinforces the inference that thermal rectification is a strong function of symmetry. Again, the

modification of the phonon spectrum due to functionalization differs for forward and reverse bias, except, of course, when $z_f = 0$.

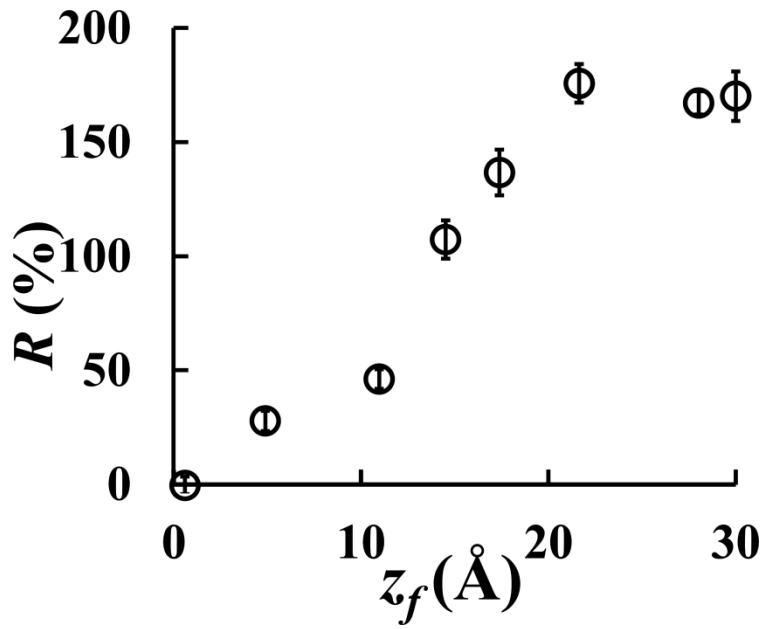


**Figure 4.5:** The rectification parameter $R$ (Eq. (4.1)) plotted against $z_f$. Error bars are determined from ten samples recorded at intervals of 0.2 ns during the last 2 ns of the simulations after steady state is achieved.

*4.3.3. The diode characteristics*

Diode performance is depicted through a typical characteristic, which plots $J$ versus $\Delta T$, as shown in Fig. 4.6(a). Positive and negative values of $\Delta T$ correspond to the forward and the reverse bias conditions, respectively. The range of $\Delta T$ spans two regions, viz., operating and breakdown. In the operating region, whereas $J_+$ increases with increasing $\Delta T$, the magnitude of $J_-$ remains relatively small and also does not change as significantly. Therefore, the difference ($J_+ - J_-$) rises with increasing $\Delta T$. This also increases $R$, as shown in Fig. 4.6(b). In the breakdown region, increasing $\Delta T$ increases $J_-$ but here $J_+$ also rises at the same rate. Consequently, increasing $\Delta T$ decreases $R$ in this region. This characteristic resembles that of a

typical electrical diode that has distinct operating and breakdown regions. The critical value of $\Delta T$ for transition from the operating to the breakdown region is ~80 K, as is evident from Fig. 4.6(a) and (b). The optimum values of $\Delta T$ for the highest rectification lie in the rage 40-80 K. The maximum value of $R$ is 204 %, which is higher than values reported in the literature[37, 114, 129],[130] for thermal rectification with SWCNTs.

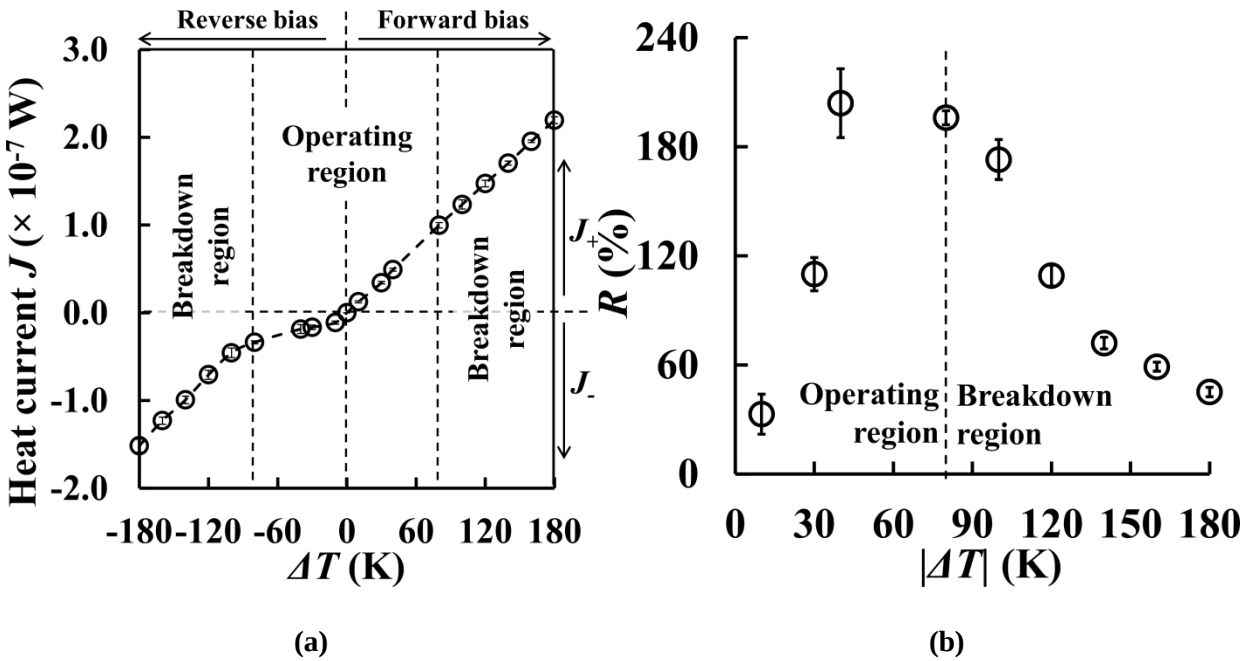


**Figure 4.6: (a)** The diode characteristic, i.e., a plot of heat current $J$ *vs.* $\Delta T$. Positive and negative $\Delta T$ values represent forward and reverse bias, respectively. **(b)** The variation of $R$ with respect to $|\Delta T|$. Error bars are calculated in a similar manner as for Fig. 4.5.

## 4.4. Summary

A SWCNT functionalized by PA can function as a thermal diode. This structure shows larger thermal rectification than existing concepts. The rectification occurs due to the difference in heat currents originating from the dissimilar spectral mismatches during forward and reverse bias. Functionalization behaves as a band-pass filter, allowing a range of phonon frequencies to pass through and thus alter the phonon spectrum in the vicinity of functionalization. Such an alteration of the phonon spectrum is temperature dependent. When placed near the sink i.e., in reverse bias, the filter alters the cold end phonon spectrum so that there is a greater spectral mismatch between the hot and cold ends, thereby increasing phonon scattering as compared to when its placement near the source during forward bias. Structural asymmetry also influences the rectification. Placing functionalization at the center of the nanotube makes the structure symmetric, resulting in no rectification at all. The $J$-$\Delta T$ characteristic obtained for the thermal diode resembles that for an electrical diode. The operating range is $\Delta T$ = 0-80 K when $R$ increases with respect to $\Delta T$ with optimal rectification between 40-80 K when $R$ is maximum. Beyond this range, increasing $\Delta T$ leads to a breakdown of thermal rectification.

## 4.5. Acknowledgement

This research was supported by a grant from the National Science Foundation (CBET 1246611). We thank the Virginia Tech Department of Engineering Science and Mechanics for the use of its Linux Computing Cluster.

Chapter 5

# Thermal AND gate using a monolayer graphene nanoribbon

*A thermal AND gate performs logic calculations with phonons. We present the first ever implementation of a thermal AND gate using two identical asymmetric graphene nanoribbon (GNR) based thermal diodes. Employing molecular dynamics simulations, we investigate the properties of the AND gate and compare them with those for an electrical AND gate. The gate has two input terminals, a biasing and an output terminal. The thermal analog of voltage for a thermal AND gate is temperature. We represent the digital logic 1 and 0 states by predefined 'HIGH' and 'LOW' temperatures, which for our base case are 300 K and 100 K, respectively. By applying different 'HIGH' and 'LOW' combinations at the input, we monitor the output. The effectiveness of the gate in producing an output that conforms to AND operations for the specified inputs is measured as* $\varepsilon$ *= (Output – LOW)/ (HIGH – LOW). For thermal inputs 1 – 0, 0 – 1 and 0 – 0, the thermal AND gate produces* $0 \le \varepsilon \le 0.275$*, which is comparable to the* $0 \le \varepsilon \le 0.12$ *range for a silicon electrical diode. The thermal gate mechanism originates through thermal rectification in its two diodes due to asymmetric phonon boundary scattering, which is only effective at the nanoscale and at temperatures much below room temperature. The gate has a fast switching time of ~100 ps due to the high phonon velocity in graphene.*

## 5.1. Motivation and background

Logic calculations performed with phonons are referred to as phononics [49]. The functional building block of phononic devices is the thermal diode. It allows heat to flow in a single direction and prevents its flow in the opposing direction [103-105]. Experimental [98], theoretical [96, 97] and molecular simulation [38, 99-102] investigations have proposed different material systems for thermal diodes, e.g., mass graded CNT [114], the polyethylene-silicon interface [38], carbon nanocone [100], graphene nanoribbon (GNR) [99], and solid-fluid interfaces [103, 104]. However, more complex structures such as thermal logic gates, thermal memory [106] and thermal transistors [105, 107, 131] that combine thermal diodes have been sparingly investigated.

In most materials, thermal rectification depends on phonon transport at the nanoscale. At this scale, interfaces and boundaries scatter phonons and impede thermal transport [125]. Hence, the design of phononic circuits to produce prescribed interfacial and boundary scattering is a challenging task. Prior investigations of thermal logic gates [132] have been based on ideal non-linear atomic chain segments which do not exactly correspond to a real material. For any logic device, the ‘HIGH’, i.e., digital logic 1 and ‘LOW’, or digital logic 0 states must be established. For a typical electrical diode, a voltage range determines these states. Since the analog of voltage for a thermal logic device is temperature, the ‘LOW’ and ‘HIGH’ states of a thermal device are similarly prescribed by a temperature range.

We present the first design of a thermal AND gate using a GNR thermal diode as its fundamental building block. The asymmetric shape of the GNR diode produces asymmetric phonon boundary scattering. Thus, the diode exhibits high rectification, described as the ratio of forward to reverse current. Using molecular dynamics (MD) simulations, we characterize the

performance of the thermal AND gate by investigating the fundamental behavior of the gate, identifying optimal operating conditions, and characterizing its switching behavior.

## 5.2. Methodology

Molecular simulations have described thermal transport in a monolayer graphene sheet and GNRs [133-137]. Typically, in such simulations, the atoms at the two edges of the graphene sheet are held fixed. The next few atomic layers at both ends are used as the heat source and sink to initiate heat transfer with a non-equilibrium molecular dynamics (NEMD) simulation. We also adopt this standard methodology.

The basic design of a typical GNR diode is shown in Fig. 5.1(a) where higher heat current flows from the wider to the narrower terminal, i.e., $J_+ > J_-$.

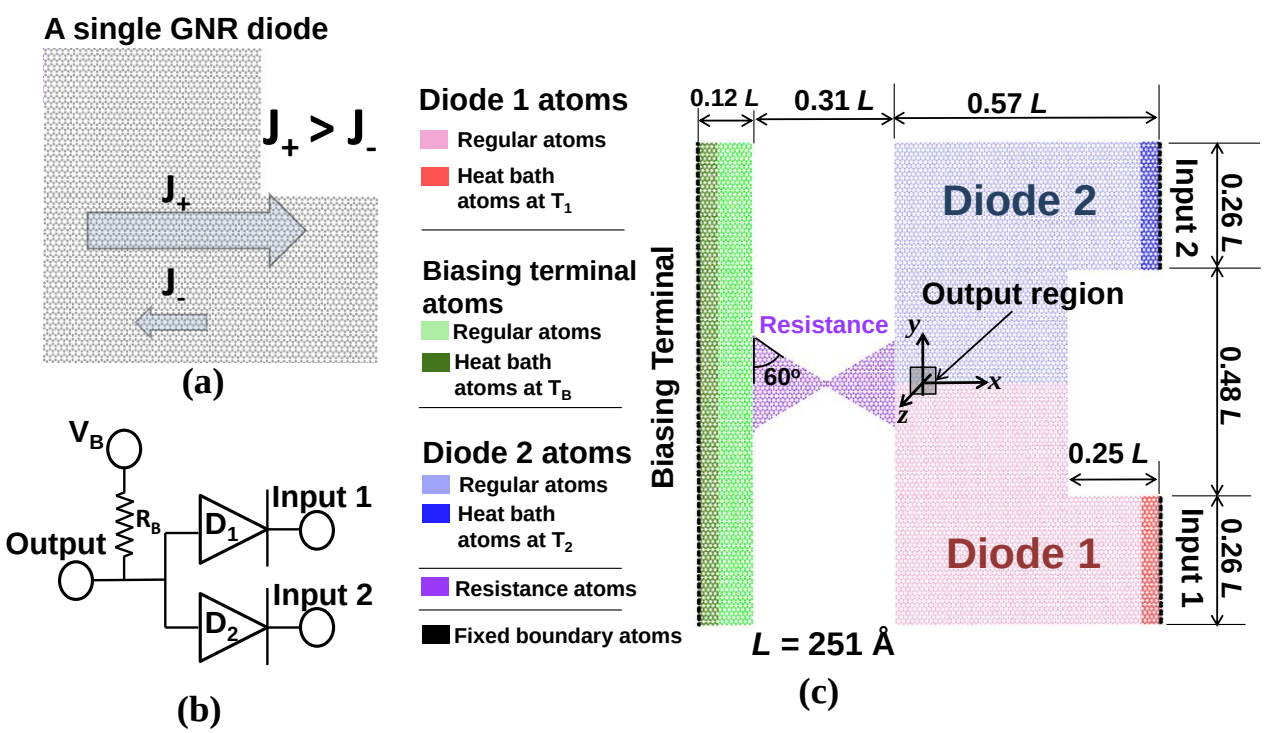


**Figure 5.1:** (a) A single GNR diode is shown with heat currents $J_+$ and $J_-$. Here, $J_+ > J_-$, which indicates that the GNR diode prefers heat current to flow from the wider to the narrower

terminal. (b) A typical electrical AND gate implemented by two electrical diodes is shown. It has two input terminals, an output and a biasing terminal, which is connected to the output terminal via a biasing resistance. (c) The thermal AND gate analogous to the electrical AND gate of Fig. 5.1(b) is presented. The gate consists of two GNR diodes shown in red and blue and is identical to the one shown in Fig. 5.1(a). These two diodes are connected to a biasing terminal via a converging-diverging region of very narrow section serving as biasing resistance. Similar to the electrical diode, it also contains two input terminals, an output terminal and a biasing terminal. The edge atoms of the inputs and the biasing terminal are held fixed. The next eight layers of atoms are bath atoms shown in deeper shades of red, blue and green. The entire diode consists of 15372 atoms.

In Fig. 5.1(b) a typical electrical AND gate implemented by two diodes $D_1$ and $D_2$ is shown. It has two input terminals, an output terminal and a biasing terminal. The device has predefined 'HIGH' and 'LOW' voltage ranges. The output voltage is 'HIGH' when both the inputs are 'HIGH'. The biasing terminal, usually maintained at 'HIGH', is connected to the output terminal through a biasing resistance. Figure 5.1(c) presents the thermal analog of the electrical AND gate of Fig. 5.1(b). It is implemented through the two GNR diodes shown in red and blue and the biasing terminal represented by green. The two diodes are connected to the biasing terminal through a very narrow region shown in purple that offers high thermal resistance due to strong boundary phonon scattering. The entire system consists of 15372 C atoms.

The edge atoms of the input and biasing terminals in Fig. 5.1(c), shown in black, are held fixed. The next eight atomic layers, shown in deeper shades of red, green and blue are used as heat baths that are maintained at fixed temperatures by a Nosé-Hoover thermostat, which is used to initiate heat transfer in GNR investigations [137-139]. Results of MD-based studies of thermal transport in nanostructures can be sensitive to the size of the heat bath due to the presence of a

localized edge mode (LEM) of phonons that lie close to the boundaries [140]. We use eight layers of heat bath atoms, which are sufficient for removing this LEM effect on thermal transport [137, 140]. At steady state, the device output is recorded as the average temperature in the 1 nm × 1 nm square region centered on the origin. All structures are generated using VMD [72] and Xenoview [70].

The interatomic interactions between carbon atoms in graphene are described by the second generation reactive bond order potential (REBO II) [141] which accurately reproduces graphene properties, particularly bond strength and anharmonicity [142]. We apply nonperiodic boundary conditions in all directions and a timestep of 1 femtosecond (fs). All simulations are performed using LAMMPS [68]. The system energy is first minimized using the conjugate gradient technique [68]. The minimized structure is then initialized at 300 K. Next, the system is equilibrated under canonical (NVT) ensemble at $T$ = 300 K for 0.2 nanoseconds (ns) with the temperature being controlled by Nosé-Hoover thermostat that has a coupling time of 1 picosecond (ps). Finally, the system is equilibrated under an NVE ensemble for 0.2 ns.

After equilibration, heat transfer is initiated by Nosé-Hoover thermostats that have the same coupling time of 1 ps for the heat bath atoms at the inputs and the biasing terminal. The heat currents $J_{i1}$, $J_{i2}$ and $J_b$ associated with the thermostats at input 1, input 2 and the biasing terminal are calculated from the rate of energy added or subtracted to each thermostat. At steady state, which is generally achieved after $2\times10^6$ steps, i.e., 2 ns, the heat currents become steady, fluctuating only within ~3 % of their average values.

## 5.3. Results and discussion

### *5.3.1. Temperature distribution*

For the base case, we assume 300 K to be 'HIGH' and 100 K as 'LOW' for the system. The biasing terminal is also maintained at 'HIGH'. The temperatures at input 1, input 2, biasing and output terminals are designated as $T_1$, $T_2$, $T_b$ and $T_o$, respectively. Four different $T_1$-$T_2$ combinations are simulated, *viz*., 0 - 1, 1 - 0, 1 - 1 and 0 - 0. For the 1 - 0 case, i.e., when $T_1$ = 300 K, $T_2 = 100$ K, diode 2 is forward biased and diode 1 is reverse biased. For this case, the *y*-averaged temperature distribution along *x* in the two diodes is shown in Figs. 5.2(a) and 5.2(b).

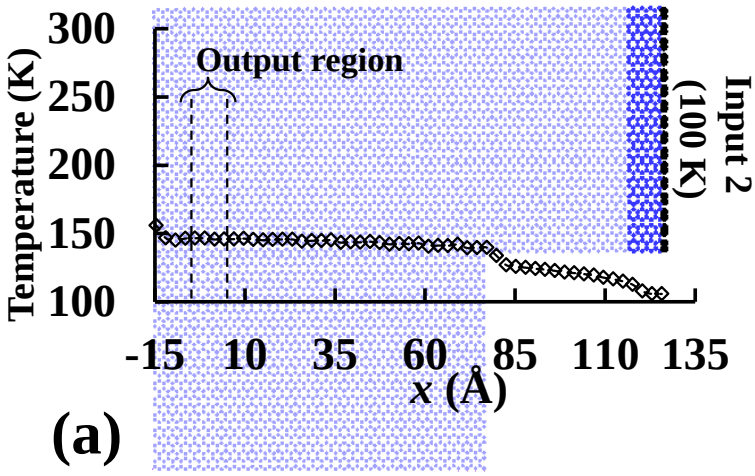


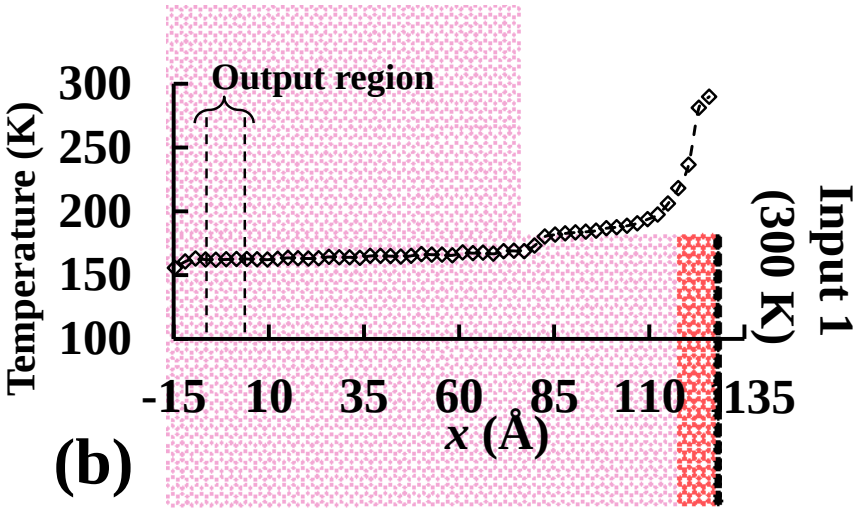

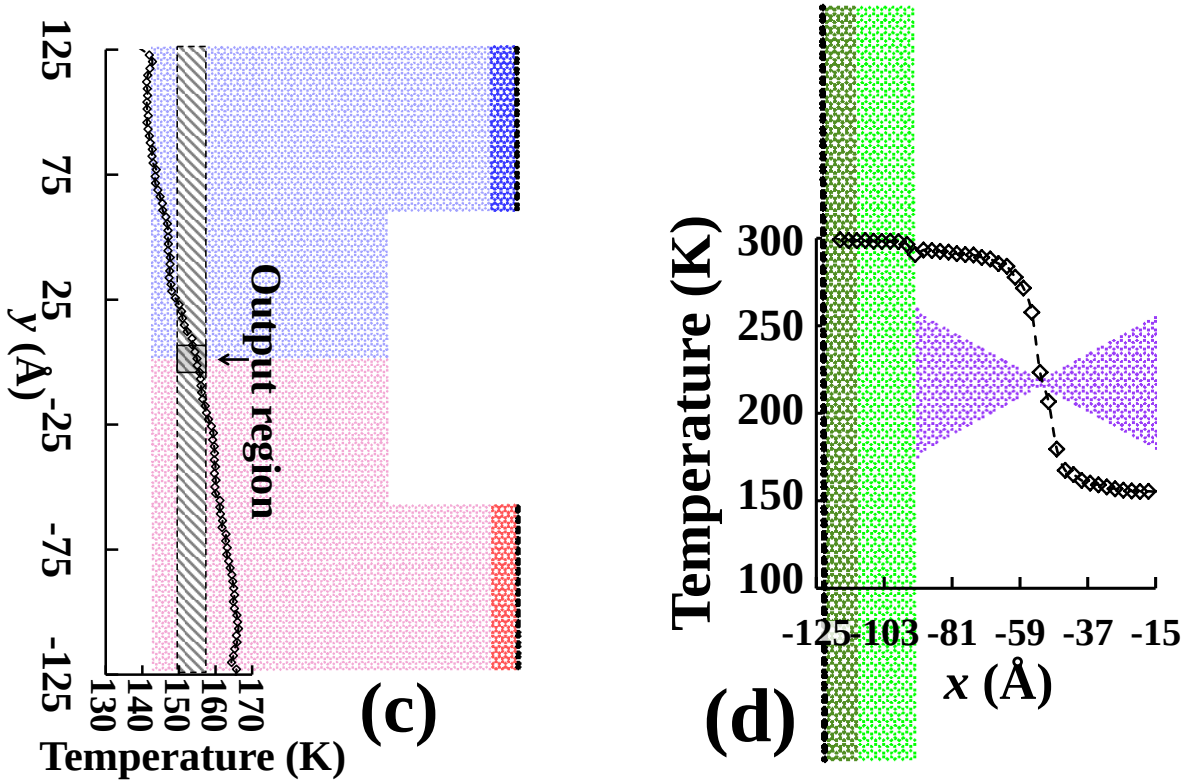


**Figure 5.2:** (a) The *y*-averaged temperature distribution along *x* at steady state in diode 2 is shown. The input 2 terminal is maintained at 'LOW", i.e., 100 K. The temperature does not change appreciably within the *x* bounds of the output region, i.e., $\pm 5$ Å. (b) The *y*-averaged temperature distribution along *x* at steady state for diode 1 is shown. The input 1 terminal is held at 'HIGH", i.e., 300 K. Again, the temperature changes very little within the *x* bounds of the output region. (c) The *x*-averaged temperature distribution along *y* at steady state is plotted in the shaded region which extends from -5 to 5 Å along *x*. (d) the *y*-averaged temperature distribution along *x* in the biasing terminal and the resistance is shown. For all temperature plots, error bars are not shown for sake of presentation clarity. The variations of temperature at steady state are within 1% of their average value.

For both diodes, the temperature remains almost constant within the *x* bounds of the output region (illustrated by dotted lines). The *x*-averaged temperature distribution along *y* in the shaded region including the output is shown in Fig. 5.2(c). Again, within the *y* bounds of the output

region, the temperature does not change appreciably. The steady state average output temperature $T_o$ = 155 K with any spatial or temporal fluctuations lying within 1%. The temperature distribution in the biasing terminal and the resistance is shown in Fig. 5.2(d). The large drop across the narrowest section of the resistance is due to strong boundary phonon scattering.

### *5.3.2. Determination of 'LOW' and 'HIGH' ranges*

In an ideal AND gate, when either of the inputs is low, the expected output is 'LOW'. To represent the effectiveness of the AND gate, we define an output parameter

$$\varepsilon = (\text{Output} - \text{LOW})/\ (\text{HIGH} - \text{LOW}). \tag{5.1}$$

An ideal AND gate should demonstrate $\varepsilon = 0$ for 0 - 1, 1 - 0 and 0 - 0 inputs. The inputs and their corresponding outputs in terms of $\varepsilon$ for the simulated base case thermal AND gate are presented as the truth table in Table 5.1.

In classical MD simulations, the temperature,

$$T_{MD} = \frac{2}{3Nk_b}\sum_i \frac{p_i^{\,2}}{2m_i}. \tag{5.2}$$

Here, $T_{MD}$ represents temperature calculated through the MD simulation, $N$ the total number of atoms considered, $k_b$ the Boltzmann constant, and $p_i$ and $m_i$ the momentum and mass of $i^{\text{th}}$ atom.

**Table 5.1: The truth table**

| Input 1 | Input 2 | Output ( ε) | Ideal |
|---|---|---|---|
| 1 | 0 | 0.270 | 0 |
| 0 | 1 | 0.275 | 0 |
| 0 | 0 | 0.025 | 0 |
| 1 | 1 | 0.993 | 1 |

When the system temperature is lower than the Debye temperature of the material, quantum effects on thermal transport can no longer be neglected [143]. By equating the total energies obtained from the quantum and classical representation of the system, we relate the two temperatures $T_{MD}$ and $T_Q$ [138],

$$T_{MD} = \frac{2T_Q^3}{T_D^2} \int_0^{T_D/T_Q} \frac{x^2}{e^x - 1} dx, \tag{5.3}$$

where $T_D$ represents the Debye temperature and $T_Q$ the quantum corrected temperature. Since the reported range of Debye temperature for graphene varies, from between 1000-2300 K [144-146] to 322 K [50, 139, 147]. the benefit of employing this correction is ambiguous. We assume the Debye temperature to be 322 K since this temperature has been used for quantum corrections for thermal rectification studies in single layer GNRs [139, 147]. The value of $\varepsilon$ for a 1–0 input increases slightly from 0.275 to 0.28 as a result of the correction. This small ~2% change suggests a weak influence of the quantum correction. Hence, for the following discussion, we will neglect its influence.

In a practical implementation of an electrical AND gate, when either of the inputs is 'LOW', the output voltage is higher than 'LOW' due to a small voltage drop $V_D$ in a forward biased diode. For instance, a typical silicon diode in forward bias has $V_D$ = 0.6 V.[148] With 5 V as 'HIGH' and 0 V as 'LOW',[149] the output of the AND gate shown in Fig. 5.1(b) is 0.6 V, or $\varepsilon$ = 0.12. Thus, the output is designated as 'LOW' if $0 \le \varepsilon \le 0.12$. For the thermal AND gate output shown in Table 1, this range is $0 \le \varepsilon \le 0.275$, or $100\ \mathrm{K} \le T_o \le 155\ \mathrm{K}$. From Fig. 5.2(b), the forward bias temperature drop $\Delta_D$ across diode 2 is 55 K, which is much lower than the 145 K drop across diode 1 that is reverse biased. Similarly, the output is designated 'HIGH' if

$0.99 \le \varepsilon \le 1$. An effective AND gate must have very narrow ranges for 'HIGH' and 'LOW'. We define the upper limit of the 'LOW' range as $\tilde{\varepsilon}$, i.e., $0 \le \varepsilon \le \tilde{\varepsilon}$ where $\tilde{\varepsilon}$ corresponds to the output $\varepsilon$ for the 1–0 or 0–1 cases. The output $\varepsilon$ for the 0–0 case lies between 0 and $\tilde{\varepsilon}$. For the current AND gate, $\tilde{\varepsilon}$ = 0.275. The smaller the value of $\tilde{\varepsilon}$ the better is the gate. The least effective AND gate will have $0 \le \varepsilon \le 0.5$ and $0.5 \le \varepsilon \le 1$ as 'LOW' and 'HIGH' ranges. If $\tilde{\varepsilon} > 0.5$, the device no longer operates as an AND gate.

### *5.3.3. Heat current flow*

Figure 5.3 shows the heat current in the gate at steady state. The total current $J_{i2}$ flowing into input 2 equals the sum of the currents $J_{i1}$ from input 1 and $J_b$ from the biasing terminal, thereby satisfying energy conservation. $J_{i1}$ = 0.9 $J_{i2}$ is a leakage current flowing from the 'HIGH' to 'LOW' terminals.

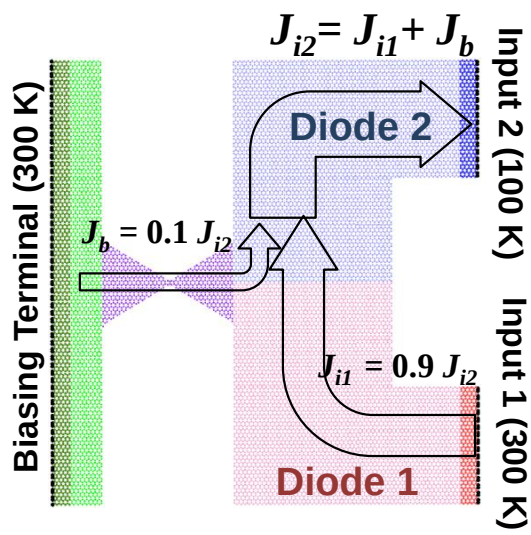


**Figure 5.3:** The heat currents flowing in the gate at steady state are shown. The heat current $J_{i2}$ into the diode 2 equals the sum of heat currents $J_{i1}$ from the diode 1 and $J_b$ from the biasing terminal.

This is different from an electrical AND gate where there is no leakage current flowing from the 'HIGH' to 'LOW' terminals. A thermal diode has a relatively smaller reverse bias resistance as compared to an electrical diode. The much higher reverse bias resistance in a typical electrical diode leads to a rectification ratio $J_+ / J_-$, i.e., a forward to reverse bias current ratio of about 1000 [150]. The highest rectification ratio reported for a thermal diode is 4.5 [99]. With the GNR diode of Fig. 5.1(a) it is 1.94. This low rectification ratio leads to a significant leakage current from the 'HIGH' to 'LOW' terminals.

### *5.3.4. The phonon spectra*

To understand why the temperature drop across diode 2 is smaller than for diode 1, we compare the phonon power spectrum for atoms contained in different sections of the two diodes. An overlap in the phonon spectrum over different portions of a material facilitates phonon motion without scattering while a mismatch in the spectra produces scattering which lowers the phonon thermal conductivity and impedes phonon transport [127]. The spectrum $P(f)$ is determined by taking the Fourier transform of the velocity autocorrelation function obtained from the MD trajectories [38, 128]. For each diode, we calculate two spectra, one for the layer of atoms adjacent to the heat bath (layer C for diode 1 and layer B for diode 2) and another for the layer of atoms at $x = 0$ (layer D for diode 1 and layer A for diode 2), as shown in Figs. 5.4(a) and (b).

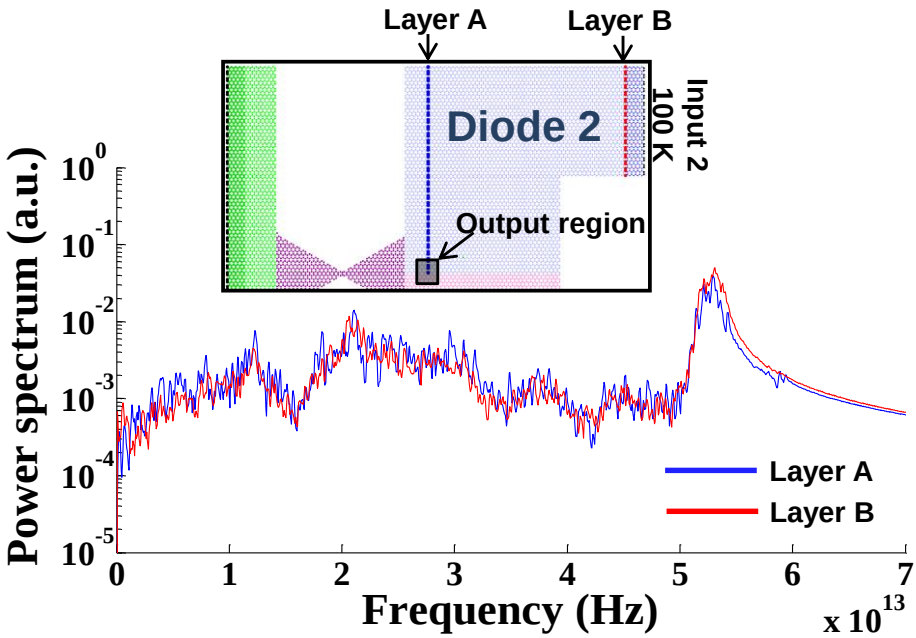


(a)

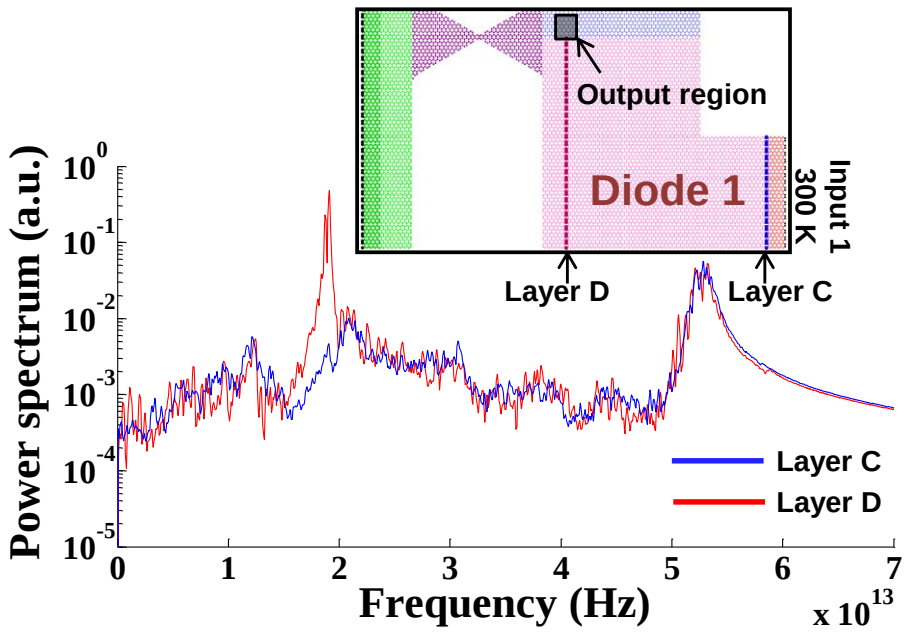


(b)

**Figure 5.4:** (a) The steady state phonon spectrum for atoms in layers A and B in diode 2 is presented. Layer B is immediately next to the heat bath. Layer A lies at the center of the *x* bounds

of the output region, i.e., at $x = 0$. (b) The steady state phonon spectrum for atoms in layer C and D in diode 1 is presented. Layer C is adjacent to the heat bath. Layer D lies at $x = 0$.

Clearly, there is significantly higher spectral overlap between layers A and B as compared to that between layers C and D. The direction of heat transfer in diode 1 is from layer C to layer D while that in diode 2 is from layer A to layer B. Thus, for a GNR diode, the spectral overlap increases when heat transfer occurs from the wider to the narrower terminal, as in diode 1, favoring greater thermal transport in contrast to thermal transport the opposite direction, i.e., from narrower to the wider terminal in diode 2. In asymmetric GNR thermal diodes, this spectrum modification is produced by the asymmetric boundary scattering of phonons at different locations [99]. The higher impedance to phonon transport from layer C to D makes diode 1 to become reverse biased and thereby induces a relatively larger temperature drop of $T_1 - T_o = 145\,\mathrm{K}$ as compared to a smaller drop of $T_o - T_2 = 55\,\mathrm{K}$ across the forward biased diode 2.

### *5.3.5. Role of phonon spectrum in strong nonlinearity of temperature distribution*

It is worth noting that in Fig. 5.2(b), the temperature drop in diode 1 is highly nonlinear in the vicinity of the heat bath. This is attributed to the very localized spectral mismatch in diode 1 that produces impedance to phonon transport. To prove this, we establish a quantitative measure of the spectral mismatch between two spectra $P_1(f)$ and $P_2(f)$ as,

$$S = \frac{\int_0^\infty \sqrt{P_1(f)P_2(f)}\,df}{\sqrt{\left(\int_0^\infty P_1(f)\,df\right)\left(\int_0^\infty P_2(f)\,df\right)}}. \tag{5.4}$$

$S = 1$ and $S = 0$ correspond to the complete spectral overlap and complete spectral mismatch conditions, respectively. We calculate $S$ between layer C and each of the seven other layers

shown in Fig. 5.5(a). A plot of $S$ with respect to the position of those layers along $x$ is presented in Fig. 5.5(b). This exercise helps us understand how the phonon spectrum changes along the direction of heat transfer in diode 1. For layer 1, $S \sim 1$, indicating almost complete overlap with the layer C spectrum. However, for layers 2–4, the overlap with the layer C spectrum, indicated by decreasing $S$, drops significantly over a very small distance but shows little change beyond layer 5. The steep change in the phonon spectrum from layer C to layer 4 causes significant phonon scattering, The bulk of the temperature drop occurs in this region.

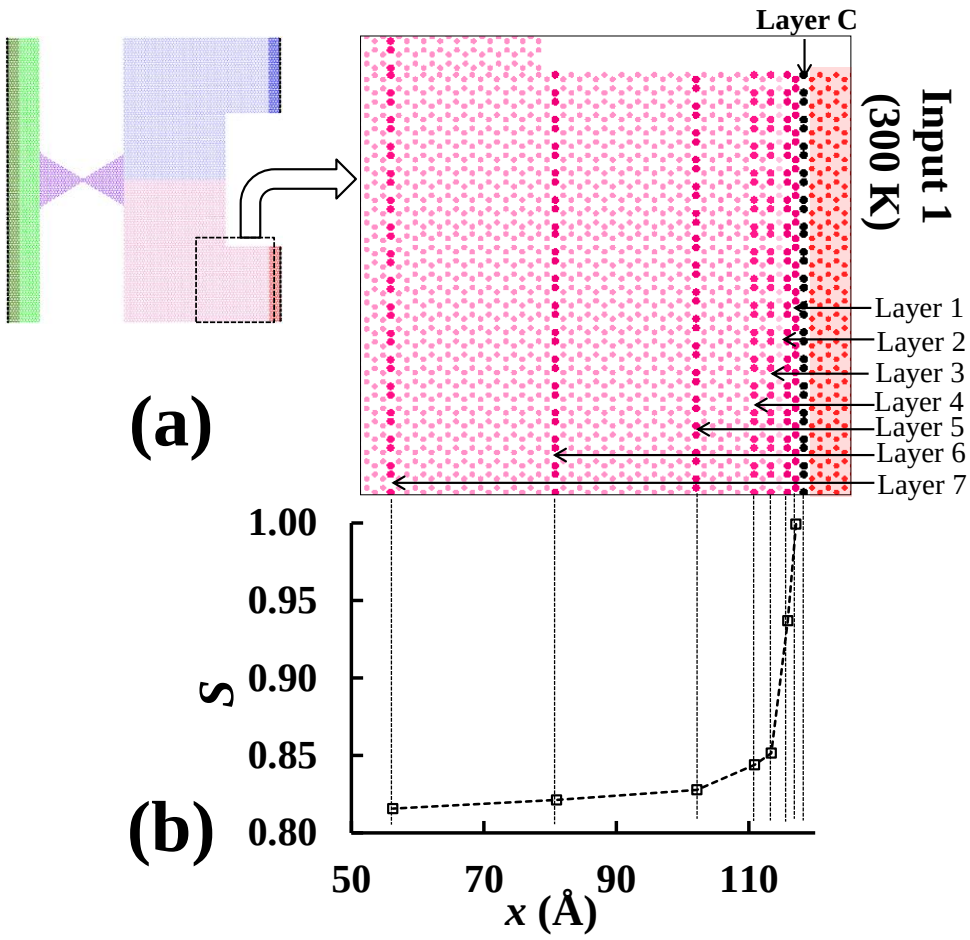


**Figure 5.5:** (a) An expanded image of diode 1 is shown where seven layers of atoms, numbered 1 – 7, are highlighted in deep pink along with the layer C the is immediately next to the heat bath and shown in black. For each of the seven layers, the spectral overlap parameter $S$ is calculated

between that layer and layer C. (b) The resulting values of *S* for each of the seven layers with respect their *x*-position are plotted.

However, after this section the phonon spectrum does not change appreciably. This implies that beyond layer 5 there are high spectral overlaps between layers, i.e., very little phonon scattering occurs beyond layer 5. Hence, the temperature drop is very small in this region. The change in the phonon spectrum is highly non-uniform and also very localized. This leads to localized increase in the impedance to phonon transport and explains the strong non-linearity of the temperature profile close to the heat bath in diode 1.

### *5.3.6. Role of boundary scattering: comparison with continuum length scale behavior*

It is worth asking, if there were no rectification at all from the individual GNR diodes, what would have been the output temperature? At room temperature, graphene has a phonon mean free path (mfp) of ~775 nm [151], which is much larger than the length scale $L$ for the base case AND gate. Consequently, thermal transport is significantly influenced through phonon boundary scattering, which primarily controls thermal rectification in the diodes. The influence of boundary scattering could be eliminated by simulating the AND gate at a length significantly larger than 775 nm. However, such a system would require enormous computational resources. At the larger length scale, phonon transport is diffusive, allowing us to model the heat transfer through the continuum 2-D diffusion equation, which at steady state is,

$$\frac{\partial^2 T}{\partial x^2} + \frac{\partial^2 T}{\partial y^2} = 0 \tag{5.5}$$

The steady state temperature contour obtained by solving Eq. (5.5) for an equivalent continuum system is shown in Fig. 5.6. The continuum system is isometrically scaled up with the ratios of the lengths of different sections held unaltered. The temperature distribution shown in Fig. 5.6 is

independent of the thermal conductivity and length scale $L$, as long as $L \gg$ mfp of phonons, since at this scale, boundary scattering has a weak influence on thermal transport as compared to Umklapp phonon-phonon scattering. The independence of the steady state temperature contours with respect to the thermal conductivity $\kappa$ are apparent because $\kappa$ is absent from Eq. (5.5).

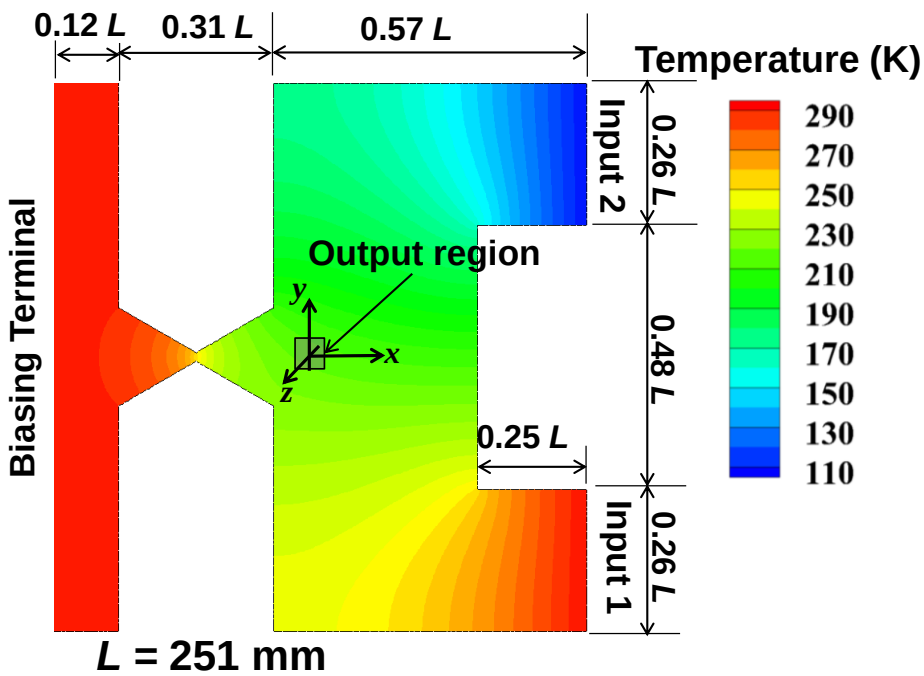


**Figure 5.6:** Steady state temperature contours in a 2D region that is similar in shape to the thermal AND gate in Fig. 5.1(c) but with $L$ = 251 mm is shown. The edges at the input and biasing terminals are subjected to Dirichlet boundary conditions while all other edges are subjected to adiabatic boundary condition.

The spatiotemporal averaged temperature at the output section is 220 K which is significantly higher than the temperature obtained with the smaller graphene AND gate. The corresponding value of $\varepsilon$ is 0.6, which is outside the maximum allowed range $0 \le \varepsilon \le 0.5$ for the output to be designated as 'LOW'. Hence, the continuum system does not behave as an AND gate. This

establishes that thermal rectification is essential in obtaining AND gate behavior, which is achieved at very small length scales due to the strong boundary scattering of phonons.

### *5.3.7. Dependence of gate performance on input temperature ranges*

We now investigate the ranges of operating temperature that lead to the most effective operation of the AND gate, i.e., the smallest possible value of $\tilde{\varepsilon}$. For this, we compare $\tilde{\varepsilon}$ obtained for the 1 - 0 input cases with different 'HIGH' and 'LOW' temperatures. Simulations are run for three different 'HIGH' temperatures of 300 K, 400 K and 500 K. For each such value, five simulations are run with different 'LOW' values such that $\Delta T$ = 'HIGH'–'LOW', varies from 40 K to 200 K. The resulting plot of $\tilde{\varepsilon}$ vs. $\Delta T$ is presented in Fig. 5.7. The base case corresponds to $\Delta T$ = 200 K when 'HIGH' is 300 K. For all three 'HIGH' temperatures, when $\Delta \leq 80$ K the device performance is very poor because $\tilde{\varepsilon}$ is close to 0.5. Increasing $\Delta$ beyond 80 K improves device performance, as indicated by the decrease in $\tilde{\varepsilon}$ when 'HIGH' = 300 K. Very little additional improvement in $\tilde{\varepsilon}$ occurs for the other two cases when 'HIGH' = 400 K or 500 K. This reveals the decreasing efficacy of thermal rectification with increasing temperature.

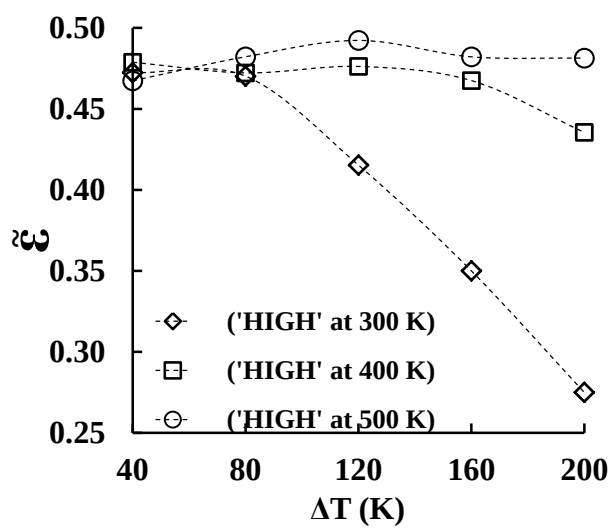


**Figure 5.7:** The variation of $\tilde{\varepsilon}$ for 1 – 0 input with variations in values for 'HIGH' and 'LOW' are shown. Three values of 'HIGH' = 300 K, 400 K and 500 K are used. For each of these, five

simulations are run with five different 'LOW' values such that $\Delta$ varies from 40 to 200 K in steps of 40 K, where $\Delta = \text{'HIGH'} - \text{'LOW'}$. The three sets with different 'HIGH' values' are represented with different symbols.

The rectification mechanism based on phonon boundary scattering that limits thermal conductivity and phonon transport is more apparent at low temperatures. At temperatures higher than 80 K, the effect of Umklapp phonon-phonon scattering on heat transfer starts to become comparable to that of boundary scattering [152]. At room temperature, Umklapp phonon-phonon scattering dominates over boundary scattering [153]. When 'HIGH' = 300 K and 'LOW' = 100 K, most regions of the device are at temperatures significantly lower than 300 K, as is evident from Fig. 5.2, i.e., boundary scattering is still effective. Increasing 'LOW' from 100 K, i.e., decreasing $\Delta$ from 200 K, this effectiveness diminishes, leading to a deterioration in performance. With 'HIGH' = 400 K or 500 K, Umklapp phonon scattering eliminates the influence of boundary scattering and the device performance is even worse.

### *5.3.8. Switching characteristics*

Finally, we characterize the response of the AND gate to a rapidly changing input. In a practical implementation, an AND gate is subjected to continuously changing streams of 1 and 0 states at the two inputs. The pace at which the output can keep abreast of changes in the input is called the switching time, which is an important property of a diode. To examine the thermal switching time, we first obtain a steady state for the base case with the 1 - 0 state and then abruptly change the temperature at the 'LOW' terminal to 'HIGH', i.e., to 300 K, thereby changing to a 1–1 condition. The resulting alteration in the output $\varepsilon$ with respect to time is presented in Fig. 8, where $t = 0$ corresponds to steady state and the input 2 is switched at $t = 80$ ps.

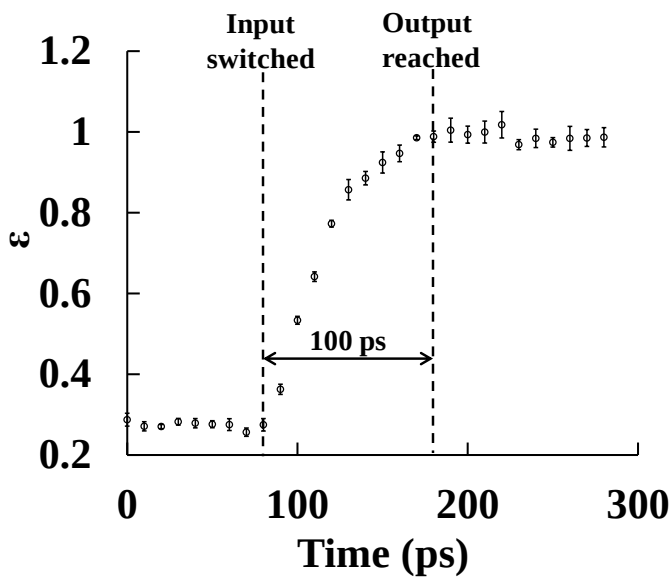


**Figure 5.8:** Switching characteristic of the AND gate is shown**.** At steady state for the base case with 1 - 0, the input 2 is switch to logic 1. The transient evolution of $\varepsilon$ is plotted over time. The error bar representing the error in $\varepsilon$ calculated over the temperature of all atoms in the output region. In this figure, $t = 0$ represents steady state. After 80 ps the input is switched.

The device output $\varepsilon$ responds to this change by attaining a value close to 1 in about 100 ps, which represents the switching time. This time is comparable to that for a fast response electrical diode, such as the Schottky diode which has a switching time between 10 to 100 ps [154]. The fast response of the thermal device can be attributed to the very high phonon speed in grapheme, which is $\sim 2\times10^4$ m s$^{-1}$[155].

### 5.4. Summary

A thermal AND gate is implemented using GNR diodes and represents the first study of such a gate using existing nanomaterials. Employing molecular dynamics simulations, the diode performance is characterized. The output from the diode is presented in the form of a truth table. The range of output temperatures that can be designated as 'HIGH' and 'LOW' are identified. With either inputs at a logic 0 state, the device output parameter $\varepsilon$ is in the range $0 \le \varepsilon \le 0.275$,

which is comparable to that for a typical silicon based electrical diode ($0 \le \varepsilon \le 0.12$). The working mechanism of the thermal AND gate is controlled by the thermal rectification effect in the two diodes. This rectification occurs due to asymmetric phonon boundary scattering, which is significant at the nanoscale when the device length is comparable to the phonon mfp. Thus, such a device loses its efficacy at continuum length scales. The device performs better at temperatures lower than 300 K when boundary scattering dominates over phonon-phonon Umklapp scattering. The switching speed of the AND gate is ~100 ps, which is comparable to that for fast electrical diodes. This is attributed to the fast phonon propagation speed of $2\times10^4$ m $s^{-1}$ in graphene. The results imply there is significant potential to implement GNR diodes in phononic logic circuits and thus perform computations with phonons.

### 5.5. Acknowledgement

This research was supported by a grant from the National Science Foundation (CBET 1246611). We thank the Virginia Tech Department of Engineering Science and Mechanics for the use of its Linux Computing Cluster.

Chapter 6

# Future research

The research in the area of thermal rectification is still in its infancy. A majority of the work in this area is theoretical or simulations based. Experiments need to be performed which can validate simulation results and test implementation of phononic devices such as GNR AND gate, thermal transistor, etc. A primary difficulty in performing experiments is the small size of such systems, often at the nanometer range. Much of the interesting thermal behavior is apparent only at that length scale due to phonon boundary scattering. Thus scaled up prototypes lose the thermal behaviors manifested at a smaller length scale. Another practical concern is the range of temperatures far below or above room temperature required in these studies. New experimental schemes need to be developed for performing those challenging thermal transport studies.

Although properties of different thermal diode implementations are well characterized by now, not enough investigations have been reported on how these diodes behave collectively when placed in a phononic circuit. The thermal AND gate proposed in chapter 5 is just a first step in that direction. Detailed investigations of other device like thermal OR gate, memory, and transistor need to be performed. In thermal memory studies, the major concern needs to be addressed is the problem of slow information loss due to heat loss over long periods of time.

In chapters 2 and 3 we explored different mechanisms to reduce phonon thermal conductivity in polymers for thermoelectric energy applications. With reduction of thermal conductivity, the thermoelectric figure of merit goes up, given that the electrical conductivity remains the same or does not increase appreciably. To test this, the role of phonon transport on electrical transport, i.e., electron-phonon interactions also needs to be modeled. The standard molecular dynamics simulation technique ignores electronic interactions. It will be worth investigating how mechanical deformation can alter electronic properties of the system and how does that change the thermoelectric figure of merit. Techniques like CPMD (Car–Parrinello molecular dynamics), quantum-classical tight binding schemes can include electronic interactions and can provide estimates of electronic conductivity of such systems. However, the main problem with CPMD or similar first principle simulation techniques is that the computational time required to model a system large enough to be physically meaningful is enormous. Thus, the challenge is to develop mesoscale numerical simulation tools which can consider electron-phonon interactions without explicitly modeling individual electrons. Such a coarse graining model can be applied to a variety of mass and energy transport problems such as thermoelectric energy storage and conversion, transport of ions in batteries for large scale electronic storage etc.

# Appendix A

# Description of the force field employed for the molecular dynamics simulations in chapter 2

We use a class II force field,[156] Polymer Consistent Force Field (PCFF), in which the total potential energy of the polymer

$$E = E_{bond} + E_{angle} + E_{dihedral} + E_{out-of-plane} + E_{cross-coupling-term} + E_{non-bonded}, \quad \text{(A1)}$$

$$E_{bond} = \sum_{l} c_1 (l - l_0)^2 + c_2 (l - l_0)^3 + c_3 (l - l_0)^4, \quad \text{(A2)}$$

$$E_{angle} = \sum_{\theta} d_1 (\theta - \theta_0)^2 + d_2 (\theta - \theta_0)^3 + d_3 (\theta - \theta_0)^4, \quad \text{(A3)}$$

$$E_{dihedral} = \sum_{\phi} k_1 (1 - \cos(\phi)) + k_2 (1 - \cos(2\phi)) + k_3 (1 - \cos(3\phi)), \quad \text{(A4)}$$

$$E_{out-of-plane} = \sum_{\chi} K \chi^2, \quad \text{(A5)}$$

$$E_{cross-coupling-term} = E_{bond-bond} + E_{bond-angle} + E_{bond-torsion} + E_{angle-angle} + E_{angle-angle-torsion} + E_{angle-torsion}, \quad \text{(A6)}$$

$$E_{bond-bond} = \sum_{l,l'} h (l - l_0)(l' - l_0'), \quad \text{(A7)}$$

$$E_{bond-angle} = \sum_{l,\theta} h' (l - l_0)(\theta - \theta_0), \quad \text{(A8)}$$

$$E_{bond-torsion} = \sum_{l,\phi} (l - l_0)(g_1 \cos\phi + g_2 \cos 2\phi + g_3 \cos 3\phi), \quad \text{(A9)}$$

$$E_{angle-torsion} = \sum_{\theta,\phi} (\theta - \theta_0)(g_1' \cos\phi + g_2' \cos 2\phi + g_3' \cos 3\phi), \quad \text{(A10)}$$

$$E_{angle-angle-torsion} = \sum_{\theta,\theta',\phi} k_{aa} (\theta - \theta_0)(\theta' - \theta_0') \cos\phi, \quad \text{(A11)}$$

$$E_{angle-angle} = \sum_{l,\theta} s(\theta - \theta_0)(\theta' - \theta_0'), \tag{A12}$$

$$E_{non-bonded} = E_{Coulomb} + E_{vdw} \ , \tag{A13}$$

$$E_{Coulomb} = \sum_{i,j} \frac{q_i q_j}{r_{ij}} \ , \tag{A14}$$

$$E_{vdw} = \sum_{i,j} \varepsilon_{ij} \left[ 2\left(\frac{\sigma_{ij}}{r_{ij}}\right)^9 - 3\left(\frac{\sigma_{ij}}{r_{ij}}\right)^6 \right]. \tag{A15}$$

Here, $E_{bond}$ is the energy associated with change in bond length $l$ during the simulation from equilibrium bond length $l_0$, and $c_1$, $c_2$, and $c_3$ denote the force constants associated with the bond stretching. The 3rd and 4th order terms in Eq. (A1) are considered along with the 2nd order harmonic term in order to account for the anharmonic interactions in these polymers. $E_{angle}$ denotes the energy associated with change in bond angle $\theta$ from the equilibrium bond angle $\theta_0$ with $d_1$, $d_2$, and $d_3$ as associated force constants. The torsional potential energy $E_{dihedral}$ is characterized by the change in the dihedral angle $\varphi$ from the equilibrium dihedral angles $\varphi_0$ ($\varphi_0$ =0 for the present case) with $k_1$, $k_2$, and $k_3$ as associated force constants. The out of plane deformation is characterized by the out of plane angle $\chi$ and the associated constant $K$ as shown in Eq. (A5). The cross coupling terms account for the effect of one deformation on the other, e.g., the influence of bond stretching on angle bending. These are calculated from Eqs. (A7)-(A12). In these relations $l_0, \theta_0, l_0', \theta_0', g_1, g_2, g_3, g_1', g_2', g_3', s, h, h', k_{aa}$ are all constants. The nonbonded interactions are given by $E_{non\text{-}bonded}$ which is sum of contributions from Coulombic ($E_{Coulomb}$) and *van der Waals* ($E_{vdw}$) interactions. For Columbic interactions, as shown in Eq. (14), $q_i$ and $q_j$ represents the partial charges of atoms separated by an interatomic distance of $r_{ij}$. For calculating long range Coulombic interactions, a particle-particle particle-mesh (pppm)[157] algorithm is used. The *van der Waals* interactions are calculated in the form of a 6-9 Lennard-

Jones (LJ) potential, as shown in Eq. (A15). Here, the size parameter $\sigma_{ij}$ is the radial distance $r_{ij}$ between the centers of atoms $i$ and $j$ at which the potential is zero and $\varepsilon_{ij}$ denotes the depth of the potential well. $\sigma_{ij}$ for the atom pair $i$, $j$ is calculated from the individual LJ size parameter of individual atoms $\sigma_i$ and $\sigma_j$ using a sixth power rule as shown in Eq. (A16), whereas the energy parameter $\varepsilon_{ij}$ for the atom pair $i$, $j$ is given by the formula shown in Eq. (A17), i.e.,

$$\sigma_{ij} = \left[\frac{1}{2}\left(\sigma_i^{\,6} + \sigma_j^{\,6}\right)\right]^{\frac{1}{6}}, \text{ and} \tag{A16}$$

$$\varepsilon_{ij} = 2\sqrt{\varepsilon_i \varepsilon_j}\,\frac{\sigma_i^{\,3}\sigma_j^{\,3}}{\sigma_i^{\,6} + \sigma_i^{\,6}}\,. \tag{A17}$$

To save computational time, both the *van der Waals* and Coulombic interactions are truncated after a cutoff distance $r_c$ , *i.e.*, the potential is set to zero when the interatomic distance is larger than $r_c$. For all simulations, a cutoff distance of 10 Å is used for both the *van der Waals* and the Coulombic interactions.

# Appendix B

## Simulation details and force field parameters used in chapter 2.

### B.1. Energy minimization

We employ the conjugate gradient technique for energy minimization. The resulting convergence of the total energy with respect to the number of iterations is shown in Fig. B1 for representative minimization simulations conducted for a PANI and a PA system. All systems are thermodynamically initialized (i.e., the constituent atoms in that system are assigned initial velocities corresponding to a specified temperature) only after minimization. Hence, the global kinetic energy of the system is zero during the minimization process so that the total system energy is essentially the potential energy of the system. Figure B1 shows that the change in this total energy from timestep 999 to 1000 is 1.21 % for PANI and 0.04 % for PA.

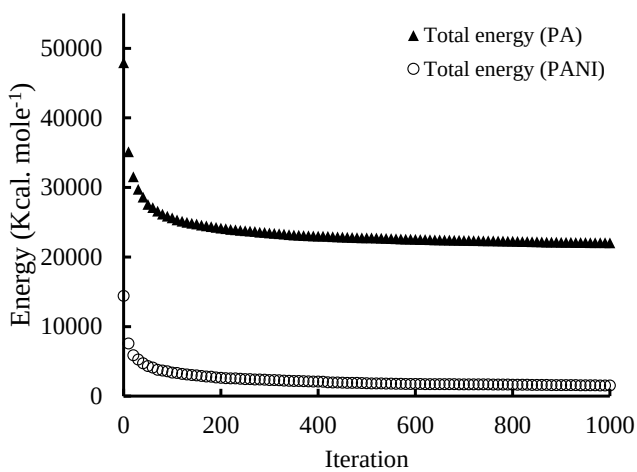


**Figure B.1:** The convergence of the system energy to a minimum during representative minimization simulations for a PANI and a PA system.

## B.2. Details of NEMD simulation

The thermal conductivity is calculated using reverse nonequilibrium molecular dynamics (NEMD). We use the algorithm proposed by Müller-Plathe described in Ref. [23] of the revised manuscript. The standard NEMD method applies thermostats that maintain two different specified temperatures in two regions in the material, i.e., the method applies a known temperature gradient. The heat flux is thereafter determined as the system responds to this condition. On the contrary, with reverse NEMD, a known heat flux is established in the system. As a result, a temperature gradient between the hot and cold regions emerges as the response of the system rather than a prescribed condition. Subsequently, the empirical Fourier's heat conduction law is applied to calculate the thermal conductivity.

The entire domain is divided into 100 layers along the direction of heat transfer (which is along the *x*-axis in our case). When, after equilibration, the temperature of the entire domain becomes uniform at 300K, after every 300 timesteps, the atom with highest kinetic energy in the left boundary layer and the atom with least kinetic energy in the middle layer are selected and their kinetic energies are exchanged by rescaling their velocities. This increases the kinetic energy of the middle layer. A temperature difference is thus established across the domain that facilitates energy transfer from the hot middle layer to the colder boundary layers. A steady state temperature profile is reached when the energy transport rate due to this kinetic energy exchange from the cold to the hot layer is balanced by the heat flux in the reverse direction. Thus, the middle layer behaves as a heat source and the two end layers as sinks. This produces a symmetric temperature profile across the length of the domain over time as shown in Fig. 2.1.

The system is simulated for 5 ns under an NVT ensemble at 300 K. During the final 1 ns, the spatial temperature profile along the *x*-wise direction is determined at 0.1 ns intervals. The

temperatures of the two boundary layers and of the middle layer are shown in Fig. B2. These temperatures correspond to the temperature profile of Fig. 2.1. From Fig. B.2, we note that the time-averaged temperature in the middle is 330.25 K while the corresponding values for the left and right boundaries are 271.53 K and 269.13 K, respectively. The small deviations in temperature (with maximum magnitudes of ±1.3%) from the time averaged value in Fig. B.2 indicate that steady state has been reached.

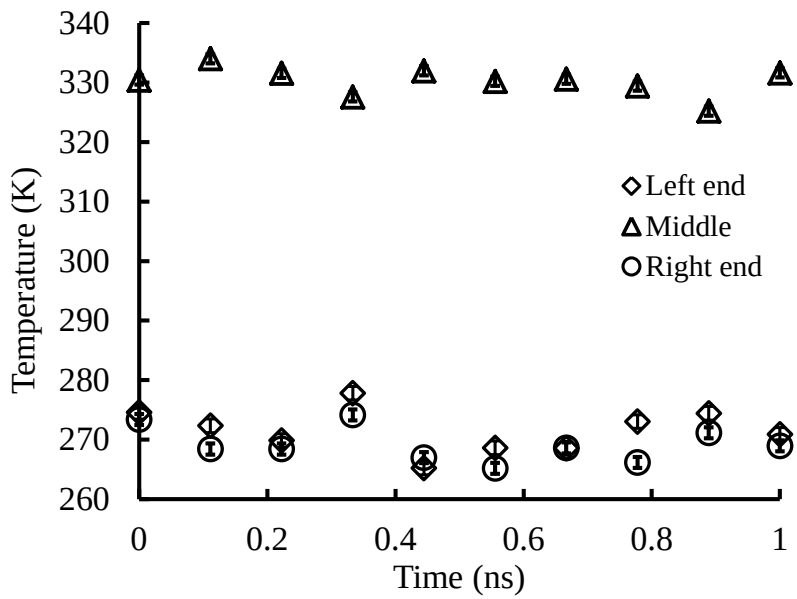


**Figure B.2:** The temperatures of the boundary layers and in the middle layer along *x*-wise direction of the domain are plotted for last 1 ns of NEMD simulation at 0.1 ns intervals. The error bars represent the standard error in temperatures obtained from ten samples collected during this period.

The temperature gradient $\partial T / \partial x$ in each half of the domain along the *x*-wise direction is calculated and averaged for each of the ten temperature profiles obtained over the final 1 ns. Finally, the thermal conductivity is obtained from Fourier's law, i.e.,

$$\kappa = -j_x / \left(\partial T / \partial x\right)_{av}, \tag{B1}$$

where $\kappa$ denotes the thermal conductivity, $j_x = J_x/2$ is the applied heat flux from the source to either of the sinks, and $\left(\partial T / \partial x\right)_{av}$ the average temperature gradient considering both the left and right halves of the material that is further averaged over the ten temperature profiles obtained during the final 1 ns. Note that $J_x$ is the total energy exchanged across the hot and cold layers over the entire simulation length per unit cross sectional area (which is the *yz* plane) of the domain.

The parameters required to calculate the total potential energy according to the formulation described in the Appendix of the main manuscript are provided in Tables B1-B11 (for PANI) and Tables B12-B22 (for PA). The constant *s* in Eq. (A12) is zero for both PA and PANI. In each table the interaction parameters are provided for only those types that have a non-zero contribution towards the energy.

**PCFF parameters**[70, 156] **for PANI**

Table B.1: The different atom types present in a PANI molecule.

| Atom type | Description |
|---|---|
| cp | Carbon atom in $sp^2$ hybridized state |
| hc | Hydrogen atom bonded to carbon atoms |
| hn | Hydrogen atom bonded to nitrogen atoms |
| na | Nitrogen in $sp^3$ hybridized state (amines) |
| nb | Nitrogen in $sp^2$ hybridized state (amines) |

Table B.2: Bonded interaction parameters for different bond types in PANI (Eq. (A2)).

| Bond type | Equilibrium bond length $l_0$ (Å) | $c_1$ (Kcal mole$^{-1}$ Å$^{-2}$) | $c_2$ (Kcal mole$^{-1}$ Å$^{-3}$) | $c_3$ (Kcal mole$^{-1}$ Å$^{-4}$) |
|---|---|---|---|---|
| na - cp | 1.412 | 257.800 | 0.000 | 0.000 |
| na - hn | 1.006 | 466.700 | -1074.000 | 1251.000 |
| cp - cp | 1.417 | 470.800 | -627.600 | 1328.000 |
| cp - hc | 1.098 | 372.800 | -803.500 | 894.300 |
| cp - nb | 1.391 | 447.000 | -784.500 | 886.200 |

Table B.3: Angle interaction parameters for different angle types in PANI (Eq. (A3)).

| Angle type | Equilibrium angle $\theta_0$ (radian) | $d_1$ (Kcal mole$^{-1}$ radian$^{-2}$) | $d_2$ (Kcal mole$^{-1}$ radian$^{-3}$) | $d_3$ (Kcal mole$^{-1}$ radian$^{-4}$) |
|---|---|---|---|---|
| cp-na-hn | 1.920 | 41.600 | 0.000 | 0.000 |
| hn-na-hn | 1.869 | 45.250 | -7.556 | -9.512 |
| na-cp-cp | 2.094 | 102.000 | 0.000 | 0.000 |
| cp-cp-cp | 2.075 | 61.020 | -34.990 | 0.000 |
| cp-cp-hc | 2.058 | 35.160 | -12.470 | 0.000 |
| cp-na-cp | 1.902 | 80.000 | 0.000 | 0.000 |
| cp-cp-nb | 2.120 | 61.060 | -21.620 | 0.000 |
| cp-nb-cp | 2.094 | 50.000 | 0.000 | 0.000 |

Table B.4: Dihedral interaction parameters for different dihedral types in PANI (Eq. (A4)).

| Dihedral type | $k_1$ (Kcal mole$^{-1}$) | $k_2$ (Kcal mole$^{-1}$) | $k_3$ (Kcal mole$^{-1}$) |
|---|---|---|---|
| hn - na - cp - cp | 0.000 | 2.250 | 0.000 |
| na - cp - cp - cp | 0.000 | 3.000 | 0.000 |
| na - cp - cp - hc | 0.000 | 3.000 | 0.000 |
| cp - cp - cp - cp | 8.367 | 1.193 | 0.000 |
| cp - cp - cp - hc | 0.000 | 3.966 | 0.000 |
| hc - cp - cp - hc | 0.000 | 1.877 | 0.000 |
| cp - cp - na - cp | 0.000 | 2.250 | 0.000 |
| cp - cp - cp - nb | 0.000 | 5.383 | 0.000 |
| hc - cp - cp - nb | 0.000 | 1.333 | 0.000 |
| cp - cp - nb - cp | 0.000 | 2.250 | 0.000 |

Table B.5: Out-of-plane (improper) interaction parameters in PANI (Eq. (A5)).

| Improper type | $K$ (Kcal mole$^{-1}$ radian$^{-2}$) |
|---|---|
| cp - na - cp - cp | 10.000 |
| cp - cp - cp - hc | 7.601 |
| cp - cp - cp - nb | 10.790 |

Table B.6: Bond-bond cross-term parameters for PANI (Eq. (A7)).

| Bond-bond type | $h$ (Kcal mole$^{-1}$ Å$^{-2}$) |
|---|---|
| hn-na-hn | -1.875 |
| cp-cp-cp | 68.286 |
| cp-cp-hc | 1.080 |
| cp-cp-nb | 46.951 |

Table B.7**:** Bond-angle cross-term parameters for PANI (Eq. (A8)).

| Bond/angle type | $h'$ (Kcal mole$^{-1}$ Å$^{-1}$radian$^{-1}$) |
|---|---|
| hn-na/hn-na-hn | 28.032 |
| cp-cp/cp-cp-cp | 28.871 |
| cp-cp/cp-cp-hc | 20.003 |
| cp-hc/cp-cp-hc | 24.218 |
| cp-cp/cp-cp-nb | 39.404 |
| cp-nb/cp-cp-nb | 73.655 |

Table B.8: Bond-torsion cross-term parameters for PANI (Eq. (A9)).

| Bond/torsion type | $g_1$ (Kcal mole$^{-1}$ Å$^{-1}$) | $g_2$ (Kcal mole$^{-1}$ Å$^{-1}$) | $g_3$ (Kcal mole$^{-1}$ Å$^{-1}$) |
|---|---|---|---|
| cp-cp/cp-cp-cp-cp | -0.119 | 6.320 | 0.000 |
| cp-cp/cp-cp-cp-hc | 0.000 | -6.896 | 0.000 |
| cp-hc/cp-cp-cp-hc | 0.000 | -0.467 | 0.000 |
| hc-cp/hc-cp-cp-hc | 0.000 | -0.689 | 0.000 |
| cp-cp/cp-cp-cp-nb | 0.000 | -6.540 | 0.000 |
| cp-nb/cp-cp-cp-nb | 0.000 | -7.348 | 0.000 |
| hc-cp/hc-cp-cp-nb | 0.000 | -2.648 | 0.000 |
| cp-nb/hc-cp-cp-nb | 0.000 | -1.640 | 0.000 |
| cp-cp/cp-cp-cp-cp (middle) | 27.599 | -2.312 | 0.000 |
| cp-cp/cp-cp-cp-hc (middle) | 0.000 | -1.152 | 0.000 |
| cp-cp/hc-cp-cp-hc (middle) | 0.000 | 4.823 | 0.000 |
| cp-cp/cp-cp-cp-nb (middle) | 0.000 | -0.569 | 0.000 |
| cp-cp/hc-cp-cp-nb (middle) | 0.000 | 2.288 | 0.000 |

Table B.9: Angle-torsion cross-term parameters for PANI (Eq. (A10)).

| Angle/torsion type | $g_1'$ (Kcal mole$^{-1}$ radian$^{-1}$) | $g_2'$ (Kcal mole$^{-1}$ radian$^{-1}$) | $g_3'$ (Kcal mole$^{-1}$ radian$^{-1}$) |
|---|---|---|---|
| cp-cp-cp/cp-cp-cp-cp | 1.977 | 1.024 | 0.000 |
| cp-cp-cp/cp-cp-cp-hc | 0.000 | 2.501 | 0.000 |
| cp-cp-hc/cp-cp-cp-hc | 0.000 | 2.715 | 0.000 |
| hc-cp-cp/hc-cp-cp-hc | 0.000 | 2.450 | 0.000 |
| cp-cp-cp/cp-cp-cp-nb | 0.000 | 9.090 | 0.000 |
| cp-cp-nb/cp-cp-cp-nb | 0.000 | -6.088 | 0.000 |
| hc-cp-cp/hc-cp-cp-nb | 0.000 | 2.981 | 0.000 |
| cp-cp-nb/hc-cp-cp-nb | 0.000 | 0.279 | 0.000 |

Table B.10: Angle-angle-torsion cross-term parameters for PANI (Eq. (A11)).

| Angle/angle/torsion type | $k_{aa}$ (Kcal mole$^{-1}$ radian$^{-2}$) |
|---|---|
| cp-cp-cp-hc | -4.814 |
| hc-cp-cp-hc | 0.360 |

Table B.11: Nonbonded interaction parameters for PANI.

| Atom Type | Size parameter $\sigma$ (Å) | Depth of potential well $\varepsilon$ (Kcal mole$^{-1}$) | Partial charge *q[158]* (electron units) |
|---|---|---|---|
| cp (cp-na / cp-nb) | 4.010 | 0.064 | 0.083 |
| cp (cp-hc) | 4.010 | 0.064 | -0.127 |
| hc | 2.995 | 0.020 | 0.127 |
| hn | 1.098 | 0.013 | 0.359 |
| na | 4.070 | 0.065 | -0.415 |
| nb | 4.070 | 0.065 | -0.414 |

**PCFF parameters** [70, 156] **for PA**

Table B.12: The different atom types present In a PA molecule.

| Atom type | Description |
|---|---|
| cp | Carbon atom in $sp^2$ hybridized state |
| hc | Hydrogen atom bonded to carbon atoms |

Table B.13: Bonded interaction parameters for different bond types in PA (Eq. (A2)).

| Bond type | Equilibrium bond length $l_0$ (Å) | $c_1$ (Kcal mole$^{-1}$ Å$^{-2}$) | $c_2$ (Kcal mole$^{-1}$ Å$^{-3}$) | $c_3$ (Kcal mole$^{-1}$ Å$^{-4}$) |
|---|---|---|---|---|
| cp - cp | 1.417 | 470.836 | -627.618 | 1327.635 |
| cp - hc | 1.098 | 372.825 | -803.453 | 894.317 |

Table B.14: Angle interaction parameters for different angle types in PA (Eq. (A3)).

| Angle type | Equilibrium angle $\theta_0$ (radian) | $d_1$ (Kcal mole$^{-1}$ radian$^{-2}$) | $d_2$ (Kcal mole$^{-1}$ radian$^{-3}$) | $d_3$ (Kcal mole$^{-1}$ radian$^{-4}$) |
|---|---|---|---|---|
| cp-cp-hc | 2.058 | 35.156 | -12.468 | 0.000 |
| cp-cp-cp | 2.075 | 61.023 | -34.993 | 0.000 |
| hc-cp-hc | 2.094 | 37.000 | 0.000 | 0.000 |

Table B.15: Dihedral interaction parameters for different dihedral types in PA (Eq. (A4)).

| Dihedral type | $k_1$ (Kcal mole$^{-1}$) | $k_2$ (Kcal mole$^{-1}$) | $k_3$ (Kcal mole$^{-1}$) |
|---|---|---|---|
| hc - cp - cp - cp | 0.000 | 3.966 | 0.000 |
| hc - cp - cp - hc | 0.000 | 1.877 | 0.000 |
| cp - cp - cp - cp | 8.367 | 1.193 | 0.000 |

Table B.16: Out-of-plane (improper) interaction parameters in PA (Eq. (A5)).

| Improper type | $K$ (Kcal mole$^{-1}$ radian$^{-2}$) |
|---|---|
| cp - cp - cp - hc | 7.601 |
| cp - cp - hc - hc | 10.000 |

Table B.17: Bond-bond cross-term parameters for PA (Eq. (A7)).

| Bond-bond type | $h$ (Kcal mole$^{-1}$ Å$^{-2}$) |
|---|---|
| cp-cp-hc | 1.080 |
| cp-cp-cp | 68.286 |

Table B.18: Bond-angle cross-term parameters for PA (Eq. (A8)).

| Bond/angle type | $h'$ (Kcal mole$^{-1}$ Å$^{-1}$radian$^{-1}$) |
|---|---|
| cp-cp/cp-cp-hc | 20.003 |
| cp-hc/cp-cp-hc | 24.218 |
| cp-cp/cp-cp-cp | 28.871 |

Table B.19: Bond-torsion cross-term parameters for PA (Eq. (A9)).

| Bond/torsion type | $g_1$ (Kcal mole$^{-1}$ Å$^{-1}$) | $g_2$ (Kcal mole$^{-1}$ Å$^{-1}$) | $g_3$ (Kcal mole$^{-1}$ Å$^{-1}$) |
|---|---|---|---|
| hc-cp/hc-cp-cp-cp | 0.000 | -0.467 | 0.000 |
| cp-cp/hc-cp-cp-cp | 0.000 | -6.896 | 0.000 |
| hc-cp/hc-cp-cp-hc | 0.000 | -0.689 | 0.000 |
| cp-cp/cp-cp-cp-cp | -0.119 | 6.320 | 0.000 |
| cp-cp/hc-cp-cp-cp (middle) | 0.000 | -1.152 | 0.000 |
| cp-cp/hc-cp-cp-hc (middle) | 0.000 | 4.823 | 0.000 |
| cp-cp/cp-cp-cp-cp (middle) | 27.599 | -2.312 | 0.000 |

Table B.20: Angle-torsion cross-term parameters for PA (Eq. (A10)).

| Angle/torsion type | $g_1'$ (Kcal mole$^{-1}$ radian$^{-1}$) | $g_2'$ (Kcal mole$^{-1}$ radian$^{-1}$) | $g_3'$ (Kcal mole$^{-1}$ radian$^{-1}$) |
|---|---|---|---|
| hc-cp-cp/hc-cp-cp-cp | 0.000 | 2.715 | 0.000 |
| cp-cp-cp/hc-cp-cp-cp | 0.000 | 2.501 | 0.000 |
| hc-cp-cp/hc-cp-cp-hc | 0.000 | 2.450 | 0.000 |
| cp-cp-cp/cp-cp-cp-cp | 1.977 | 1.024 | 0.000 |

Table B.21: Angle-angle-torsion cross-term parameters for PA (Eq. (A11)).

| Angle/angle-torsion type | $k_{aa}$ (Kcal mole$^{-1}$ radian$^{-2}$) |
|---|---|
| hc-cp-cp-cp | -4.814 |
| hc-cp-cp-hc | 0.360 |

Table B.22: Nonbonded interaction parameters for PA.

| Atom Type | Size parameter $\sigma$ (Å) | Depth of potential well $\varepsilon$ (Kcal mole$^{-1}$) | Partial charge *q[159]* (electron units) |
|---|---|---|---|
| cp (bonded to 1 hc) | 4.010 | 0.064 | -0.010 |
| cp (bonded to 2 hc) | 4.010 | 0.064 | -0.200 |
| Hc | 2.995 | 0.020 | 0.100 |

# Appendix C

# Simulation details of chapter 3

### C.1. Description of the simulated structures

We consider five geometrical configurations for this investigation containing polyaniline (PANI) and polyacetylene (PA) in the same 1:1 ratio with 64 chains of each polymer. For both PANI and PA, each chain contains 24 carbon atoms in their backbone. Table C1 contains a schematic of the cross section (in the *y-z* plane) for each configuration with dimensions. Blue represents PANI and white corresponds to PA. All structures are constructed using Xenoview.[70]

**Table C.1**: Geometric details of simulated structures in chapter 4

| Configuration | Cross-section in *yz* plane | Length along *x* (heat transfer) direction $\Delta X$ (Å) | Volume(Å$^3$) |
|---|---|---|---|
| 1. | 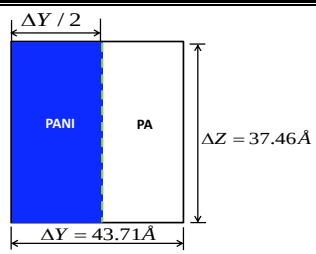 | 44.75 | 73272 |
| 2. | 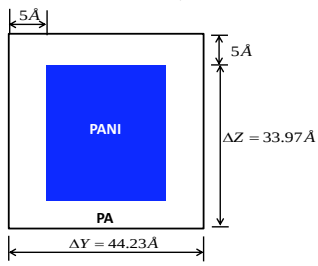 | 44.83 | 74527 |
| 3. | 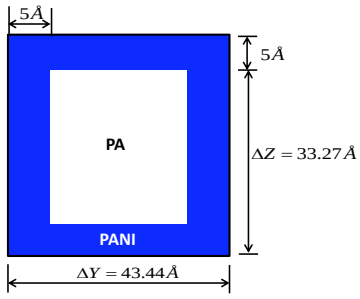 | 44.28 | 76322 |
| 4. | 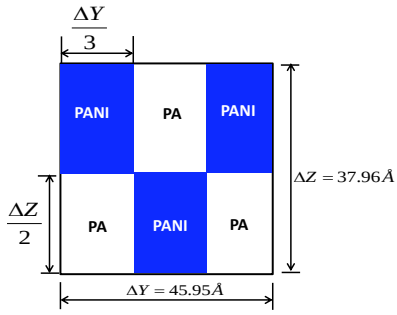 | 41.95 | 73171 |
| 5. | 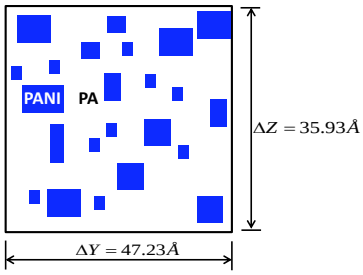 | 43.12 | 73173 |

## C.2. Interfacial area

The interfacial area $S$ is the area of the contact surfaces across which the polymers interact. From the $y$-$z$ plane cross section the length of the interface is calculated, which is then multiplied by the length of the configuration along $x$-wise direction ($\Delta X$) to obtain the total interfacial area. If the interface between PANI and PA is smooth, as shown in Fig. C1(a), its length $\Delta Z$ can be marked by the dotted line. Thus, the total interfacial length for configuration 1 is $2\Delta Z$ accounting for the periodic boundary conditions, i.e., $S = 2\Delta Z \Delta X$ .

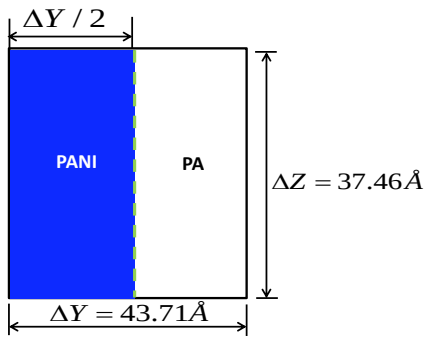


**Figure C.1:** The schematic for calculation of interfacial area for configuration 1.

## C.3. Modification of interfacial area calculation for distorted interface.

Due to the movement of the PANI and PA atoms during thermal equilibration, the interface becomes distorted so that it is no longer a regular straight line, as illustrated in Fig. C1. Therefore, a more accurate measure of $S$ is obtained using an image analysis code.[160] Figure C2 contains an actual image for configuration 1 following thermal equilibration at 300 K. The interface is identified in the figure and its length is measured by the code after proper calibration.

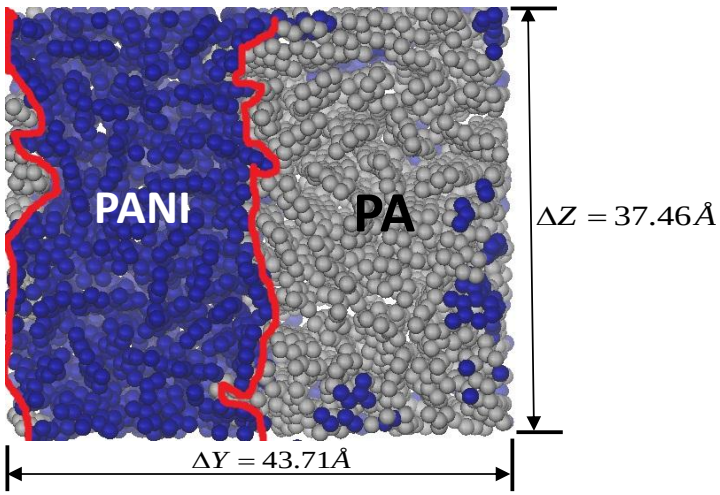


**Figure C.2:** Image of the interface obtained from the simulation of configuration 1 after equilibration at 300 K.

## C.4. Calculation of interfacial area for random distribution (configuration 5) of polymer chains

For configuration 5, the PANI and PA molecules are distributed randomly throughout the cross-section. No well-defined interfaces can be identified through the cross sectional view. This makes the process of outlining the interface and calculating its total length both tedious and inaccurate. To circumvent this problem, the image processing functions in MATLAB (version R2012a 7.14.0.739) are used. Figure C3(a) shows the cross-section of configuration 5 from a simulation image after equilibration at 300 K. The corresponding grayscale binary image is presented in Fig. C3(b). Using the Prewitt edge detection algorithm in MATLAB,[161] the interface is detected as illustrated in Fig S3(c). The total interface length is obtained by counting the number of white pixels in Fig. C3(c) and comparing it with the magnitude of the image dimensions in pixels. Unlike the image analysis approach described in Fig. C2, this approach involves tedious image pre-processing for MATLAB to produce meaningful results. So the image analysis code[160] is used for configurations 1 to 4 for convenience.


(a) (b) (c)

**Figure C.3:** Cross section (*y*-*z* plane) view of configuration 5 with a random distribution of PANI and PA a) A simulation image obtained after equilibration at 300 K. b) The corresponding grayscale binary image in MATLAB c) Detected edges from Fig. C3(b) using the Prewitt edge detection algorithm in MATLAB,[161] represented by white lines.

## C.5. Energy minimization

Energy minimization for all configurations is performed using the conjugate gradient technique. The convergence of energy with respect to subsequent iterations for a representative simulation for configuration 1 is shown in Fig. C4. This convergence is similar to that obtained for all other configurations. Since we perform velocity initialization (i.e., assign initial velocities corresponding to the desired temperature to individual atoms in the configuration) only after minimization, the kinetic energy is zero. Hence, the energy plotted in Fig. C4 is essentially the potential energy of the configuration. The minimization process runs until it satisfies the convergence criterion $\left|(E_n - E_{n-1}) / E_{n-1}\right| \leq 10^{-6}$, where, $E_n$ and $E_{n-1}$ are the energies at the $n$ and $n-1$ iterations. For configuration 1 being discussed, convergence occurred after 913 iterations.

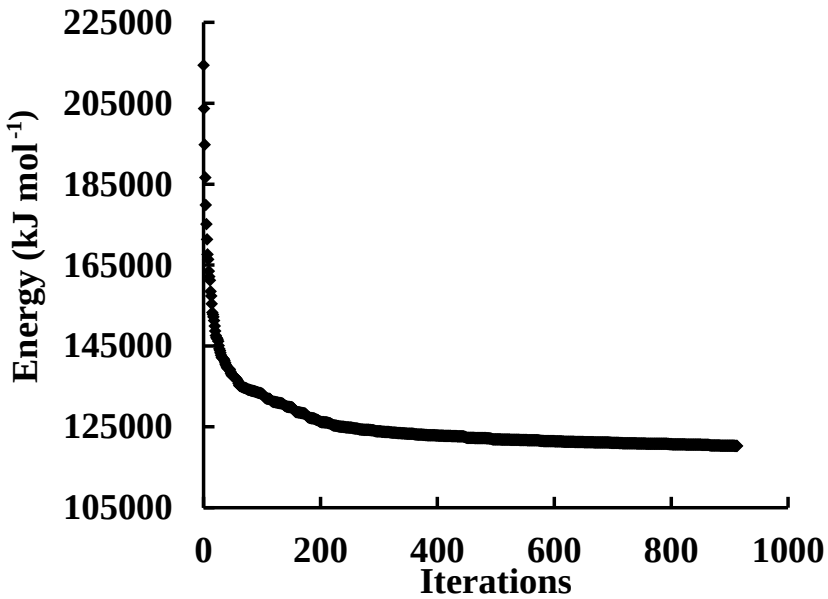


**Figure C.4:** The convergence of the energy to a minimum during a representative energy minimization simulation for configuration 1.

## C.6. Details of equilibration

After energy minimization, each configuration is initialized at the simulation temperature (150, 200, 250, 300, 350 and 400 K for the different cases) followed by a two-step process of annealing and tempering, and a three-stage equilibration process under NPT-NVT-NVE ensembles, each for 0.2 nanoseconds as detailed in the main manuscript. To check if a configuration is properly equilibrated, the temperature during the final (NVE) stage is tracked over time. For the first two stages (NPT and NVT), the temperature is held constant. Proper equilibration ensures that temperature also remains constant during the following NVE stage. Figure C5 shows the temperature of configuration 1 during the 0.2 nanoseconds long NVE stage after the NPT and NVT stage at 300 K. The temperature fluctuates around a time-averaged value of 299 K with small deviations (that have a maximum magnitude of ±0.76 % from the time

averaged value). This indicates that a steady state has been reached and a properly equilibrated structure has been obtained.

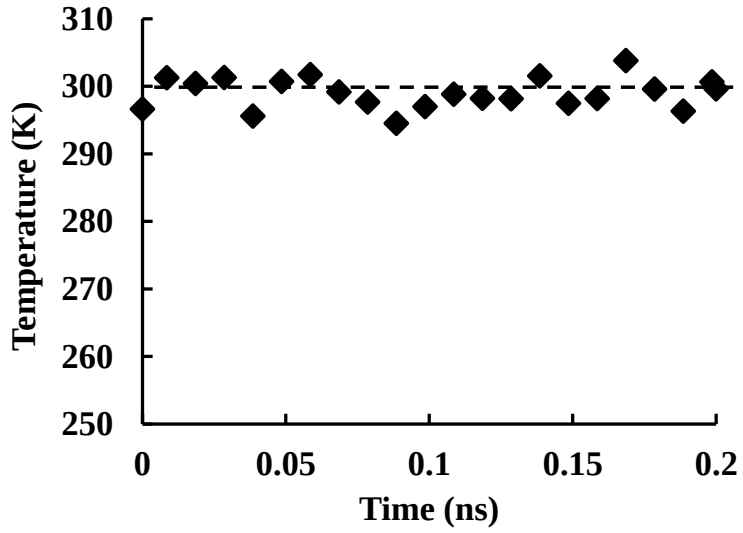


**Figure C.5:** The variation in temperature for configuration 1 over time during the NVE stage after completing the NPT and NVT stages for a constant temperature of 300 K.

**Bibliography**

[1] Fourier, J., 1807. "Théorie De La Propagation De La Chaleur Dans Les Solides". *Manuscrit présenté à l'Institut de France*.

[2] Narasimhan, T.N., 1999. "Fourier's Heat Conduction Equation: History, Influence, and Connections". *Reviews of Geophysics,* **37**(1), pp. 151-172.

[3] Chen, G., Nanoscale Energy Transport and Conversion: A Parallel Treatment of Electrons, Molecules, Phonons, and Photons, Oxford University Press, USA, 2005.

[4] Berman, R., Thermal Conduction in Solids, Oxford University Press, USA, 1976.

[5] Cahill, D.G., Ford, W.K., Goodson, K.E., Mahan, G.D., Majumdar, A., Maris, H.J., Merlin, R., Sr, P., 2003. "Nanoscale Thermal Transport". *Journal of Applied Physics,* **93**(2), pp. 793-818.

[6] Balasubramanian, G., Banerjee, S., Puri, I.K., 2008. "Interfacial Thermal Resistance in Nanoscale Heat Transfer". vol. ASME.

[7] Balasubramanian, G., Puri, I.K., 2011. "Heat Conduction across a Solid-Solid Interface: Understanding Nanoscale Interfacial Effects on Thermal Resistance". *Applied Physics Letters,* **99**(1), pp. 013116-013116-013113.

[8] Hochbaum, A.I., Chen, R.K., Delgado, R.D., Liang, W.J., Garnett, E.C., Najarian, M., Majumdar, A., Yang, P.D., 2008. "Enhanced Thermoelectric Performance of Rough Silicon Nanowires". *Nature,* **451**(7175), pp. 163-U165.

[9] Liangruksa, M., Puri, I.K., 2011. "Lattice Thermal Conductivity of a Silicon Nanowire under Surface Stress". *Journal of Applied Physics,* **109**(11).

[10] Venkatasubramanian, R., Siivola, E., Colpitts, T., O'Quinn, B., 2001. "Thin-Film Thermoelectric Devices with High Room-Temperature Figures of Merit". *Nature,* **413**(6856), pp. 597-602.

[11] Asheghi, M., Touzelbaev, M.N., Goodson, K.E., Leung, Y.K., Wong, S.S., 1998. "Temperature-Dependent Thermal Conductivity of Single-Crystal Silicon Layers in Soi Substrates". *Journal of Heat Transfer-Transactions of the Asme,* **120**(1), pp. 30-36.

[12] Ju, Y.S., Goodson, K.E., 1999. "Process-Dependent Thermal Transport Properties of Silicon-Dioxide Films Deposited Using Low-Pressure Chemical Vapor Deposition". *Journal of Applied Physics,* **85**(10), pp. 7130-7134.

[13] Liu, W., Asheghi, M., 2004. "Phonon-Boundary Scattering in Ultrathin Single-Crystal Silicon Layers". *Applied Physics Letters,* **84**(19), pp. 3819-3821.

[14] Liu, S., Xu, X.F., Xie, R.G., Zhang, G., Li, B.W., 2012. "Anomalous Heat Conduction and Anomalous Diffusion in Low Dimensional Nanoscale Systems". *European Physical Journal B,* **85**(10).

[15] Hu, T., Tang, Y., 2010. "Anomalous Heat Conduction in One-Dimensional Quantum Fermi-Pasta-Ulam Lattice: Semiquantal Approach". *Journal of the Physical Society of Japan,* **79**(6).

[16] Li, H.B., Li, Z., 2010. "Anomalous Energy Diffusion and Heat Conduction in One-Dimensional System". *Chinese Physics B,* **19**(5).

[17] Yang, X.M., To, A.C., Tian, R., 2010. "Anomalous Heat Conduction Behavior in Thin Finite-Size Silicon Nanowires". *Nanotechnology,* **21**(15).

[18] Henry, A., Chen, G., 2009. "Anomalous Heat Conduction in Polyethylene Chains: Theory and Molecular Dynamics Simulations". *Physical Review B,* **79**(14).

[19] Nishino, T.H., 2007. "Anomalous Heat Conduction in Quasi-One-Dimensional Gases". *Progress of Theoretical Physics,* **118**(4), pp. 657-666.

[20] Berber, S., Kwon, Y.-K., Tomanek, D., 2000. "Unusually High Thermal Conductivity of Carbon Nanotubes". *Physical Review Letters,* **84**(20), pp. 4613-4616.

[21] Che, J., Cagin, T., Goddard III, W.A., 2000. "Thermal Conductivity of Carbon Nanotubes". *Nanotechnology*, **11**(2), pp. 65.

[22] Fujii, M., Zhang, X., Xie, H., Ago, H., Takahashi, K., Ikuta, T., Abe, H., Shimizu, T., 2005. "Measuring the Thermal Conductivity of a Single Carbon Nanotube". *Physical Review Letters*, **95**(6), pp. 065502.

[23] Hone, J., Whitney, M., Piskoti, C., Zettl, A., 1999. "Thermal Conductivity of Single-Walled Carbon Nanotubes". *Physical Review B*, **59**(4), pp. R2514-R2516.

[24] Balandin, A.A., Ghosh, S., Bao, W., Calizo, I., Teweldebrhan, D., Miao, F., Lau, C.N., 2008. "Superior Thermal Conductivity of Single-Layer Graphene". *Nano Letters*, **8**(3), pp. 902-907.

[25] Ghosh, S., Calizo, I., Teweldebrhan, D., Pokatilov, E.P., Nika, D.L., Balandin, A.A., Bao, W., Miao, F., Lau, C.N., 2008. "Extremely High Thermal Conductivity of Graphene: Prospects for Thermal Management Applications in Nanoelectronic Circuits". *Applied Physics Letters*, **92**(15), pp. 151911-151913.

[26] Balandin, A.A., 2009. "Chill Out". *Spectrum, IEEE*, **46**(10), pp. 34-39.

[27] Chan, P.C., Yang, C., Zhang, M., Fu, Y., 2008. "The Application of Carbon Nanotubes in Cmos Integrated Circuits". Solid-State and Integrated-Circuit Technology, 2008. ICSICT 2008. 9th International Conference on, vol. IEEE, pp. 534-536.

[28] Koswatta, S.O., Nikonov, D.E., Lundstrom, M.S., 2005. "Computational Study of Carbon Nanotube Pin Tunnel Fets". Electron Devices Meeting, 2005. IEDM Technical Digest. IEEE International, vol. IEEE, pp. 518-521.

[29] Pop, E., 2010. "Energy Dissipation and Transport in Nanoscale Devices". *Nano Research*, **3**(3), pp. 147-169.

[30] Pop, E., Sinha, S., Goodson, K.E., 2006. "Heat Generation and Transport in Nanometer-Scale Transistors". *Proceedings of the Ieee,* **94**(8), pp. 1587-1601.

[31] Khanikar, V., Mudawar, I., Fisher, T., 2009. "Effects of Carbon Nanotube Coating on Flow Boiling in a Micro-Channel". *International Journal of Heat and Mass Transfer,* **52**(15–16), pp. 3805-3817.

[32] Ujereh, S., Fisher, T., Mudawar, I., 2007. "Effects of Carbon Nanotube Arrays on Nucleate Pool Boiling". *International Journal of Heat and Mass Transfer,* **50**(19), pp. 4023-4038.

[33] Boettner, H., Chen, G., Venkatasubramanian, R., 2006. "Aspects of Thin-Film Superlattice Thermoelectric Materials, Devices, and Applications". *MRS bulletin,* **31**(03), pp. 211-217.

[34] Ghamaty, S., Elsner, N.B., Thermoelectric Device with Si/Sic Superlattice N-Legs, in, Google Patents, 2004.

[35] Pal, S., Balasubramanian, G., Puri, I.K., 2012. "Modifying Thermal Transport in Electrically Conducting Polymers: Effects of Stretching and Combining Polymer Chains". *The Journal of chemical physics,* **136**, pp. 044901.

[36] Yakuphanoglu, F., Şenkal, B.F., Saraç, A., 2008. "Electrical Conductivity, Thermoelectric Power, and Optical Properties of Organo-Soluble Polyaniline Organic Semiconductor". *Journal of Electronic Materials,* **37**(6), pp. 930-934.

[37] Alaghemandi, M., Leroy, F., Muller-Plathe, F., Bohm, M.C., 2010. "Thermal Rectification in Nanosized Model Systems: A Molecular Dynamics Approach". *Physical Review B,* **81**(12), pp. 125410-125421.

[38] Hu, M., Keblinski, P., Li, B., 2008. "Thermal Rectification at Silicon-Amorphous Polyethylene Interface". *Applied Physics Letters,* **92**(21), pp. 211908-211911.

[39] Majumdar, A., 1993. "Microscale Heat Conduction in Dielectric Thin Films". *ASME Transactions Journal of Heat Transfer,* **115**, pp. 7-16.

[40] Ziman, J.M., Electrons and Phonons: The Theory of Transport Phenomena in Solids, OUP Oxford, 2001.

[41] Allen, M.P., Tildesley, D.J., Computer Simulation of Liquids, Oxford university press, 1989.

[42] Binder, K., Horbach, J., Kob, W., Paul, W., Varnik, F., 2004. "Molecular Dynamics Simulations". *Journal of Physics: Condensed Matter,* **16**(5), pp. S429.

[43] Hansson, T., Oostenbrink, C., van Gunsteren, W., 2002. "Molecular Dynamics Simulations". *Current Opinion in Structural Biology,* **12**(2), pp. 190-196.

[44] Hoover, W.G., Computational Statistical Mechanics, Elsevier Science Publishers Ltd., 1991.

[45] Schelling, P.K., Phillpot, S.R., Keblinski, P., 2002. "Comparison of Atomic-Level Simulation Methods for Computing Thermal Conductivity". *Physical Review B,* **65**(14).

[46] Müller-Plathe, F., 1997. "A Simple Nonequilibrium Molecular Dynamics Method for Calculating the Thermal Conductivity". *The Journal of chemical physics,* **106**, pp. 6082.

[47] Boara, G., Sparpaglione, M., 1995. "Synthesis of Polyanilines with High Electrical Conductivity". *Synthetic metals,* **72**(2), pp. 135-140.

[48] Pal, S., Balasubramanian, G., Puri, I.K., 2013. "Reducing Thermal Transport in Electrically Conducting Polymers: Effects of Ordered Mixing of Polymer Chains". *Applied Physics Letters,* **102**(2), pp. 023109.

[49] Wang, L., Li, B., 2008. "Phononics Gets Hot". *Physics World,* **21**(3), pp. 27-29.

[50] Hu, J., Ruan, X., Chen, Y.P., 2009. "Thermal Conductivity and Thermal Rectification in Graphene Nanoribbons: A Molecular Dynamics Study". *Nano Letters,* **9**(7), pp. 2730-2735.

[51] Inzelt, G., Pineri, M., Schultze, J.W., Vorotyntsev, M.A., 2000. "Electron and Proton Conducting Polymers: Recent Developments and Prospects". *Electrochimica acta,* **45**(15-16), pp. 2403-2421.

[52] Jin, J.Z., Wang, Q., Haque, M.A., 2010. "Doping Dependence of Electrical and Thermal Conductivity of Nanoscale Polyaniline Thin Films". *J. Phys. D: Appl. Phys.,* **43**(20), pp. -.

[53] Park, Y.W., Yoon, C.O., Lee, C.H., Shirakawa, H., Suezaki, Y., Akagi, K., 1989. "Conductivity and Thermoelectric Power of the Newly Processed Polyacetylene". *Synth. Met.,* **28**(3), pp. D27-D34.

[54] Kittel, C., Introduction to Solid State Physics, Wiley, New York, 1966.

[55] Henry, A., Chen, G., 2008. "High Thermal Conductivity of Single Polyethylene Chains Using Molecular Dynamics Simulations". *Physical Review Letters,* **101**(23), pp. -.

[56] Liu, J., Yang, R.G., 2010. "Tuning the Thermal Conductivity of Polymers with Mechanical Strains". *Physical Review B,* **81**(17), pp. -.

[57] Hsieh, W.P., Losego, M.D., Braun, P.V., Shenogin, S., Keblinski, P., Cahill, D.G., 2011. "Testing the Minimum Thermal Conductivity Model for Amorphous Polymers Using High Pressure". *Physical Review B,* **83**(17), pp. -.

[58] Goodson, K.E., 2007. "Materials Science: Ordering up the Minimum Thermal Conductivity of Solids". *Science,* **315**(5810), pp. 342-343.

[59] Kelly, M.J., Wolfe, D.E., Singh, J., Eldridge, J., Zhu, D.M., Miller, R., 2006. "Thermal Barrier Coatings Design with Increased Reflectivity and Lower Thermal Conductivity for High-Temperature Turbine Applications". *Int. J. Appl. Ceram. Tech.,* **3**(2), pp. 81-93.

[60] Pirovano, A., Lacaita, A.L., Benvenuti, A., Pellizzer, F., Bez, R., 2004. "Electronic Switching in Phase-Change Memories". *IEEE Trans. Electron Devices,* **51**(3), pp. 452-459.

[61] Venkatasubramanian, R., 2000. "Lattice Thermal Conductivity Reduction and Phonon Localizationlike Behavior in Superlattice Structures". *Physical Review B,* **61**(4), pp. 3091-3097.

[62] Bhowmick, S., Shenoy, V.B., 2006. "Effect of Strain on the Thermal Conductivity of Solids". *Journal of Chemical Physics,* **125**(16), pp. -.

[63] Kim, W., Zide, J., Gossard, A., Klenov, D., Stemmer, S., Shakouri, A., Majumdar, A., 2006. "Thermal Conductivity Reduction and Thermoelectric Figure of Merit Increase by Embedding Nanoparticles in Crystalline Semiconductors". *Physical Review Letters,* **96**(4), pp. 045901.

[64] Lacevic, N.M., Maxwell, R.S., Saab, A., Gee, R.H., 2005. "Molecular Dynamics Simulations of Ordering of Poly(Dimethylsiloxane) under Uniaxial Stress†". *Journal of Physical Chemistry. B,* **110**(8), pp. 3588-3594.

[65] Roberge, M., Prud'homme, R.E., Brisson, J., 2004. "Molecular Modelling of the Uniaxial Deformation of Amorphous Polyethylene Terephthalate". *Polymer,* **45**(4), pp. 1401-1411.

[66] Ni, B., Watanabe, T., Phillpot, S.R., 2009. "Thermal Transport in Polyethylene and at Polyethylene–Diamond Interfaces Investigated Using Molecular Dynamics Simulation". *Journal of Physics: Condensed Matter,* **21**(8), pp. 084219.

[67] Terao, T., Lussetti, E., Müller-Plathe, F., 2007. "Nonequilibrium Molecular Dynamics Methods for Computing the Thermal Conductivity: Application to Amorphous Polymers". *Phys. Rev. E,* **75**(5), pp. 057701.

[68] Plimpton, S.J., 1995. "Fast Parallel Algorithms for Short-Range Molecular Dynamics". *J. Comput. Phys.,* **117**(1), pp. 1-19.

[69] Ostwal, M.M., Tsotsis, T.T., Sahimi, M., 2007. "Molecular Dynamics Simulation of Diffusion and Sorption of Water in Conducting Polyaniline". *Journal of Chemical Physics,* **126**(12), pp. -.

[70] Shenogin, S., Ozisik, R., 2005. "Deformation of Glassy Polycarbonate and Polystyrene: The Influence of Chemical Structure and Local Environment". *Polymer,* **46**(12), pp. 4397-4404.

[71] Takehara, Z.I., Kanamura, K., Yonezawa, S.I., Hanawa, T., 1989. "The Diffusion of Various Anions in a Polyacetylene Cathode of a Secondary Lithium Battery". *J. Power Sources,* **25**(4), pp. 277-285.

[72] Humphrey, W., Dalke, A., Schulten, K., 1996. "Vmd: Visual Molecular Dynamics". *J. Mol. Graphics Modell.,* **14**(1), pp. 33-38.

[73] Müller-Plathe, F., 1997. "A Simple Nonequilibrium Molecular Dynamics Method for Calculating the Thermal Conductivity". *J. Chem. Phys.,* **106**(14), pp. 6082.

[74] Incropera, F.P., Fundamentals of Heat and Mass Transfer, John Wiley & Sons, Hoboken, N.J., 2007.

[75] Jin, J., 2009. "In-Plane Thermal Conductivity of Nanoscale Polyaniline Thin Films". *Applied Physics Letters,* **95**(3), pp. 033113.

[76] Moses, D., Denenstein, A., 1984. "Experimental Determination of the Thermal Conductivity of a Conducting Polymer: Pure and Heavily Doped Polyacetylene". *Physical Review B,* **30**(4), pp. 2090.

[77] Chen, G., 1997. "Size and Interface Effects on Thermal Conductivity of Superlattices and Periodic Thin-Film Structures". *Journal of Heat Transfer,* **119**(2), pp. 220-229.

[78] Kumar, S., Vradis, G.C., 1994. "Thermal Conductivity of Thin Metallic Films". *Journal of Heat Transfer,* **116**(1), pp. 28-34.

[79] Choy, C.L., 1977. "Thermal Conductivity of Polymers". *Polymer (Guilford),* **18**(10), pp. 984.

[80] Balasubramanian, G., Puri, I.K., 2011. "Heat Conduction across a Solid-Solid Interface: Understanding Nanoscale Interfacial Effects on Thermal Resistance". *Appl. Phys. Lett.,* **99**(1), pp. 013116.

[81] Balasubramanian, G., Puri, I.K., Bohm, M.C., Leroy, F., 2011. "Thermal Conductivity Reduction through Isotope Substitution in Nanomaterials: Predictions from an Analytical Classical Model and Nonequilibrium Molecular Dynamics Simulations". *Nanoscale,* **3**(9), pp. 3714-3720.

[82] White, J.L., Spruiell, J.E., 1983. "The Specification of Orientation and Its Development in Polymer Processing". *Polym. Eng. Sci.,* **23**(5), pp. 247-256.

[83] Springborg, M., 1988. "Helical Polyacetylene: A First-Principles Approach". *Phys. Rev. B,* **37**(3), pp. 1218-1227.

[84] Liu, J., Yang, R.G., 2010. "Tuning the Thermal Conductivity of Polymers with Mechanical Strains". *Phys. Rev. B.,* **81**(17), pp. 174122.

[85] Shen, S., Henry, A., Tong, J., Zheng, R., Chen, G., 2010. "Polyethylene Nanofibres with Very High Thermal Conductivities". *Nat. Nano.,* **5**(4), pp. 251-255.

[86] Pal, S., Balasubramanian, G., Puri, I.K., 2012. "Modifying Thermal Transport in Electrically Conducting Polymers: Effects of Stretching and Combining Polymer Chains". *J. Chem. Phys.,* **136**(4), pp. 044901-044907.

[87] Alaghemandi, M., Schulte, J., Leroy, F., Müller-plathe, F., Böhm, M.C., 2011. "Correlation between Thermal Conductivity and Bond Length Alternation in Carbon Nanotubes: A Combined Reverse Nonequilibrium Molecular Dynamics—Crystal Orbital Analysis". *J. Comput. Chem.,* **32**(1), pp. 121-133.

[88] Balasubramanian, G., Puri, I.K., 2011. "Heat Conduction across a Solid-Solid Interface: Understanding Nanoscale Interfacial Effects on Thermal Resistance". *Appl. Phys. Lett.,* **99**(1), pp. 013116-013116-013113.

[89] Ostwal, M.M., Sahimi, M., Tsotsis, T.T., 2009. "Water Harvesting Using a Conducting Polymer: A Study by Molecular Dynamics Simulation". *Phys. Rev. E,* **79**(6), pp. 061801.

[90] Balasubramanian, G., Puri, I.K., Böhm, M.C., Leroy, F., 2011. "Thermal Conductivity Reduction through Isotope Substitution in Nanomaterials: Predictions from an Analytical Classical Model and Nonequilibrium Molecular Dynamics Simulations". *Nanoscale,* **3**(9), pp. 3714-3720.

[91] Dashora, P., Gupta, G., 1996. "On the Temperature Dependence of the Thermal Conductivity of Linear Amorphous Polymers". *Polymer,* **37**(2), pp. 231-234.

[92] Kaul, P.B., Day, K.A., Abramson, A.R., 2007. "Application of the Three Omega Method for the Thermal Conductivity Measurement of Polyaniline". *J. Appl. Phys.,* **101**(8), pp. 083507-083507.

[93] Schweizer, R.J., Menke, K., Roth, S., 1984. "Thermal Conductivity of Polyacetylene". *J. Chem. Phys.,* **81**(12), pp. 6301-6303.

[94] Starr, C., 1936. "The Copper Oxide Rectifier". *Physics,* **7**(1), pp. 15-19.

[95] Roberts, N.A., Walker, D.G., 2011. "A Review of Thermal Rectification Observations and Models in Solid Materials". *International Journal of Thermal Sciences,* **50**(5), pp. 648-662.

[96] Zeng, N., Wang, J.-S., 2008. "Mechanisms Causing Thermal Rectification: The Influence of Phonon Frequency, Asymmetry, and Nonlinear Interactions". *Physical Review B,* **78**(2), pp. 024305-024309.

[97] Pereira, E., 2010. "Thermal Rectification in Quantum Graded Mass Systems". *Physics Letters A,* **374**(19), pp. 1933-1937.

[98] Chang, C.W., Okawa, D., Majumdar, A., Zettl, A., 2006. "Solid-State Thermal Rectifier". *Science,* **314**(5802), pp. 1121-1124.

[99] Yang, N., Zhang, G., Li, B., 2009. "Thermal Rectification in Asymmetric Graphene Ribbons". *Applied Physics Letters,* **95**(3), pp. 033107-033109.

[100] Yang, N., Zhang, G., Li, B., 2008. "Carbon Nanocone: A Promising Thermal Rectifier". *Applied Physics Letters,* **93**(24), pp. 243111-243113.

[101] Hu, M., Goicochea, J.V., Michel, B., Poulikakos, D., 2009. "Thermal Rectification at Water/Functionalized Silica Interfaces". *Applied Physics Letters,* **95**(15), pp. 151903-151905.

[102] Alaghemandi, M., Leroy, F., Müller-Plathe, F., Böhm, M.C., 2010. "Thermal Rectification in Nanosized Model Systems: A Molecular Dynamics Approach". *Physical Review B,* **81**(12), pp. 125410-125421.

[103] Murad, S., Puri, I.K., 2012. "Communication: Thermal Rectification in Liquids by Manipulating the Solid-Liquid Interface". *The Journal of chemical physics,* **137**(8), pp. 081101-081104.

[104] Murad, S., Puri, I.K., 2012. "Thermal Rectification in a Fluid Reservoir". *Applied Physics Letters,* **100**(12), pp. 121901-121905.

[105] Murad, S., Puri, I.K., 2013. "A Thermal Logic Device Based on Fluid-Solid Interfaces". *Applied Physics Letters,* **102**(19), pp. 193109-193112.

[106] Wang, L., Li, B., 2008. "Thermal Memory: A Storage of Phononic Information". *Physical Review Letters,* **101**(26), pp. 267203.

[107] Li, B., Wang, L., Casati, G., 2004. "Thermal Diode: Rectification of Heat Flux". *Physical Review Letters,* **93**(18), pp. 184301.

[108] Norton, B., Probert, S.D., 1983. "Achieving Thermal Rectification in Natural-Circulation Solar-Energy Water Heaters". *Applied Energy,* **14**(3), pp. 211-225.

[109] Lan, J., Wang, L., Li, B., 2007. "Interface Thermal Resistance between Frenkel-Kontorova and Fermi-Pasta-Ulam Lattices". *International Journal of Modern Physics B,* **21**(23n24), pp. 4013-4016.

[110] Hu, T., Hu, K., Tang, Y., 2010. "Anharmonic on-Site Potential Implies Asymmetry Thermal Transport in 1d Mass-Graded Harmonic Lattice". *Physica B: Condensed Matter,* **405**(21), pp. 4407-4412.

[111] Chantrenne, P., Barrat, J.-L., 2004. "Analytical Model for the Thermal Conductivity of Nanostructures". *Superlattices and Microstructures,* **35**(3–6), pp. 173-186.

[112] Yu, C.H., Shi, L., Yao, Z., Li, D.Y., Majumdar, A., 2005. "Thermal Conductance and Thermopower of an Individual Single-Wall Carbon Nanotube". *Nano Letters,* **5**(9), pp. 1842-1846.

[113] Wu, G., Li, B., 2007. "Thermal Rectification in Carbon Nanotube Intramolecular Junctions: Molecular Dynamics Calculations". *Physical Review B,* **76**(8), pp. 085424.

[114] Alaghemandi, M., Leroy, F., Algaer, E., Böhm, M.C., Müller-Plathe, F., 2010. "Thermal Rectification in Mass-Graded Nanotubes: A Model Approach in the Framework of Reverse Non-Equilibrium Molecular Dynamics Simulations". *Nanotechnology,* **21**(7), pp. 075704-.

[115] Zheng, Q.B., Xia, D., Xue, Q.Z., Yan, K.Y., Gao, X.L., Li, Q., 2009. "Computational Analysis of Effect of Modification on the Interfacial Characteristics of a Carbon Nanotube-Polyethylene Composite System". *Applied Surface Science,* **255**(6), pp. 3534-3543.

[116] Frankland, S.J.V., Caglar, A., Brenner, D.W., Griebel, M., 2002. "Molecular Simulation of the Influence of Chemical Cross-Links on the Shear Strength of Carbon Nanotube-Polymer Interfaces". *Journal of Physical Chemistry B*, **106**(12), pp. 3046-3048.

[117] Sahoo, N.G., Rana, S., Cho, J.W., Li, L., Chan, S.H., 2010. "Polymer Nanocomposites Based on Functionalized Carbon Nanotubes". *Progress in Polymer Science*, **35**(7), pp. 837-867.

[118] Stepanian, S.G., Karachevtsev, M.V., Glamazda, A.Y., Karachevtsev, V.A., Adamowicz, L., 2008. "Stacking Interaction of Cytosine with Carbon Nanotubes: Mp2, Dft and Raman Spectroscopy Study". *Chemical Physics Letters*, **459**(1–6), pp. 153-158.

[119] Campidelli, S., Klumpp, C., Bianco, A., Guldi, D.M., Prato, M., 2006. "Functionalization of Cnt: Synthesis and Applications in Photovoltaics and Biology". *Journal of Physical Organic Chemistry*, **19**(8-9), pp. 531-539.

[120] Lee, J., Varshney, V., Brown, J.S., Roy, A.K., Farmer, B.L., 2012. "Single Mode Phonon Scattering at Carbon Nanotube-Graphene Junction in Pillared Graphene Structure". *Applied Physics Letters*, **100**(18).

[121] Lordi, V., Yao, N., 2000. "Molecular Mechanics of Binding in Carbon-Nanotube-Polymer Composites". *Journal of Materials Research*, **15**(12), pp. 2770-2779.

[122] Balasubramanian, G., Banerjee, S., Puri, I.K., 2008. "Unsteady Nanoscale Thermal Transport across a Solid-Fluid Interface". *Journal of Applied Physics*, **104**(6).

[123] Pan, R.Q., Xu, Z.J., Zhu, Z.Y., Wang, Z.X., 2007. "Thermal Conductivity of Functionalized Single-Wall Carbon Nanotubes". *Nanotechnology*, **18**(28).

[124] Verma, A., Kauser, M.Z., Ruden, P.P., 2005. "Ensemble Monte Carlo Transport Simulations for Semiconducting Carbon Nanotubes". *Journal of Applied Physics*, **97**(11), pp. 114319-114318.

[125] Balasubramanian, G., Banerjee, S., Puri, I.K., Interfacial Thermal Resistance in Nanoscale Heat Transfer, in: IMECE 2008, ASME, Boston, Massachusetts, USA, 2008, pp. 969-973.

[126] Murad, S., Puri, I.K., 2008. "Thermal Transport across Nanoscale Solid-Fluid Interfaces". *Applied Physics Letters,* **92**(13), pp. 133105.

[127] Li, N., Ren, J., Wang, L., Zhang, G., Hänggi, P., Li, B., 2012. "Colloquium: Phononics: Manipulating Heat Flow with Electronic Analogs and Beyond". *Reviews of Modern Physics,* **84**(3), pp. 1045-1066.

[128] Bhowmik, R., Katti, K.S., Katti, D., 2007. "Molecular Dynamics Simulation of Hydroxyapatite–Polyacrylic Acid Interfaces". *Polymer,* **48**(2), pp. 664-674.

[129] Chien, S.K., Yang, Y.T., Chen, C.K., 2010. "Thermal Conductivity and Thermal Rectification in Carbon Nanotubes with Geometric Variations of Doped Nitrogen Non-Equilibrium Molecular Dynamics Simulations". *Physics Letters A,* **374**(48), pp. 4885-4889.

[130] Ni, X.X., Zhang, G., Li, B.W., 2011. "Thermal Conductivity and Thermal Rectification in Unzipped Carbon Nanotubes". *Journal of Physics-Condensed Matter,* **23**(21).

[131] Murad, S., Puri, I.K., 2013. "Communication: A Tractable Design for a Thermal Transistor". *The Journal of chemical physics,* **139**(15), pp. 151102

[132] Wang, L., Li, B., 2007. "Thermal Logic Gates: Computation with Phonons". *Physical Review Letters,* **99**(17), pp. 177208

[133] Varshney, V., Patnaik, S.S., Roy, A.K., Froudakis, G., Farmer, B.L., 2010. "Modeling of Thermal Transport in Pillared-Graphene Architectures". *ACS nano,* **4**(2), pp. 1153-1161.

[134] Wang, Y., Chen, S., Ruan, X., 2012. "Tunable Thermal Rectification in Graphene Nanoribbons through Defect Engineering: A Molecular Dynamics Study". *Applied Physics Letters,* **100**(16), pp. 163101-163103.

[135] Wang, Y., Qiu, B., Ruan, X., 2012. "Edge Effect on Thermal Transport in Graphene Nanoribbons: A Phonon Localization Mechanism Beyond Edge Roughness Scattering". *Applied Physics Letters*, **101**(1), pp. 013101-013104.

[136] Wei, N., Xu, L., Wang, H.-Q., Zheng, J.-C., 2011. "Strain Engineering of Thermal Conductivity in Graphene Sheets and Nanoribbons: A Demonstration of Magic Flexibility". *Nanotechnology*, **22**(10), pp. 105705.

[137] Zhang, G., Zhang, H., 2011. "Thermal Conduction and Rectification in Few-Layer Graphene Y Junctions". *Nanoscale*, **3**(11), pp. 4604-4607.

[138] Hu, J., Ruan, X., Jiang, Z., Chen, Y.P., 2009. "Molecular Dynamics Calculation of Thermal Conductivity of Graphene Nanoribbons". *AIP Conference Proceedings*, **1173**(1), pp. 135-138.

[139] Yu, C., Zhang, G., 2013. "Impacts of Length and Geometry Deformation on Thermal Conductivity of Graphene Nanoribbons". *Journal of Applied Physics*, **113**(4), pp. 044306-044309.

[140] Chen, J., Zhang, G., Li, B., 2010. "Molecular Dynamics Simulations of Heat Conduction in Nanostructures: Effect of Heat Bath". *arXiv preprint arXiv:1005.4481*.

[141] Brenner, D.W., Shenderova, O.A., Harrison, J.A., Stuart, S.J., Ni, B., Sinnott, S.B., 2002. "A Second-Generation Reactive Empirical Bond Order (Rebo) Potential Energy Expression for Hydrocarbons". *Journal of Physics: Condensed Matter*, **14**(4), pp. 783-802.

[142] Wei, D., Song, Y., Wang, F., 2011. "A Simple Molecular Mechanics Potential for Mm Scale Graphene Simulations from the Adaptive Force Matching Method". *The Journal of chemical physics*, **134**, pp. 184704.

[143] Chen, J., Zhang, G., Li, B., 2009. "Tunable Thermal Conductivity of Si1−Xgex Nanowires". *Applied Physics Letters,* **95**(7), pp. 073117

[144] Tewary, V.K., Yang, B., 2009. "Singular Behavior of the Debye-Waller Factor of Graphene". *Physical Review B,* **79**(12), pp. 125416.

[145] Tohei, T., Kuwabara, A., Oba, F., Tanaka, I., 2006. "Debye Temperature and Stiffness of Carbon and Boron Nitride Polymorphs from First Principles Calculations". *Physical Review B,* **73**(6), pp. 064304.

[146] Zhai, X., Jin, G., 2011. "Stretching-Enhanced Ballistic Thermal Conductance in Graphene Nanoribbons". *EPL (Europhysics Letters),* **96**(1), pp. 16002.

[147] Li, X., Yang, P., 2013. "Effect of Equilateral Triangle Vacancy Defect on the Thermal Conductivity and Thermal Rectification of Graphene: A Molecular Dynamics Study". *International Journal of Materials and Structural Integrity,* **7**(1), pp. 131-138.

[148] Bajec, P., Pevec, B., Voncina, D., Miljavec, D., Nastran, J., 2005. "Extending the Low-Speed Operation Range of Pm Generator in Automotive Applications Using Novel Ac-Dc Converter Control". *Industrial Electronics, IEEE Transactions on,* **52**(2), pp. 436-443.

[149] Sziebert, I.L., Motor Control Circuit and Method with Digital Level Shifting, in, Google Patents, 2000.

[150] Ajimsha, R., Jayaraj, M., Kukreja, L., 2008. "Electrical Characteristics of N-Zno/P-Si Heterojunction Diodes Grown by Pulsed Laser Deposition at Different Oxygen Pressures". *Journal of Electronic Materials,* **37**(5), pp. 770-775.

[151] Ghosh, S., Calizo, I., Teweldebrhan, D., Pokatilov, E.P., Nika, D.L., Balandin, A.A., Bao, W., Miao, F., Lau, C.N., 2008. "Extremely High Thermal Conductivity of Graphene: Prospects

for Thermal Management Applications in Nanoelectronic Circuits". *Applied Physics Letters*, **92**(15), pp. 151911

[152] Nika, D.L., Pokatilov, E.P., Askerov, A.S., Balandin, A.A., 2009. "Phonon Thermal Conduction in Graphene: Role of Umklapp and Edge Roughness Scattering". *Physical Review B*, **79**(15), pp. 155413.

[153] Evans, W.J., Hu, L., Keblinski, P., 2010. "Thermal Conductivity of Graphene Ribbons from Equilibrium Molecular Dynamics: Effect of Ribbon Width, Edge Roughness, and Hydrogen Termination". *Applied Physics Letters*, **96**(20), pp. 203112

[154] Grndl, A., Hoffmann, B., Half-Bridge Subassembly, in, Google Patents, USA, 2004.

[155] Lau, C.N., Bao, W., Velasco Jr, J., 2012. "Properties of Suspended Graphene Membranes". *Materials Today*, **15**(6), pp. 238-245.

[156] Sun, H., 1998. "Compass: An Ab Initio Force-Field Optimized for Condensed-Phase Applicationsoverview with Details on Alkane and Benzene Compounds". *J. Phys. Chem. B*, **102**(38), pp. 7338-7364.

[157] Hockney, R.W., Eastwood, J.W., Computer Simulation Using Particles, Institute of Physics, 1992.

[158] Ostwal, M.M., Sahimi, M., Tsotsis, T.T., 2009. "Water Harvesting Using a Conducting Polymer: A Study by Molecular Dynamics Simulation". *Phys. Rev. E*, **79**(6).

[159] Dianoux, A.J., Kneller, G.R., Sauvajol, J.L., Smith, J.C., 1993. "The Polarized Density-of-States of Crystalline Polyacetylene - Molecular-Dynamics Analysis and Comparison with Neutron-Scattering Results". *J.Chem. Phys.*, **99**(7), pp. 5586-5596.

[160] Connected Mathematics Project, (2006) Areas and Perimeters [Applet], Cmp Interactive Resources Grade 6, Http://Connectedmath.Msu.Edu/Cd/Grid/Index.Html (September 27, 2012).

[161] Prewitt, J.M.S., Object Enhancement and Extraction, in: B. S. Lipkin, A. Rosenfeld (Ed.) Picture Processing and Psychopictorics, Academic Press, New York, 1970.